

CONTRIBUTIONS IN INVERSE SYNTHETIC  
APERTURE RADAR IMAGING

TAN HWEE SIANG  
(B.Eng.(Hons.)), NUS

A THESIS SUBMITTED  
FOR THE DEGREE OF DOCTOR OF PHILOSOPHY  
DEPARTMENT OF ELECTRICAL & COMPUTER ENGINEERING  
NATIONAL UNIVERSITY OF SINGAPORE

2008

# Acknowledgements

The author would like to thank his thesis advisor Professor Yeo Tat Soon for his advice, guidance and support; without whom the completion of the work would have been impossible. He is also very grateful to Professor Yeo for taking time to read the thesis despite his busy schedule.

Apart from his thesis advisor, the author would also like to especially thank Dr Ma Changzheng for his guidance, advice and teachings, without whom the author would face a much steeper learning curve. Dr Ma has been very supportive and especially kind in sharing his knowledge and experience from the diverse areas of work he had been involved in. Not forgetting other former colleagues, the author would also like to thank Dr Zhang Qun for his guidance and help during his short stay with the Radar and Signal Processing Laboratory and a former colleague Dr Guo Xin for her guidance and help.

The author would also like to express gratitude to the friends and colleagues

of the Radar and Signal Processing Laboratory who have helped in one way or another in making his work possible and successful.

The author is also thankful to his family for their support and understanding. Most importantly, the author would like to thank his fiancée, Miss Chua Pingzi for her patience and support over the past four years.

# Contents

<b>Acknowledgements</b>	<b>ii</b>
<b>Summary</b>	<b>xiv</b>
<b>1 Introduction</b>	<b>1</b>
1.1 Overview of Radar . . . . .	1
1.1.1 MTI and Pulse Doppler Radar . . . . .	2
1.1.2 Imaging Radar . . . . .	3
1.1.3 Synthetic Aperture Radar . . . . .	5
1.1.4 ISAR, InSAR and InISAR . . . . .	8
1.2 Recent Developments . . . . .	11
1.3 My Contributions . . . . .	16
1.4 Organization of Thesis . . . . .	17
1.5 Papers Published/In Preparation . . . . .	18
1.5.1 Papers Published . . . . .	18
1.5.2 Papers In Preparation . . . . .	19
<b>2 Antenna Array Imaging</b>	<b>20</b>
2.1 Introduction . . . . .	20
2.1.1 Developments towards Antenna Array Imaging . . . . .	21

2.1.2	Problems Examined . . . . .	23
2.2	Principle of Cross-range Measurement Method . . . . .	25
2.2.1	Two-Antenna Interferometric Technique . . . . .	25
2.2.2	Antenna Array Technique . . . . .	29
2.3	Three-dimensional Imaging Based on Array DOA Estimation . . . .	32
2.3.1	Wideband Signal Model . . . . .	33
2.3.2	Envelope Alignment . . . . .	34
2.3.3	Motion Compensation . . . . .	36
2.3.4	Cross-range Position Estimation . . . . .	44
2.3.5	Scatterer Registration . . . . .	45
2.3.6	Estimation of the Axis of Rotation . . . . .	47
2.4	Simulation Results . . . . .	48
2.4.1	Target with Isolated Scatterer . . . . .	49
2.4.2	Two-ring Target . . . . .	56
2.4.3	Aeroplane Target . . . . .	60
2.5	Conclusions . . . . .	68
<b>3</b>	<b>Sparse Array ISAR Imaging</b>	<b>70</b>
3.1	Introduction . . . . .	70
3.1.1	Problems Examined . . . . .	71
3.2	Spatial and Time Domain Signal Model for Three-dimensional Motion	74
3.3	Envelope Alignment . . . . .	79
3.4	Three-dimensional Imaging Algorithms . . . . .	80
3.4.1	Interferometric Imaging using Three Antenna Elements . . .	81
3.4.2	Imaging based on DOA estimation of Cross Antenna Array .	84

3.4.3	Imaging based on Combination of Sparse-array Beamforming and ISAR imaging . . . . .	86
3.5	Estimation of Synthesis Rotation Vector . . . . .	94
3.6	Simulation Results . . . . .	97
3.7	Conclusions . . . . .	99
<b>4</b>	<b>Micro-Doppler extraction using Hough Transform</b>	<b>102</b>
4.1	Introduction . . . . .	102
4.1.1	Micro-Doppler Phenomena . . . . .	103
4.1.2	Problem Examined . . . . .	104
4.1.3	Possible Approach . . . . .	104
4.2	Signal Model and Micro-Doppler . . . . .	106
4.2.1	Signal Model . . . . .	106
4.2.2	Micro-Doppler effect . . . . .	108
4.3	HT and Micro-Doppler Extraction Algorithm . . . . .	112
4.3.1	Standard Hough Transform . . . . .	113
4.3.2	Extended Hough Transform . . . . .	115
4.3.3	Proposed Extraction Algorithm . . . . .	117
4.4	Simulation Results . . . . .	119
4.5	Comments and Discussions . . . . .	127
4.6	Conclusions . . . . .	132
<b>5</b>	<b>Micro-Doppler removal by Range Grouping</b>	<b>133</b>
5.1	Introduction . . . . .	133
5.2	Simulation Model . . . . .	135
5.3	Micro-Doppler Separation Steps . . . . .	138
5.4	Simulation Results . . . . .	140

5.4.1	Simulated Helicopter Target . . . . .	141
5.4.2	Simulated Tank Target . . . . .	144
5.5	Conclusions . . . . .	147
<b>6</b>	<b>Imaging of a Helicopter Target</b>	<b>148</b>
6.1	Introduction . . . . .	148
6.1.1	Problems Examined . . . . .	150
6.2	Simulation Model . . . . .	151
6.3	Envelope Alignment and Zero-force Windowing . . . . .	154
6.4	Simulation Results . . . . .	158
6.5	Conclusions . . . . .	162
<b>7</b>	<b>Conclusions</b>	<b>165</b>
7.1	Summary of Work . . . . .	165
7.2	Contributions . . . . .	168
7.3	Future Work . . . . .	170
<b>A</b>	<b>Derivation of Equations</b>	<b>172</b>
A.1	Derivation of (3.28) . . . . .	172
A.2	Derivation of (4.4) . . . . .	176
	<b>Bibliography</b>	<b>180</b>

# List of Tables

2.1	Imaging system parameters (Antenna array method) . . . . .	49
3.1	Imaging system parameters (Sparse-array ISAR imaging method) .	98
4.1	Simulation parameters (Hough Transform extraction method) . . .	120
4.2	Sinusoidal Parameters obtained using Extended Hough Transform. .	123
4.3	Straight Line Parameters obtained using Standard Hough Transform	125
7.1	Summary of work. . . . .	167



# List of Figures

1.1	Stripmap mode SAR. . . . .	7
1.2	Spotlight mode SAR. . . . .	8
1.3	Similarity between Spotlight SAR and ISAR. . . . .	9
2.1	Geometry of the two-antenna cross-range measurement system. . . . .	26
2.2	Geometry of the L-shape antenna array imaging system. . . . .	30
2.3	Relation between rotation axis and scatterers coordinates. . . . .	47
2.4	3D model of the target (target with isolated scatterer). . . . .	50
2.5	Projected views of the target model (target with isolated scatterer). . . . .	51
2.6	Contour plot of ISAR image (target with isolated scatterer). . . . .	52
2.7	3D image obtained by the antenna array method (target with isolated scatterer). . . . .	53
2.8	Projected views of the image obtained by the antenna array method (target with isolated scatterer) . . . . .	54
2.9	3D image obtained by three-antenna method (target with isolated scatterer). . . . .	55
2.10	3D model of the target (two-ring target). . . . .	56
2.11	Projected views of the target model (two-ring target). . . . .	57
2.12	Contour plot of ISAR image (two-ring target). . . . .	58

2.13	Contour plot of correlation function of the ISAR images of the different antennas (two-ring target). . . . .	59
2.14	3D image obtained by the antenna array method (two-ring target). . . . .	60
2.15	Projected views of the image obtained by the antenna array method (two-ring target). . . . .	61
2.16	3D image obtained by the three-antenna method (two-ring target). . . . .	62
2.17	3D model of the target (aeroplane target). . . . .	62
2.18	Projected views of the target model (aeroplane target). . . . .	63
2.19	Contour plot of ISAR image (aeroplane target). . . . .	64
2.20	X-direction cross-range estimation plot (aeroplane target). . . . .	65
2.21	Z-direction cross-range estimation plot (aeroplane target). . . . .	65
2.22	3D image obtained by the antenna array method (aeroplane target). . . . .	66
2.23	Projected views of the image obtained by the antenna array method (aeroplane target). . . . .	67
2.24	3D image obtained by the three-antenna method (aeroplane target). . . . .	68
2.25	Projected views of the image obtained by the three-antenna method (aeroplane target). . . . .	69
3.1	Geometry of the radar and the target (Sparse-array ISAR imaging method). . . . .	74
3.2	Three-antenna ISAR imaging system. . . . .	82
3.3	Physical and synthetic antenna aperture. . . . .	89
3.4	Beam pattern of physical, synthesis and combined array. . . . .	91
3.5	Position of antenna elements. . . . .	93
3.6	Beam pattern of sparse array. . . . .	94
3.7	Beam pattern combining sparse array and ISAR processing . . . . .	95

3.8	Relation between rotation axis and scatterers' coordinates. . . . .	96
3.9	Target's three-dimensional image. . . . .	100
3.10	Target's ISAR image (Sparse-array ISAR imaging method). . . . .	100
3.11	Reconstructed three-dimensional image (Sparse-array ISAR imaging method). . . . .	101
4.1	Geometry of a radar and target with a rotating scatterer. . . . .	107
4.2	Comparison of the range profile at two different time instance. . . .	111
4.3	Range profile of a target that comprises of two non-rotating scatter points and a rotating scatter point. . . . .	112
4.4	ISAR image comparison for a target consisting of non-rotating and rotating scatterers . . . . .	121
4.5	Range profile of a target with both rotating scatterers and non- rotating scatterers . . . . .	122
4.6	Range profile after the spectrum of the rotating scatterer has been eliminated from the original range profile. . . . .	123
4.7	ISAR imaging result after the spectrum of the rotating scatterer has been eliminated. . . . .	124
4.8	Range profile after the spectrum of the rotating scatterer has been eliminated. . . . .	126
4.9	Final ISAR imaging result after the spectrum of the rotating scat- terer has been eliminated. . . . .	127
4.10	Processed result of a rotating scatterer with a rotating frequency of 160Hz and radius of 1m. . . . .	129
4.11	Imaging result of a rotating scatterer with a rotating frequency of 50Hz and a radius of 1m after remediation processing. . . . .	130

5.1	Geometry of a target with a rotating scatterer . . . . .	136
5.2	Simulated target without rotating parts . . . . .	141
5.3	Range profile of target with rotating parts before micro-Doppler separation . . . . .	142
5.4	Range profile of target with rotating parts after micro-Doppler sep- aration . . . . .	142
5.5	ISAR image of target with rotating parts without micro-Doppler separation . . . . .	143
5.6	ISAR image of target with rotating parts after micro-Doppler sepa- ration . . . . .	143
5.7	Range profile of target with irregularly moving parts before micro- Doppler separation . . . . .	144
5.8	Range profile of target without micro-Doppler contamination . . . .	145
5.9	Range profile of target with irregularly moving parts after micro- Doppler separation . . . . .	145
5.10	ISAR image of target with irregularly moving parts without micro- Doppler separation . . . . .	146
5.11	ISAR image of target with irregularly moving parts after micro- Doppler separation . . . . .	147
6.1	Geometry of the radar and target. . . . .	151
6.2	Projected image of the target. . . . .	158
6.3	Range profile after alignment using conventional method. . . . .	159
6.4	Range profile after alignment using the proposed method. . . . .	160
6.5	Variance of range profile using conventional method. . . . .	161
6.6	Variance of range profile using the proposed method. . . . .	162

6.7	Positions of flash signals in the slow time domain. . . . .	163
6.8	Positions of flash signals in the range domain. . . . .	163
6.9	ISAR image obtained using conventional method. . . . .	164
6.10	ISAR image obtained using the proposed method. . . . .	164

# Summary

The area of work chosen is Inverse Synthetic Aperture Radar (ISAR) imaging as ISAR images provides an extremely useful application, that is, for the purpose of surveillance and target recognition. The focus of our work is to tackle several important issues that have not been resolved till now. The thesis proposed methods to solve these issues so as to improve the quality of ISAR images. The two major contributions are in the area of array-based ISAR imaging and imaging of target exhibiting the micro-Doppler phenomena.

The thesis begins with an introduction to the developments of various radar imaging methodologies, followed by a detailed discussion on a three-dimensional inverse synthetic aperture radar imaging method using an antenna array configuration in Chapter 2. The performance of conventional interferometric ISAR imaging system using the three-antenna configuration is poor as the positions of synthesis scatterers cannot be correctly estimated. Synthesis scatterer arises as scatterers

that are located on a line parallel to the axis of rotation having the same range-Doppler value, and are projected onto the same point on the ISAR plane. If the synthesis scatterers could not be properly resolved, the image may not be accurate and identification would be difficult. The proposed antenna array method has been shown to be able to improve the system's ability to separate these scatterers as compared to the methods published previously. Two cross-range motion parameters measurement algorithms, one based on array processing of the range profile and the other based on correlation of ISAR images of different antennas are proposed to estimate the motion parameters for cross-range motion compensation. The coordinates registration method for synthesis scatterers is also discussed.

Further to the perpendicular array configuration, a new imaging method, a two-dimensional sparse-array beamforming combined with ISAR imaging is proposed in Chapter 3. It reaps the benefits of the sparse array to achieve a large aperture while using ISAR imaging to lower the sidelobe of the sparse-array beam pattern, thereby achieving a high resolution ISAR image. The advantage of a sparse array is that it achieves a wider aperture while the number of antenna elements can be greatly reduced compared to a full array. The reduced number of antenna elements allows a lower computational load compared to a full array. Also, due to the large aperture formed by the sparse array, a long coherent time duration is not needed to separate scatterers. Therefore, during a short time duration, the rotation of the

target relative to the antenna array can be approximated as an uniform rotation. Hence techniques such as time-frequency analysis or super resolution spectrum analysis are not necessary and the analysis is simplified. Two target rotational parameters estimation methods for the estimation of the rotation parameters of the target are also proposed in this chapter.

The next part of the thesis deals with the issues of micro-motions known as the micro-Doppler phenomenon in Chapter 4 and 5. Mechanical vibrations or rotation of structures in a target introduce additional frequency modulations on returned signals and generate sidebands about the center Doppler frequency of the target's body. This is known as the micro-Doppler phenomenon. A clear ISAR image of the moving target that comprises of moving or rotating parts cannot be obtained using the conventional range-Doppler imaging principle due to the presence of the micro-Doppler. Using the standard Hough Transform and an extended Hough Transform, a separation method by detecting the straight lines and the sinusoids on the range profile was presented. Separations of irregular micro-motions on the range profile image is presented in Chapter 5.

Finally the envelope alignment for a helicopter target is discussed in Chapter 6. Envelope alignment is usually the first step in ISAR imaging, before radial motion compensation and spectrum analysis can be carried out. However, range alignment



for a helicopter target is different from other rigid targets as the return signal from the rotor is a "flashing-like" signal and the strength of the signal has the strongest value when the blade is perpendicular to the wavefront. Therefore its envelope is not a slow-time varying signal in the slow-time domain and conventional envelope alignment methods based on rigid target assumption is not suitable in this case.

In all the above works, the simulated results shows that our proposed methods are effective and that good results have been achieved. The use of the antenna array and sparse-array imaging configuration improves the system's ability to separate synthesis scatterers and allows for a more accurate image, allowing for easier target identification. The separation and removal of the micro-Doppler using the extended Hough Transform and the range grouping method is important for achieving a better ISAR image, as the presence of the micro-Doppler contamination would cause image blurring. The proposed method for helicopter target envelope alignment has also allowed for a more precise envelope alignment, thus allowing for an improved ISAR image.

# Chapter 1

## Introduction

### 1.1 Overview of Radar

Radar is an acronym for radio detection and ranging. A radar is an active system that transmits a beam of electromagnetic(EM) energy in the microwave region of the EM spectrum to detect and locate objects. It was developed to detect hostile aircrafts in the beginning of the 20th century. After years of development, new applications have been discovered. Today, radar is used, for example, in air traffic control, environmental observations[1] and aircraft collision avoidance systems[2].

The most basic form of radar system consists of a transmitter connected to a transmitting antenna and a receiver connected to a receiving antenna. The transmitter transmits EM waves which is re-radiated in many directions when it reaches

the target. Some of the EM waves will be backscattered to the receiver and only the backscattered energy that is received by the receiving antenna is of interest to us<sup>1</sup>. The energy is collected at the receiver and can be used to calculate the distance to the target as well as its velocity in relation to the radar.

As an active system, radar provides its own illumination and this allows for continuous day and night applications. Furthermore, neither clouds, fog nor precipitation have a significant effect on EM waves, thus allowing for all-weather applications[3]. In the subsequent sections, we briefly provide some overviews of the various different radar followed by some of the recent developments in the radar fields without any detailed derivations. The details on radar system modeling are discussed in [4], [5] and [6].

### 1.1.1 MTI and Pulse Doppler Radar

Although a radar can theoretically detect an isolated target easily, it is not so simple to detect a target in real world applications, as there are other factors to consider. Radar have to deal with more than receiver noise when detecting targets since they will also receive echoes from the natural environment such as the land, sea and weather. These echoes are known as clutter and can be many order of magnitude larger than the target echoes. When the target echo and a clutter echo

---

<sup>1</sup>Applicable for monostatic radars where the transmitting and receiving antennas are located together. For bistatic radars, the transmitter and receiver are located separately and only the energy received by the receiver is useful.

appear in the same resolution cell, the target may not be detectable[1]. Although there are many methods for reducing clutters in order to detect the desired target echoes, the most powerful method is by making use of the Doppler effect, which is the change of frequency of the radar echo signal due to the relative velocity between the radar and the moving target.

The two methods commonly used are moving target indication(MTI) and pulse-Doppler processing[7]. In MTI, which is often used in ground-based radar, two or more pulse returns are processed to create a null region around zero Doppler frequency shift to reject the clutter spectrum. Pulse-Doppler processing is often used in airborne radar[8], as well as some ground based radars. In this technique, a train of pulses is coherently processed using a Fourier transform type algorithm to divide the received signal into a series of narrow spectral bands. The target is then separated from the zero velocity mainbeam clutter, and from the sidelobe clutter that may occur at other velocities for a moving radar. More details on the radar processing techniques are discussed in [1] and [7].

### 1.1.2 Imaging Radar

A radar image is defined by [9] as the spatial distribution of reflectivity corresponding to the object. Comparing a radar image to an optical image, an useful optical image must display spatial distribution of optical reflectivity with sufficient detail

for the object to be recognized by a human observer. Similarly, a radar image must present a spatial distribution of radar reflectivity sufficient to characterize the object illuminated.

### **Direct Imaging Radar**

It is possible to carry out radar imaging of a three-dimensional object by scanning it with a range-gated, short-pulse radar with a pencil beam antenna[9]. The antenna beam and the range gate are systematically scanned throughout the entire three-dimensional volume and the values of reflectivity received is displayed as a function of the spatial coordinates being scanned. This method, known as the direct imaging method, requires no additional calculations in order to retrieve the image. However, it has several disadvantages. For example, in order to obtain a high spatial resolution image, one may require impractical radar configurations. Furthermore, the cross-range resolution degrades as range increases[9].

### **Side Looking Aperture Radar**

The first high resolution radar imaging began with the use of the side-looking aperture radar(SLAR). In the early 1950s, engineers observed that, instead of rotating the antenna to scan the target area like in the direct imaging method, the antenna can be fixed to the fuselage of the aircraft. This allowed for much longer apertures and hence improved along-track resolution. The imaging radar became known as the SLAR and was primarily used for military reconnaissance purposes. Some

systems operating at frequencies as high as 35GHz with a short pulse duration a fraction of a microsecond, were capable of producing imagery with resolutions in the 10-20m range[3]. In the 1960's when SLAR images was made available for scientific use, it found applications in geology, oceanography and land use studies.

The cross-range resolution was still not suitable for high-resolution imaging and synthetic imaging methods were later developed and are able to overcome these problems.

### 1.1.3 Synthetic Aperture Radar

Synthetic imaging uses the result of several observations of the object from different angles and frequencies. The resolution obtainable using a wideband signal and large apertures can thus be obtained by combining signals obtained from sequences of narrow band, single-angle observation. This results in an image with higher resolution.

The most commonly used synthetic imaging technique is in Synthetic Aperture Radar(SAR). SAR is fundamentally different from SLAR. The radar is mounted on a moving platform such as a satellite or an airplane. The earliest knowledge that Doppler-frequency analysis could be used to obtain fine cross-range resolution is attributed to Carl Wiley of the Goodyear Aircraft Corporation in June 1951.

Wiley observed that the reflections from fixed targets at an angular separation relative to the velocity vector could be resolved by frequency analysis of the along-track spectrum. The first experimental demonstration of SAR mapping occurred in 1953 when a strip map of a section of Key West, Florida was generated by frequency analysis of data collected using a 3-cm wavelength signal from a C-46 aircraft by a group from the University of Illinois[10].

SAR is an airborne or spaceborne radar imaging technique for generating high resolution maps of surface target areas and terrain. SAR can be used to obtain fine resolution in both the slant range and cross-range direction. SAR achieves fine cross-range resolution by synthesizing the effect of a large aperture using radar with a small physical aperture. Details on SAR and the basic SAR processing are discussed in [1], [3] and [10]. SAR is operated mainly in two modes, namely the stripmap and spotlight mode.

### **Stripmap(Linear) Mode**

With a fixed side-looking antenna, the beam is pointed normal to the platform motion. The maximum possible cross-range resolution is approximately equal to one-half of the real aperture's cross-range dimension. Fig. 1.1 illustrates a SAR operating in the stripmap mode.

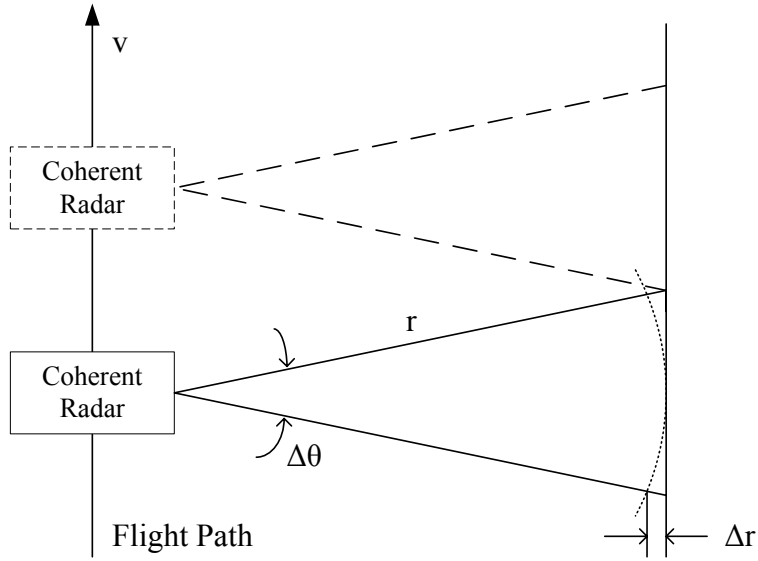


Fig. 1.1: Stripmap mode SAR.

Signal energy collected during illumination of each range-resolved scatterer is made to arrive in phase at the output of the radar processor in order to realise the narrow beamwidth associated with the long, synthetically generated aperture. This is achieved by first correcting for all movement of the aircraft that deviates from straight-line motion. At this point, we have obtained the unfocused SAR. For focused SAR, the quadratic phase error produced by straight line motion of the radar past each point of the area to be mapped needs to be corrected. This is discussed in [3][10][11].

### Spotlight Mode

Spotlight mode refers to the case where the antenna squints off in the azimuth direction to track a particular area of interest as shown in Fig. 1.2. In this mode,



the radar is carried on a moving vehicle and the antenna illuminates a fixed spot on the terrain by continuously changing the look angle.

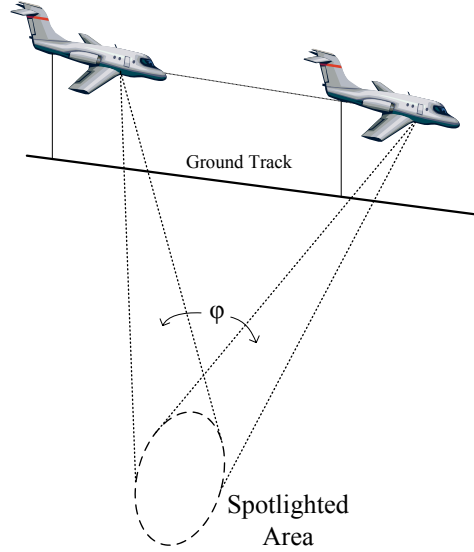


Fig. 1.2: Spotlight mode SAR.

Here the cross-range resolution is limited not by the size of the real aperture, but by the target dwell time. Synthetic aperture length for small  $\varphi$  can be thought of as the tangential distance that the radar travels while moving through the angle  $\varphi$ .

#### 1.1.4 ISAR, InSAR and InISAR

Inverse Synthetic Aperture Radar (ISAR) imaging has received significant attention in the past three decades. ISAR imaging[9][10][11][12][13][14] obtains the image of a target by analyzing the return radar signal in terms of the range delay and

Doppler frequency of the scatterers that makes up the target. ISAR is similar to SAR except that the radar remains stationary while the targeted is rotated. It can be explained with reference to the spotlight mode SAR. The similarity between spotlight mode SAR and ISAR is shown in Fig. 1.3.

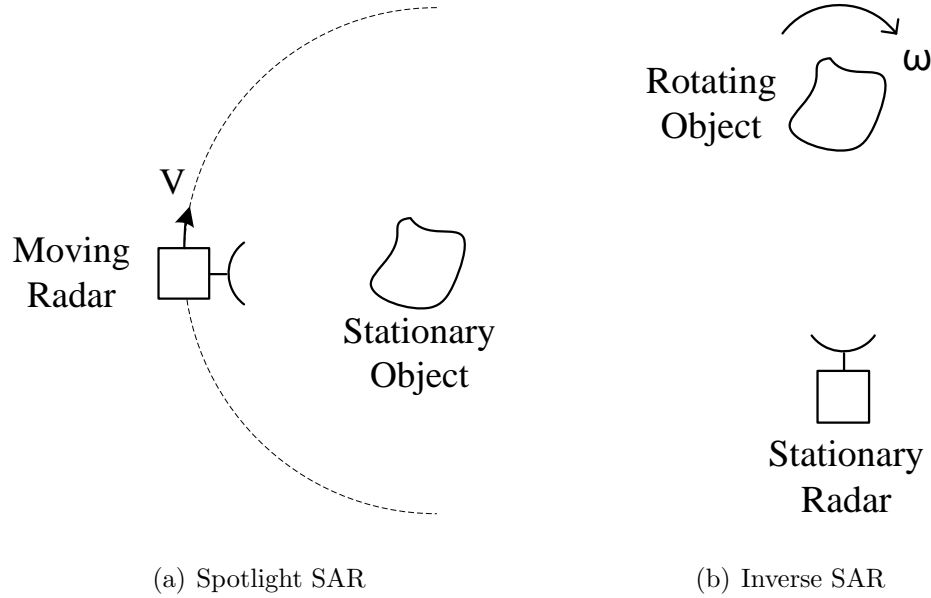


Fig. 1.3: Similarity between Spotlight SAR and ISAR.

After correcting for unwanted deviation from straight line motion and for quadratic phase errors, a spotlight SAR can be seen as if the radar were flying a portion of a circle around the target. Although the radar moves about the target in the case of spotlight SAR, the same data would be collected if the radar is stationary and the target is rotated. In ISAR imaging, this is precisely what happens. The radar remains stationary while the targeted is rotated. The Doppler frequency gradient required to obtain fine cross-range resolution is generated by

the motion of the object relative to the radar. Fine range resolution is attained by transmitting a wideband signal while its cross-range resolution is dependent on the relative rotation between the radar and the target.

A major shortcoming of such a two-dimensional SAR image is that it cannot provide the altitude information. The interferometric processing technique was subsequently introduced to provide high-resolution digital elevation maps(DEMs) in three-dimensional terrain mapping. This interferometric SAR(InSAR) technique proposed by Graham[15] is based on the phase difference measurement of the SAR signal returns received by two spatially separated antennas. InSAR has since been used in many applications such as target scattering diagnosis and motion modeling, determination of airborne sensors and for automatic aircraft landing. Details on InSAR are discussed in [16], [17] and [18].

Similar to InSAR, the use of interferometric processing and ISAR processing can also be combined to form a powerful technique known as Interferometric ISAR(InISAR)[19][20][21][22][23]. A minimum of two antennas are used and the elevation information of a target can be obtained by comparing the phase difference of the two antennas' received signals. Similarly, a three-dimensional ISAR image can be obtained by combining the two-dimensional ISAR images from the various image planes.

## 1.2 Recent Developments

One of the challenges in radar imaging is the formation of clear images of maneuvering targets. A maneuvering target is defined as one that has translational and rotational or non-uniform motions during the coherent processing interval. Although the ISAR images of a cooperating and non-maneuvering targets can be obtained quite easily, it is not so if the targets are non-cooperative and/or maneuvering. Unfortunately, the targets that need to be imaged in ISAR imaging are usually non-cooperative and may be maneuvering.

For maneuvering targets, the rotation axis and the rotation speed of the target relative to the radar is time varying. This means that the Doppler is time varying and the usual range-doppler imaging[14] techniques cannot be used. Techniques such as time frequency analysis or super resolution spectrum analysis needs to be carried out in order to obtain a fine ISAR image. Such methods have demonstrated improved image quality in imaging maneuvering targets and are discussed in [24], [25], [26], [27], [28] and [29].

Recent works have also looked at using the micro-Doppler features or micro-motion dynamics of a target for imaging[30][31][32][33]. Micro-Doppler features can be regarded as a unique signature of an object and provide additional information for classification, recognition and identification of the object[34][35][36].

Mechanical vibration or rotation of structures in a target introduces additional frequency modulation on returned signals and generates side-bands about the center Doppler frequency of the target's body. To exploit these weak features, high-resolution time-frequency analysis with high dynamic range is being considered as a suitable tool to extract the time-varying micro-Doppler signature[30][34][35]. A four-parameter adaptive Chirplet signal representation method[37] has been used for the separation of rotating parts from the target body in [38].

Antenna array has also been used for ISAR imaging[39]. Conventional antenna-array-ISAR three-dimensional imaging system carries out imaging by first obtaining the ISAR image of the different antennas and then use array direction of arrival(DOA) estimation[40] on every strong scatterer to get the spatial position of that scatterer. The synthetic aperture formed by the target's motion is used to separate the scatterers while the antenna array aperture is only used for position measurement. In [39], a linear antenna array adaptive beamforming(ABF) was used in ISAR imaging. The temporal radio camera which combined ABF with ISAR, where ISAR images from different antennas, are non-coherently combined to obtain a clearer image. Although this can improve the quality of the ISAR image, it was not further developed for three-dimensional imaging by the authors. Part of our work involves developing it for three-dimensional imaging as we overcome difficulties like synthesis scatterers separation and scatterer registration.

The use of sparse arrays are also attractive for many applications as they provide a wider aperture with a reduced number of antenna elements compared to a full array[41][42]. Due to the large aperture formed by the sparse array, a long coherent time duration is not needed to separate scatterers. Furthermore, during a short time duration, the rotation of the target relative to the antenna array can be approximated as an uniform rotation. However, sparse arrays have the drawback of high sidelobe levels, which must be reduced to fully realize the advantages of using sparse array. The design and optimization of sparse arrays are discussed in [43] and [44].

The concept of Multi-Input Multi-Output(MIMO) radars has also drawn considerable interests due to its advantages. MIMO radars transmit orthogonal waveforms[45][46][47][48] or non-coherent waveforms[49][50][51] instead of coherent waveforms which form a focused beam in the traditional transmit beamforming techniques. In the MIMO radar receiver, a matched filterbank is used to extract the orthogonal waveform components[52]. There are two major advantages of a MIMO system[47]. Firstly, the increased spatial diversity can be obtained. The orthogonal components are transmitted from different antennas. If these antennas are far enough from each other, the target radar cross sections(RCS) for different

transmitting paths will become independent random variables. Thus each orthogonal waveform carries independent information about the target. This spatial diversity can be utilized to perform better detection. Secondly, the phase differences caused by different transmitting antennas along with the phase differences caused by different receiving antennas can form a new virtual array steering vector.

Recent works have also allowed for a more efficient use of the radio frequency(RF) spectrum with newer signal processing techniques. The need for a more efficient use of the RF spectrum has become an important issue in recent years due to increasing demand for spectrum usage rights by the communications industry coupled with the demand for wider instantaneous bandwidths for radar applications[53][54]. As RF spectral crowding becomes more severe, certain operational scenarios may make the use of spectral diversity impossible[55]. This has resulted in work towards a shared-spectrum radar.

The ability to simultaneously operate multiple radars at the same frequency in a multistatic configuration and in close proximity to one another would result in a great improvement in radar spectral efficiency. Shared-spectrum radar has been implemented through the use of waveform diversity techniques, where each radar transmits a unique waveform and signal processing in the receiver is utilized to separate the individual waveforms and to mitigate interference. Techniques proposed

include the Multistatic Adaptive Pulse Compression(MAPC) algorithm[56][57], where multiple known transmitted waveforms are adaptively pulse compressed using reiterative minimum mean-square error(RMMSE) estimation[58][59]. An adaptive beamforming component has also been combined with the MAPC algorithm in [55] to enable better estimation performance and to increase the number of multistatic radars which can simultaneously operate in the same spectrum.

Over-The-Horizon Radar(OTHR) is another area that has seen developments. OTHR is an useful application as it performs wide-area surveillance at long range well beyond the limit of the conventional line-of-sight(LOS) radars[60][61]. It can track aircraft more than 3000 km away and over millions of square kilometers of open ocean[62]. Various signal processing methods including using adaptive time-frequency analysis or other techniques[63][64][65] have been considered for the suppression of impulsive and transient interference signals for enhanced OTHR performance.

Previous OTHR systems using a single OTHR only provides information about the target range and Doppler frequency in the slant range direction. With only these information, the user is not able to uniquely determine the movement of the targets. The system is improved by a concurrent operation of two OTHR systems proposed in [66] and [67]. Using two OTHRs would result in cross radar



interference, but this was solved by new cross-radar interference cancellation approaches presented in [66] and [67]. The use of two OTHRs, positioned at different locations, not only extends the coverage for enhanced surveillance, but also offers higher-dimensional information of a moving target. The information is key to achieving improved target classification and predictions of ballistic destinations.

### 1.3 My Contributions

Although we have provided a general discussion about the recent developments in the many different types of radars, the main area of work chosen is in area of Inverse Synthetic Aperture Radar(ISAR) imaging as we feel that ISAR imaging provides an extremely useful application, that is, for the purpose of surveillance and target recognition.

The two major contributions are in the area of array-based ISAR imaging and imaging of target exhibiting the micro-Doppler phenomena. In the array-based ISAR imaging, a perpendicular array method and a sparse array method has been proposed for imaging. The array-based method has the ability to separate synthesis scatterers. Synthesis scatterers are scatterers that are located at different physical positions, but are projected onto the same range-Doppler unit as they have the same range-Doppler value. As a result of the ability to separate synthesis

scatterers, the ISAR images have been significantly improved.

The rotation or movement of structures in a target introduces additional frequency modulations on the returned signals and also generates sidebands about the center Doppler frequency of the target and causes blurring of the processed ISAR image. This is known as the micro-Doppler phenomena. Methods proposed include the extended Hough Transform and zero-force windowing to remove the micro-Doppler effect of the rotor of a helicopter target which exhibits an uniform rotation. A range grouping method has also been proposed for the imaging of a tank target which exhibits a non-uniform movement. The ISAR images has also improved significantly with the micro-Doppler contamination removed.

## 1.4 Organization of Thesis

The thesis begins with the an introduction to the developments of radar imaging in Chapter 1. This is followed by a discussion on a three-dimensional inverse synthetic aperture radar imaging method using an antenna array configuration and sparse array configuration in Chapter 2 and 3 respectively.

Chapter 4 and 5 discuss on ISAR imaging of targets exhibiting the micro-Doppler phenomenon. The phenomenon were caused by mechanical vibrations or rotation of structures in a target, and introduce additional frequency modulations

on returned signals. Chapter 4 discusses imaging of a target with a regular rotating body part using the Hough Transform while Chapter 5 discusses imaging of a target with an irregular moving body part. This is followed by a discussion on ISAR imaging of a helicopter target in Chapter 6. Finally we conclude our work in Chapter 7.

## 1.5 Papers Published/In Preparation

The work described in this thesis resulted in the following papers.

### 1.5.1 Papers Published

- Q. Zhang, T. S. Yeo and H. S. Tan, "Imaging of Moving Target with Rotating Parts Based on Hough Transform," *IEEE International Geoscience and Remote Sensing Symposium*, July 2006 Page(s): 4183 - 4186
- H. S. Tan, C. Z. Ma, T. S. Yeo, Q. Zhang, C. S. Ng and B. Zou, "ISAR imaging of targets with moving parts using micro-doppler detection on the range profile image," *IEEE International Geoscience and Remote Sensing Symposium*, July 2007 Page(s): 499 - 502
- C. Z. Ma, T. S. Yeo, H. S. Tan, Z. Liu, X. Dong and B. Zou, "ISAR imaging of helicopter," *IEEE International Geoscience and Remote Sensing Symposium*, July 2007 Page(s): 838 - 841

- Q. Zhang, T. S. Yeo, H. S. Tan and Y. Luo, "Imaging of a Moving Target With Rotating Parts Based on the Hough Transform," *IEEE Transactions on Geoscience and Remote Sensing*, Volume 46, Issue 1, Jan. 2008 Page(s): 291 - 299
- C. Z. Ma, T. S. Yeo, Q. Zhang, H. S. Tan and J. Wang, "Three-Dimensional ISAR Imaging Based on Antenna Array," *IEEE Transactions on Geoscience and Remote Sensing*, Volume 46, Issue 2, Feb. 2008 Page(s): 504 - 515
- C. Z. Ma, T. S. Yeo, H. S. Tan, J. Wang and B. Chen, "Three-Dimensional ISAR Imaging Using a Two-Dimensional Sparse Antenna Array," *IEEE Geoscience and Remote Sensing Letters*, Volume 5, Issue 3, Jul. 2008 Page(s): 378 - 382

### 1.5.2 Papers In Preparation

- C. Z. Ma, T. S. Yeo, H. S. Tan, J. Wang and B. Chen, "3D Imaging Based on 2D Sparse Array Space-Time CLEAN and Hill Climbing Optimization."

# Chapter 2

## Antenna Array Imaging

### 2.1 Introduction

In this chapter, a three-dimensional inverse synthetic aperture radar imaging method based on an antenna array configuration is proposed. Conventional interferometric ISAR(InISAR) imaging system[19][20][21][22] and InISAR systems using three antennas[23] fail when scatterers having the same range-Doppler value are projected onto the ISAR plane as a synthesis scatterer. We propose using two antenna arrays perpendicular to each other to improve the system's ability to separate these scatterers.

Motion compensation is also key towards achieving a focussed image. The criterion for the selection of a range unit that contains an isolated scatterer in the

two-dimensional array domain for motion compensation is discussed. If there is no range unit which contains only an isolated scatterer, radial and cross-range motion compensation has to be carried out by motion parameter estimation. Two cross-range motion parameters measurement algorithms, one based on array processing of the range profile and another based on correlation of ISAR images of different antennas are proposed. The coordinates registration problem for the scatterers of a synthesis scatterer is also discussed.

### 2.1.1 Developments towards Antenna Array Imaging

In inverse synthetic aperture radar(ISAR) imaging, one of the main concerns is the achievable resolution. Fine range resolution is attained by transmitting a wide-band signal while its cross-range resolution is dependent on the relative rotation between the radar and the target[10][12][14][39][68][69][70][71]. While high quality ISAR images of a cooperative and non-maneuvering targets can be easily obtained, it is not so if the targets are non-cooperative and/or maneuvering[24][25][27][28]. For non-cooperative targets, the targets' rotation angle cannot be obtained and therefore, the cross-range scale of the ISAR image is not known. For maneuvering targets, the rotational axis of the target relative to the radar is time varying, therefore the range-Doppler plane may not coincide with the target's conventional visual range and cross-range plane.

To overcome the above drawbacks, 3-D interferometric ISAR imaging known as InISAR were proposed[19][20][21][22][23][72]. Interferometry technique was first introduced by Graham to compute the elevation of terrain[15]. Two antennas were used and the elevation information was obtained by comparing the phase difference of the received signals from the two antennas.

A two-antenna technique in the ISAR field was also presented in [69], where the cross-range trajectory was measured by two antennas. It was however not further developed for three-dimensional imaging by its authors. The principle of InISAR is similar to InSAR except for some differences. In InSAR, the imaging plane's direction of movement is perpendicular to the direction of the antennas' baseline, therefore the two SAR images are automatically aligned in the cross-range direction. In InISAR, however, the imaging plane is not necessarily perpendicular to the baseline, and therefore, height information cannot be obtained by simply using two antennas. As a result, three antennas are used in InISAR. Furthermore, when the target's motion is along the direction of the baseline, cross-range motion compensation known as three-dimensional focusing[22][73] is also required.

Antenna array has also been used for ISAR imaging. Conventional antenna-array-ISAR three-dimensional imaging system carries out imaging by first obtaining the ISAR image of the different antennas and then use array direction of

arrival(DOA) estimation[40] on every strong scatterer to get the spatial position of that scatterer. The synthetic aperture formed by the target's motion is used to separate the scatterers while the antenna array aperture is only used for position measurement.

In [39], a linear antenna array adaptive beamforming(ABF) was used in ISAR imaging. The temporal radio camera which combined ABF with ISAR, where ISAR images from different antennas, are non-coherently combined to obtain a clearer image. Although this can improve the quality of the ISAR image, the work was not further developed into a method for three-dimensional imaging by its author. In this chapter, we have furthered the above work and coherent processing(direction-of-arrival estimation) is used to obtain the three-dimensional images.

### 2.1.2 Problems Examined

As an ISAR image is a projection of the scatterers of a target onto the range-Doppler plane, scatterers that are located at different positions, but having the same range-Doppler value will be projected onto the same range-Doppler unit. These scatterers on the ISAR image are known as synthesis scatterers. The two-antenna based interferometry technique can only measure a scatterer's position, but cannot measure the positions of more than one scatterers which are projected



onto the ISAR plane as a synthesis scatterer. In this chapter, we propose using two perpendicular antenna arrays, one in the  $x$ -axis direction and the other in the  $z$ -axis direction, to measure the positions of scatterers of a synthesis scatterer.

For the motion compensation of the antenna array based 3-D imaging configuration, we can carry out simultaneous range and cross-range motion compensation if there is a range cell with an isolated scatterer. The selection criterion of such a range cell is discussed. If there is no isolated scatterer, we propose two cross-range motion parameters measurement algorithms, one based on array processing of the range profile and another based on correlation of ISAR images of the different antennas. Although the correlation based method will be computationally intensive due to the searching of the cross-range motion parameters and ISAR imaging at each searching step, the burden can be reduced by using the computationally efficient array processing method to provide an initial search value.

A new problem of the antenna array configuration is the coordinate registration problem for scatterers in a synthesis scatterer. Assuming that there are  $m$  physical scatterers projected onto a range-Doppler unit, then in general, there will be  $m$  spatial frequencies on each of the  $x$  and  $z$  directional array. Which is the spatial frequency on each of the two arrays that corresponds to a particular scatterer? This is discussed in Section 2.3.5.

In Section 2.2, the principles and derivations involved in our work, such as the principle of the two-antenna interferometry configuration and antenna array configuration angle measurement setup would be discussed. The envelope alignment, radial motion compensation, cross-range motion compensation methods and imaging algorithms are also discussed. Simulation results are demonstrated subsequently in Section 2.4.

## 2.2 Principle of Cross-range Measurement Method

In this section, the principle of cross-range position measurement of a single scatterer using a narrow band signal is derived. The methods presented include using a two-antenna and an antenna array configuration.

### 2.2.1 Two-Antenna Interferometric Technique

A two-antenna interferometric angle measurement system is shown in Fig. 2.1. The origin of the three-dimensional coordinate system is denoted as  $O$ , and two antennas  $A_1$  and  $A_2$  are located at  $(-d/2, 0, 0)$  and  $(d/2, 0, 0)$  respectively.  $A_1$  acts as the transmitting as well as the receiving antenna, while  $A_2$  is the receiving antenna and  $d$  is the distance between the two antennas. A point target  $P$  with coordinates  $(x, y, z)$  is located at the broadside of the two antennas.

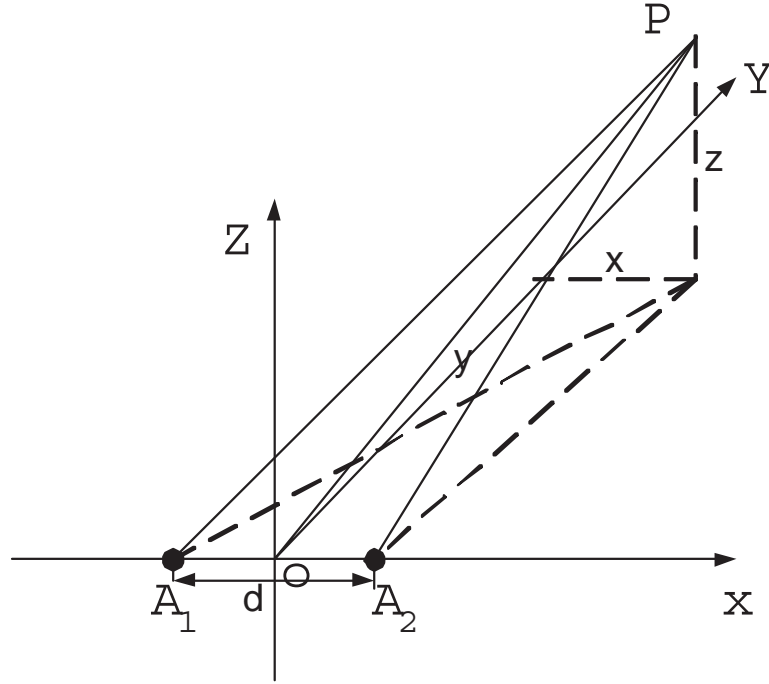


Fig. 2.1: Geometry of the two-antenna cross-range measurement system.

Let the transmitted signal from antenna  $A_1$  be  $\tilde{s}(t) = \exp(j2\pi ft)$ . The received signals at antennas  $A_1$  and  $A_2$  backscattered from the target are

$$s_1(t) = \exp\left(j2\pi f\left(t - \frac{2R_1}{c}\right)\right) \quad (2.1)$$

and

$$s_2(t) = \exp\left(j2\pi f\left(t - \frac{R_1 + R_2}{c}\right)\right) \quad (2.2)$$

respectively, where  $R_1 = |PA_1|$ ,  $R_2 = |PA_2|$ ,  $c$  is the speed of light and  $f$  is the

carrier frequency. For simplicity, we ignore the effects of path loss and we have

$$s_1^*(t)s_2(t) = \exp\left(j2\pi f \frac{R_1 - R_2}{c}\right). \quad (2.3)$$

The difference in distance between  $R_1$  and  $R_2$  is

$$\begin{aligned} \Delta R &= R_1 - R_2 \\ &= \sqrt{((x + d/2)^2 + y^2 + z^2)} \\ &\quad - \sqrt{((x - d/2)^2 + y^2 + z^2)} \\ &= \frac{(x + d/2)^2 - (x - d/2)^2}{R_1 + R_2} \\ &= \frac{2xd}{R_1 + R_2}. \end{aligned} \quad (2.4)$$

Let us consider the suitability of approximating  $2xd/(R_1 + R_2)$  by  $xd/R_1$ ,

$$\begin{aligned} \frac{2xd/(R_1 + R_2) - xd/R_1}{2xd/(R_1 + R_2)} &= 1 - \frac{R_1 + R_2}{2R_1} \\ &= \frac{R_1 - R_2}{2R_1} = \frac{xd}{R_1(R_1 + R_2)} \\ &< \frac{d}{R_1 + R_2}. \end{aligned} \quad (2.5)$$

The result of (2.5) shows that for the far field region, the relative difference between  $2xd/(R_1 + R_2)$  and  $xd/R_1$  is a small value, therefore  $\Delta R$  can be approximated by  $xd/R_1$ .

Consider another point  $Q(x, y', z')$  where  $R'_1 = |QA_1|$  and  $R'_2 = |QA_2|$ , the difference in distance between  $R'_1$  and  $R'_2$  is

$$\Delta R' = R'_1 - R'_2 = \frac{2xd}{R'_1 + R'_2}. \quad (2.6)$$

Having obtained  $\Delta R$  and  $\Delta R'$ , we have

$$\begin{aligned} & \left| \frac{\Delta R - \Delta R'}{\Delta R} \right| \\ &= \frac{R'_1 - R_1 + R'_2 - R_2}{R'_1 + R'_2} \\ &= \frac{(x + d/2)^2 + y'^2 + z'^2 - [(x + d/2)^2 + y^2 + z^2]}{(R'_1 + R'_2) \times (R'_1 + R_1)} \\ & \quad + \frac{(x - d/2)^2 + y'^2 + z'^2 - [(x - d/2)^2 + y^2 + z^2]}{(R'_1 + R'_2) \times (R'_2 + R_2)} \\ &= \frac{y'^2 - y^2 + z'^2 - z^2}{(R'_1 + R'_2) \times (R'_1 + R_1)} + \frac{y'^2 - y^2 + z'^2 - z^2}{(R'_1 + R'_2) \times (R'_2 + R_2)} \\ &< \frac{\Delta y + \Delta z}{R}, \end{aligned} \quad (2.7)$$

where  $R = \min \{R_1, R_2, R'_1, R'_2\}$ ,  $\Delta z = |z - z'|$ ,  $\Delta y = |y - y'|$ .

It can be seen that the relative difference  $|\frac{\Delta R - \Delta R'}{\Delta R}|$  is much smaller than 1 when  $\Delta y, \Delta z \ll R$ . Since we are only interested in large values of  $R$ , therefore in our range of interest ( $\Delta y, \Delta z \ll R$ ), the difference in distance between  $R_1$  and  $R_2$  is largely dependent on  $x, R$  and  $d$ ; and approximately independent of  $z$  and  $y$ .

Let  $\varphi$  denote the phase of  $s_1^*(t)s_2(t)$ ,

$$\varphi \simeq 2\pi f \times \frac{xd}{Rc} = \frac{2\pi xd}{R\lambda}, \quad (2.8)$$

and after rearranging, we have

$$x \simeq \frac{\varphi \lambda R}{2\pi d}. \quad (2.9)$$

The value of  $x$  can be estimated from the phase of  $s_1^*(t)s_2(t)$ . However, since the phase is of modulo  $2\pi$ , we must make sure that  $|\frac{2\pi xd}{\lambda R}| < \pi$  holds in order to ensure that there exists an unique relation between  $x$  and  $\varphi$ . Therefore, the cross-range unambiguous window is

$$x \in X = [-\frac{\lambda R}{2d}, \frac{\lambda R}{2d}]. \quad (2.10)$$

For example, in the case where  $f = 10GHz$ ,  $d = 1m$  and  $R = 10km$ , the unambiguous distance will be  $\lambda R/d = 300m$ .

### 2.2.2 Antenna Array Technique

The L-shape antenna array configuration is shown in Fig. 2.2. It can also be of a cross shape where the antenna elements extends to the negative x and z-axis. Let the transmitting antenna be at the origin and the  $2K - 1$  receiving antennas be located at  $(kd, 0, 0)$  and  $(0, 0, kd)$  where  $k = 0 : K - 1$ .

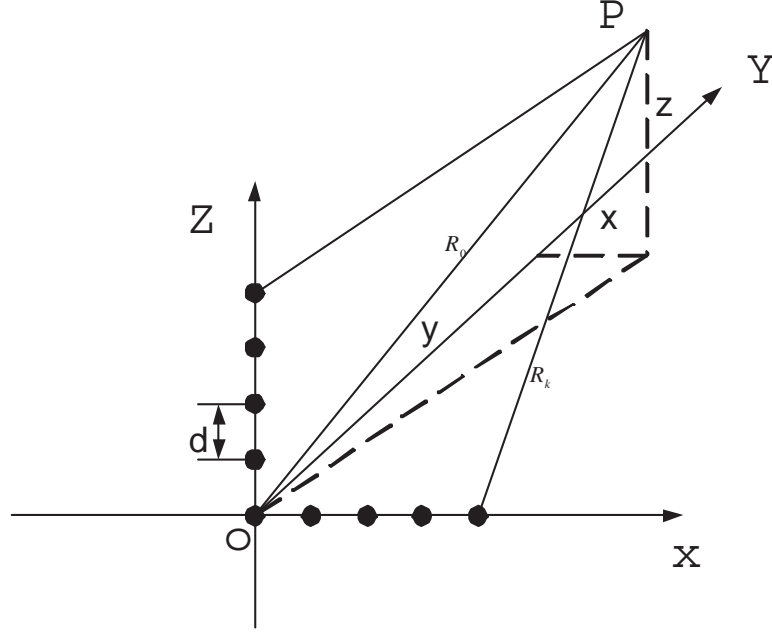


Fig. 2.2: Geometry of the L-shape antenna array imaging system.

The difference in distance between point  $P$  to the reference antenna at the origin( $0^{th}$  antenna) and point  $P$  to the  $k^{th}$  antenna in the x-axis direction is

$$\begin{aligned}
 \Delta R_k &= R_0 - R_k \\
 &= \frac{x^2 + y^2 + z^2 - ((x - kd)^2 + y^2 + z^2)}{R_0 + R_k} \\
 &= \frac{2xkd}{R_0 + R_k} - \frac{k^2 d^2}{R_0 + R_k}
 \end{aligned} \tag{2.11}$$

It can be seen that apart from the near constant term  $\frac{k^2 d^2}{R_0 + R_k}$  (which is nearly independent of  $x$ ),  $\Delta R_k$  is an approximately linear function of  $k$ . Since  $d$  is known and  $R_0$  and  $R_k$  can be estimated by a wideband signal (by measuring the round trip time delay for the signal to propagate to point  $P$  and back),  $\frac{k^2 d^2}{R_0 + R_k}$  is approximately

known and can be compensated. The received array signal can then be expressed as

$$\mathbf{s} = s_0(t) \times [1, e^{j2\pi \frac{xdk}{\lambda R}}, \dots, e^{j2\pi \frac{xd(K-1)}{\lambda R}}]^T, \quad (2.12)$$

where  $s_0(t)$  is the received signal of antenna 0. The spatial frequency is

$$f_s = xd/(\lambda R). \quad (2.13)$$

Having obtained the spatial frequency, it is easy to get the cross-range distance  $x$ ,

$$x = \frac{\lambda R}{d} f_s. \quad (2.14)$$

Similarly, we can get the  $z$  coordinate of a scatterer using the antenna array on the  $z$  axis. After we have obtained the  $x$  and  $z$  coordinates of a scatterer and together with the range information, the three-dimensional coordinates can be obtained.

The above method looks like the linear array direction-of-arrival(DOA) estimation method. In linear array DOA estimation, the angle is limited to  $[0, \pi]$ . In order to ensure that there is no ambiguity in the DOA estimation,  $d \leq \lambda/2$  must be fulfilled. For the array configuration discussed in this chapter, the cosine value of the unambiguous angle is limited to  $\frac{x}{R} = [-\frac{\lambda}{2d}, \frac{\lambda}{2d}]$  and the phase compensation of  $\frac{\pi k^2 d^2}{\lambda R}$  must be carried out when the values of  $k, d$  are large and/or  $\lambda, R$  are small.



However, for the case of conventional DOA estimation, since  $d = \lambda/2$ , therefore

$\varphi = \frac{\pi k^2 d^2}{\lambda R} = \frac{\pi k^2 \lambda}{4R}$  is a small value in the far field and can be omitted.

As the unambiguous distance is  $\lambda R/d$ , the cross-range resolution is  $\lambda R/(K \times d)$  if conventional Fourier analysis is used. Generally, many antennas are required to attain fine resolution. However, if super-resolution spectrum analysis such as the RELAX[29] and maximum likelihood methods[74] are used, the required number of antennas can be reduced.

## 2.3 Three-dimensional Imaging Based on Array DOA Estimation

In the previous section, we have described the cross-range coordinate measurement of a single scatterer by using an antenna array transmitting a narrow band signal. In this section, we discuss the coordinates measurement method for multiple scatterers using a wideband signal.

### 2.3.1 Wideband Signal Model

Let the transmitted wideband linear frequency modulated signal be

$$\tilde{s}(t) = \tilde{\chi}(t) \exp \left\{ j2\pi \left( ft + \frac{\mu}{2} t^2 \right) \right\}, |t| < \frac{T}{2}, \quad (2.15)$$

where  $f$  is the carrier frequency,  $\mu$  is the chirp rate and  $T$  is the chirp pulse duration.  $\tilde{\chi}(t)$  is the envelope of the transmitted signal which satisfies  $\tilde{\chi}(t) = 1$ , for  $|t| < \frac{T}{2}$ , and  $\tilde{\chi}(t) = 0$ , for  $|t| > \frac{T}{2}$ .

The received signal is

$$s(t) = \rho \times \tilde{\chi}(t - \tau) \exp \left\{ j2\pi \left[ f(t - \tau) + \frac{\mu}{2} (t - \tau)^2 \right] \right\}. \quad (2.16)$$

After demodulation and pulse compression, the received signal can be expressed as [68]

$$\begin{aligned} s(t) &= \rho \times \tilde{\chi}(t - \tau) \exp(-j2\pi f\tau) \\ &\quad \times (T - |t - \tau|) \times \text{sinc}(\mu(T - |t - \tau|)(t - \tau)) \\ &= \chi(t - \tau) \exp(-j2\pi f\tau), \end{aligned} \quad (2.17)$$

where  $\text{sinc}(x) = \frac{\sin(\pi x)}{\pi x}$  and  $\chi(t) = \tilde{\chi}(t)(T - |t|) \times \text{sinc}(\mu(T - |t|)t)$  describes the

envelope after the pulse compression. For simplicity, we consider only two scatterers. Let the coordinates of scatterers  $P$  and  $Q$  at time 0 be  $(x_p, y_p, z_p)$  and  $(x_q, y_q, z_q)$  respectively. The distance moved at time  $t$  are  $x_p(t), y_p(t), z_p(t)$  and  $x_q(t), y_q(t), z_q(t)$ . For rigid target and small angle imaging conditions, we have  $x_p(t) \approx x_q(t)$ ,  $y_p(t) \approx y_q(t)$  and  $z_p(t) \approx z_q(t)$ . The distance from  $P$  and  $Q$  to the origin is denoted as  $r_p(t)$  and  $r_q(t)$  respectively.

According to (2.11), (2.12) and (2.17), the backscattered array signal from  $P$  and  $Q$  can be expressed in the form as shown in (2.18) to (2.21).

Our objective is to obtain the coordinates of  $x_p, x_q, y_p, y_q, z_p, z_q$  or their relative difference in position and the power of  $\alpha_p, \alpha_q$  from the received signals. The processing steps involved include envelope alignment, motion compensation, ISAR imaging and cross-range position estimation.

### 2.3.2 Envelope Alignment

In ISAR imaging, the first step is envelope alignment. As seen in (2.18) to (2.21), since the delay is time varying, the echos' envelopes shift with time. Cross-range signal processing can only be done after the signals' envelopes  $\chi(t - \tau)$  are aligned. For the multiple antenna case, we need to know whether the different antennas' one-dimensional range profiles are aligned at every time instance.

$$\mathbf{s}_{px}(t) = \alpha_p \times e^{-j4\pi r_p(t)/\lambda} \times \begin{bmatrix} \chi\left(t - \frac{2r_{p,0}(t)}{c}\right) \times 1 \\ \chi\left(t - \frac{r_{p,0}(t)+r_{p,1}(t)}{c}\right) \times e^{j2\pi \frac{(x_p+x_p(t))d}{\lambda R}} - j\pi \frac{d^2}{\lambda R} \\ \vdots \\ \chi\left(t - \frac{r_{p,0}(t)+r_{p,K-1}(t)}{c}\right) \times e^{j2\pi \frac{(x_p+x_p(t))(K-1)d}{\lambda R}} - j\pi \frac{(K-1)^2 d^2}{\lambda R} \end{bmatrix} \quad (2.18)$$

$$\mathbf{s}_{qx}(t) = \alpha_q \times e^{-j4\pi r_q(t)/\lambda} \times \begin{bmatrix} \chi\left(t - \frac{2r_{q,0}(t)}{c}\right) \times 1 \\ \chi\left(t - \frac{r_{q,0}(t)+r_{q,1}(t)}{c}\right) \times e^{j2\pi \frac{(x_q+x_q(t))d}{\lambda R}} - j\pi \frac{d^2}{\lambda R} \\ \vdots \\ \chi\left(t - \frac{r_{q,0}(t)+r_{q,K-1}(t)}{c}\right) \times e^{j2\pi \frac{(x_q+x_q(t))(K-1)d}{\lambda R}} - j\pi \frac{(K-1)^2 d^2}{\lambda R} \end{bmatrix} \quad (2.19)$$

$$\mathbf{s}_{pz}(t) = \alpha_p \times e^{-j4\pi r_p(t)/\lambda} \times \begin{bmatrix} \chi\left(t - \frac{2r_{p,0}(t)}{c}\right) \times 1 \\ \chi\left(t - \frac{r_{p,0}(t)+r_{p,1}(t)}{c}\right) \times e^{j2\pi \frac{(z_p+z_p(t))d}{\lambda R}} - j\pi \frac{d^2}{\lambda R} \\ \vdots \\ \chi\left(t - \frac{r_{p,0}(t)+r_{p,K-1}(t)}{c}\right) \times e^{j2\pi \frac{(z_p+z_p(t))(K-1)d}{\lambda R}} - j\pi \frac{(K-1)^2 d^2}{\lambda R} \end{bmatrix} \quad (2.20)$$

$$\mathbf{s}_{qz}(t) = \alpha_q \times e^{-j4\pi r_q(t)/\lambda} \times \begin{bmatrix} \chi\left(t - \frac{2r_{q,0}(t)}{c}\right) \times 1 \\ \chi\left(t - \frac{r_{q,0}(t)+r_{q,1}(t)}{c}\right) \times e^{j2\pi \frac{(z_q+z_q(t))d}{\lambda R}} - j\pi \frac{d^2}{\lambda R} \\ \vdots \\ \chi\left(t - \frac{r_{q,0}(t)+r_{q,K-1}(t)}{c}\right) \times e^{j2\pi \frac{(z_q+z_q(t))(K-1)d}{\lambda R}} - j\pi \frac{(K-1)^2 d^2}{\lambda R} \end{bmatrix} \quad (2.21)$$

From (2.11), it can be seen that for conventional three-antenna imaging with parameters that are of interest to us, such as  $|x| < 100m$ ,  $d = 1m \sim 2m$ ,  $R > 10000m$  and range resolution  $\delta r$  being  $0.5m \sim 1m$ , we have  $\Delta R \ll \delta r$ . Therefore, it is usually not necessary to do envelope alignment between different antenna

elements[20]. However, for the proposed antenna array technique, where we may have large values of  $x$ ,  $d$ ,  $K$  and higher range resolution, it may be necessary to do envelope alignment between the different antenna elements. For example, in the case where  $R = 10000m$ ,  $d = 2m$ ,  $K = 8$ , and the target moves a distance of  $300m$  along the  $x$  direction during the data collection duration(the rotated angle is  $1.7189^\circ$ , resulting in a cross-range resolution of  $0.5m$  when the wavelength is  $0.03m$ ), the maximum distance difference  $\Delta R = 300 \times 8 \times 2/10000 = 0.48m$  is then comparable to the range resolution, and therefore, range alignment is needed for the different antennas.

### 2.3.3 Motion Compensation

This section describes motion compensation which consists of two steps, namely radial motion compensation and cross-range motion compensation. If a particular range cell contains an isolated scatterer, the range cell can then be taken as a reference range cell to carry out radial and cross-range motion compensation simultaneously. Otherwise, radial and cross-range motion parameters must be estimated. Let us begin with a discussion of the criteria to determine if there exist a particular range cell that contains an isolated scatterer in the antenna array context, which is similar to conventional ISAR case, followed by the cross-range motion parameters estimation algorithms.

**Criteria to determine if a range cell contains only an isolated scatterer**

The first step is to determine if a range cell contains only one isolated scatterer. The variance criteria is usually used in ISAR imaging. If a range cell contains only an isolated scatterer, the signal power of this range cell is constant with time. Otherwise, the signal will fluctuate due to the phase interference of the different scatterers in the same range cell.

It is commonly known that scatterers located on a line parallel to the rotational axis of the target (relative to the radar) will be projected to the same position unit on the ISAR plane. These scatterers form a synthesis scatterer on the ISAR image. If a particular range cell contains only one such synthesis scatterer, it can also be regarded as a good candidate for radial motion compensation, but not for cross-range motion compensation as the array signal from this range cell is not a sinusoidal signal. If there is only one physical scatterer in a range cell, the received signal of the different antennas will be a complex sinusoidal signal with a constant envelope.

Based on these observations, we proposed that a good choice for the reference range cell to carry out radial and cross-range motion compensation simultaneously should satisfy the conditions that the power should be large, and the signal variance in the slow-time domain as well as in the two antenna array domains should

be small. Here there is an added antenna array domain and hence the requirement that the variance in the two antenna array domains should be small.

### Simultaneous Radial and Cross-range Motion Compensation

In this section, we discuss the situation where there exist an isolated scatterer. Under such condition, simultaneous radial and cross-range motion compensation can be carried out. Assuming that range cell  $m$  contains only one isolated scatterer  $P$ , then the array signal  $\mathbf{s}_{px}(t)$ ,  $\mathbf{s}_{pz}(t)$  can be obtained directly from the range cell  $m$ . Let  $\mathbf{s}_{qx}(t)$  and  $\mathbf{s}_{qz}(t)$  be the signal of scatterer  $Q$ , then

$$\mathbf{s}_{px}^*(t) \odot \mathbf{s}_{qx}(t) = \alpha_p^* \alpha_q \times e^{j4\pi \frac{r_p(t) - r_q(t)}{\lambda}} \times \begin{bmatrix} 1 \\ e^{j2\pi \frac{(x_q - x_p)d}{\lambda R}} \\ \vdots \\ e^{j2\pi \frac{(x_q - x_p)(K-1)d}{\lambda R}} \end{bmatrix} \quad (2.22)$$

$$\mathbf{s}_{pz}^*(t) \odot \mathbf{s}_{qz}(t) = \alpha_p^* \alpha_q \times e^{j4\pi \frac{r_p(t) - r_q(t)}{\lambda}} \times \begin{bmatrix} 1 \\ e^{j2\pi \frac{(z_q - z_p)d}{\lambda R}} \\ \vdots \\ e^{j2\pi \frac{(z_q - z_p)(K-1)d}{\lambda R}} \end{bmatrix} \quad (2.23)$$

where  $\odot$  is the element wise scalar product. In (2.18), the term  $e^{-j4\pi r_p(t)/\lambda}$  can be regarded as being induced by the radial motion of the target relative to antenna 0, while the terms  $e^{j2\pi \frac{x_p(t)(k-1)d}{\lambda R}}$ ,  $e^{j2\pi \frac{x_q(t)(k-1)d}{\lambda R}}$ ,  $e^{j2\pi \frac{z_p(t)(k-1)d}{\lambda R}}$  and  $e^{j2\pi \frac{z_q(t)(k-1)d}{\lambda R}}$  in (2.18) to (2.21) can be regarded as being induced by the target's cross-range motion. It can be seen that the radial and cross-range motion terms are canceled simultaneously. The spatial frequencies of the array signal are  $f_{sx} = \frac{(x_q - x_p)d}{\lambda R}$  and  $f_{sz} = \frac{(z_q - z_p)d}{\lambda R}$ . Therefore,

$$x_q - x_p = \frac{\lambda R f_{sx}}{d} \quad (2.24)$$

$$z_q - z_p = \frac{\lambda R f_{sz}}{d} \quad (2.25)$$

From (2.24) and (2.25), what we obtained are  $x_q - x_p$  and  $z_q - z_p$ , which are the cross-range distances of the scatterer  $Q$  relative to the scatterer  $P$ . This means that point  $P$  is the center of the obtained three-dimensional image in the cross-range domain.

### Radial Motion Compensation

More importantly, we discuss the situation where there is no isolated scatterer as it is commonly the case in real-life target imaging. If there is no isolated scatterer, simultaneous radial and cross-range motion compensation cannot be carried out and therefore, radial and cross-range motion compensation must be carried out separately. There are many radial motion compensation algorithms, such as the



single-scatterer referencing algorithm[12][39], multiple-scatterer algorithm(MSA) and phase gradient autofocus technique. Steinberg had demonstrated that the dominant scatterer algorithm is effective for aircraft imaging in 80% of the experiments when the range resolution was about 1m[39]. These methods will not be discussed here as they are readily available in the references.

### **Cross-range Motion Compensation**

In this section, we discuss the two proposed cross-range motion parameters estimation method, one based on the array processing of one-dimensional range profiles data and the other based on the correlation of ISAR images.

#### **1. Cross-range motion estimation using array processing of one-dimensional range profiles data.**

As the cross-range position corresponds to the spatial spectrum of the array signal, we propose that the spatial spectrum of some range cells be computed first and curve fitting can then be used to obtain the cross-range motion information.

Let  $R(k, m, n)$  be the range profiles after range alignment and radial motion compensation, where  $k$  is the antenna index,  $0 \leq m \leq M - 1$  is the range index and  $0 \leq n \leq N - 1$  is the time index. The cross-range motion compensation can be done as follows:

**Step 1)** For every  $m$ , compute the summation and variance of  $|R(:, m, :)|$ ,  $s(m) = \sum_{k=0}^{K-1} \sum_{n=0}^{N-1} |R(k, m, n)|$  and  $Var(m) = \sum_{k=0}^{K-1} \sum_{n=0}^{N-1} (|R(:, m, :)| - s(m)/(K \times N))^2$ . Let  $\hat{M}$  be the chosen set of range cells with a large summation value and a small variance value.

**Step 2)** For  $0 \leq n \leq N - 1$  and  $m \in \hat{M}$ , calculate the spectrum of  $R(:, m, n)$ ,  $S(:, m, n) = |FFT(R(:, m, n))|$ .

**Step 3)** Carry out correlation and curve fitting to get the spatial frequency of the target at every time instance. For a definite range cell, because the cross-range spatial spectrums of different instances are similar, correlation can be used to estimate the spatial frequency  $\hat{f}_s(m, n)$  at every time instance  $n$  and every  $m \in \hat{M}$ . As there may exist frequency ambiguity, frequency unwrapping is needed. This is similar to the necessity to carry out phase unwrapping in conventional three-antenna imaging when the target moves beyond the unambiguous region.

We also denote  $\hat{f}_s(m, n)$  as the frequency unwrapped spatial frequency. The spatial frequency in every  $m \in \hat{M}$  is then polynomial-fitted and denoted as  $\tilde{f}_s(m, n)$ . Let  $V(m) = \sum_{n=0}^{N-1} (\hat{f}_s(m, n) - \tilde{f}_s(m, n))^2$  be the fitting error. Choose the value of  $\hat{m}$  that satisfies  $\hat{m} = \min_m V(m)$ . Then  $\tilde{f}_s(n) = \tilde{f}_s(\hat{m}, n)$  is the estimated spatial

frequency at every time instance.

**Step 4)** Compute the phase  $\varphi(k, :) = 2\pi\tilde{f}_s(n)k$ .

**Step 5)** Carry out cross-range motion compensation. For  $k = 1 : K - 1$  and  $0 \leq m \leq M - 1$ , compute

$$\hat{R}(k, m, :) = R(k, m, :) * \exp(-j\tilde{\varphi}(k, n)) \quad (2.26)$$

## 2. Cross-range motion parameters estimation using correlation of ISAR images.

If  $x_p(t)$  is a linear function and it is not compensated, then the ISAR image of the  $m^{th}$  antenna will look like the ISAR image of the  $0^{th}$  antenna but shifted in the cross-range direction. If  $x_p(t)$  is a nonlinear function, then in addition to the shift, it will also induce blurring of the ISAR image. According to the analysis above, after correct cross-range motion compensation, the ISAR images of different antennas are aligned, and the correlation between different ISAR images should peak at the actual motion parameters. Based on this observation, we present the following cross-range parameters estimation algorithm. We will only show the computational procedures for the motion parameters in the x-axis direction. The procedures in the z-axis direction is similar.

**Step 1)** Compute the target's cross-range moving position  $x(t) = vt + \frac{1}{2}at^2 + \frac{1}{6}qt^3$ , where  $v$  is speed,  $a$  is acceleration and  $q$  is jerk. It should be noted that the second and even third order term motion parameters could be included in our computation for maneuvering targets.

**Step 2)** Compensate the phase of antennas  $k = 1, 2, \dots, K - 1$  with phase  $\varphi(k, t) = \frac{2\pi kdx(t)}{\lambda R}$ .

**Step 3)** Obtain the ISAR images  $I(k, :, :)$ , where  $k = 0, 1, 2, \dots, K - 1$ , for all the antennas.

**Step 4)** Compute the cross correlation of  $|I(0, :, :)|$  and  $|I(k, :, :)|$  where  $k = 1, 2, \dots, K - 1$ ,

$$\zeta(v, a, q) = \sum_{k=1}^{K-1} \sum_{m=0}^{M-1} \sum_{n=0}^{N-1} (|I(0, m, n)| \times |I(k, m, n)|) \quad (2.27)$$

**Step 5)** Find the peak position. The position  $(v_0, a_0, q_0)$  of the peak of  $\zeta$  corresponds to the estimated motion parameters in the x-axis direction.

One of the disadvantages of this method is the heavy computational burden associated with doing ISAR imaging and correlation at every searching grid. However, the proposed array processing method presented in this chapter can lower the

amount of computation required by providing an initial value. This reduces the boundary of the parameters that one needs to search. The computational burden has also been further reduced as we only carry out ISAR imaging for selected range cells with high power.

### 2.3.4 Cross-range Position Estimation

After motion compensation, the positions of the scatterers can then be estimated. We discuss the estimation of the  $x$  coordinates of the scatterers. Let  $I_x(k, :, :)$  and  $I_z(k, :, :)$  be the ISAR images of the x-directional and z-directional antennas after cross-range motion compensation. Let  $(\hat{m}, \hat{n})$  be the position of a strong scatterer,  $S_x(:, \hat{m}, \hat{n})$  and  $S_z(:, \hat{m}, \hat{n})$  be the spectrum of  $I_x(:, \hat{m}, \hat{n})$  and  $I_z(:, \hat{m}, \hat{n})$  respectively. If there is only one physical scatterer projected onto the  $(\hat{m}, \hat{n})$  position, there will be only one peak in the spectrum  $S_x(:, \hat{m}, \hat{n})$  and  $S_z(:, \hat{m}, \hat{n})$ . Let the peak position of  $S_x(:, \hat{m}, \hat{n})$  be  $\hat{k}$  and the number of Fourier transform points be  $K$ , the discrete frequency will then be  $f_s = \hat{k}/K$ . According to (3.26),  $xd/(\lambda R) = f_s$ , therefore we have

$$x = \frac{\lambda R}{d} \times \hat{k}/K \quad (2.28)$$

Similarly, the  $z$  coordinate can be obtained by considering the ISAR images obtained by antennas in the z-axis direction.

### 2.3.5 Scatterer Registration

With the sets of  $x$  and  $z$  coordinates obtained, the next challenge is on scatterers registration. Here, a scatterer registration method is proposed. If there are more than one physical scatterers projected onto the point  $(\hat{m}, \hat{n})$ , then generally there will be multiple peaks on  $S_x(:, \hat{m}, \hat{n})$  and  $S_z(:, \hat{m}, \hat{n})$ . Which are the two peaks on  $S_x(:, \hat{m}, \hat{n})$  and  $S_z(:, \hat{m}, \hat{n})$  that correspond to one scatterer? As these physical scatterers must be located on a line parallel to the rotational axis in order to be projected onto the same range-Doppler unit, their projection onto the  $x$  and  $z$  axis maintains a monotonic relative positions relationship. Assuming the  $\hat{K}$  peak values on  $S_x(:, \hat{m}, \hat{n})$  and  $S_z(:, \hat{m}, \hat{n})$  are denoted by  $a(1), a(2), \dots, a(\hat{K})$  and  $b(1), b(2), \dots, b(\hat{K})$ , respectively. The registration decision may be  $a(1) \rightarrow b(1), \dots, a(\hat{K}) \rightarrow b(\hat{K})$ , or  $a(1) \rightarrow b(\hat{K}), \dots, a(\hat{K}) \rightarrow b(1)$ .

As the amplitude of a scatterer's signal obtained in two antenna array domain is the same, we have the following amplitude matching criterion. If  $\sum_{k=1}^{\hat{K}} a(k) \times b(k) > \sum_{k=1}^{\hat{K}} a(k) \times b(\hat{K} - k)$ , then we choose the  $a(1) \rightarrow b(1), \dots, a(\hat{K}) \rightarrow b(\hat{K})$  registration decision, otherwise we choose the  $a(1) \rightarrow b(\hat{K}), \dots, a(\hat{K}) \rightarrow b(1)$  decision.

The above criterion fails for the case where the amplitudes of the scatterers are the same. As the line which contains the true scatterers in the ideal case is parallel

to the axis of rotation, we should choose the line that is closest to being parallel to the axis of rotation as the correct line containing the scatterers. Let  $\vec{\Omega}$  be the unit vector of the rotation axis,  $\mathbf{v}_1$  and  $\mathbf{v}_2$  be the unit vector of two lines for scatterers registration as  $a(1) \rightarrow b(1), \dots, a(\hat{K}) \rightarrow b(\hat{K})$  and  $a(1) \rightarrow b(\hat{K}), \dots, a(\hat{K}) \rightarrow b(1)$ . If  $|\vec{\Omega}^T \mathbf{v}_1| > |\vec{\Omega}^T \mathbf{v}_2|$ , we choose the  $a(1) \rightarrow b(1), \dots, a(\hat{K}) \rightarrow b(\hat{K})$  registration decision, otherwise we choose the  $a(1) \rightarrow b(\hat{K}), \dots, a(\hat{K}) \rightarrow b(1)$  one.

The rotation axis based criterion may fail when there are imaginary scatterers observed during spatial spectrum analysis. For example, let  $Q_1, Q_2$  be two scatterers corresponding to one ISAR image pixel and the frequencies obtained by the two antenna array would be  $[f_{x1}, f_{x2}]$  and  $[f_{z1}, f_{z2}]$ . The combination would give rise to four possible scatterers  $[f_{x1}, f_{z1}], [f_{x2}, f_{z2}], [f_{x1}, f_{z2}]$  and  $[f_{x2}, f_{z1}]$ . Here, two scatterers are imaginary scatterers and non-existent.

The combination of the above two criteria as shown in the following pseudo program code would then produce a better result.

**If**  $\sum_{k=1}^{\hat{K}} a(k) \times b(k) \times \beta > \sum_{k=1}^{\hat{K}} a(k) \times b(\hat{K} - k),$   
*choose the  $a(1) \rightarrow b(1), \dots, a(\hat{K}) \rightarrow b(\hat{K})$  registration decision,*  
**else if**  $\sum_{k=1}^{\hat{K}} a(k) \times b(\hat{K} - k) \times \beta > \sum_{k=1}^{\hat{K}} a(k) \times b(k),$   
*choose the  $a(1) \rightarrow b(\hat{K}), \dots, a(\hat{K}) \rightarrow b(1)$  registration decision.*

*else use rotation axis based criterion.*

*end*

where  $\beta$  is a heuristic selected value, such as  $\beta = 0.8$ .

### 2.3.6 Estimation of the Axis of Rotation

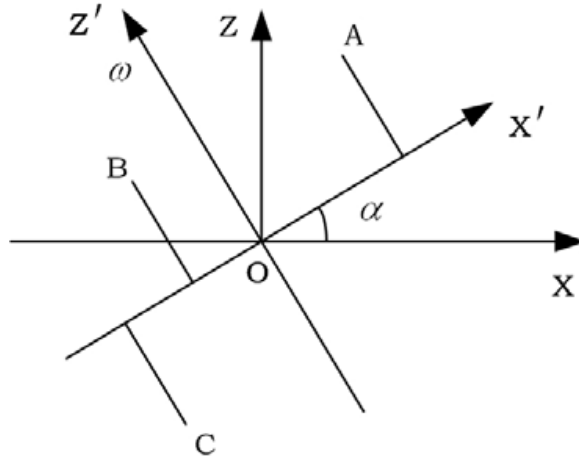


Fig. 2.3: Relation between rotation axis and scatterers coordinates.

Let the target's rotation axis be the  $Z'$  axis. A new coordinate system is  $(X', Z')$ . The rotation angle between the  $X'$  axis and the  $X$  axis is  $\alpha$ . A, B, C are three scatterers. For any scatterer, its coordinates in the  $(X, Z)$  and  $(X', Z')$  coordinate system is denoted as  $(x, z)$  and  $(x', z')$ , respectively. Then

$$\begin{pmatrix} x' \\ z' \end{pmatrix} = \begin{pmatrix} \cos \alpha & \sin \alpha \\ -\sin \alpha & \cos \alpha \end{pmatrix} \begin{pmatrix} x \\ z \end{pmatrix} \quad (2.29)$$



The Doppler frequency of this scatterer is

$$f_d = 2\Omega x' / \lambda = \frac{2\Omega}{\lambda} (\cos \alpha, \sin \alpha) \begin{pmatrix} x \\ z \end{pmatrix} \quad (2.30)$$

where  $\Omega$  is the rotation speed. Therefore  $[-\sin(\alpha), \cos(\alpha)]$  is the unit vector of the rotational axis.

Through ISAR imaging and DOA estimation, the positions and Doppler frequencies of many scatterers can be obtained, then  $\Omega$  and  $\alpha$  can be estimated using the minimum mean square error estimation method. Of course, only scatterers that do not need scatterers registration are useful.

## 2.4 Simulation Results

In this section, some simulations are carried out to verify the effectiveness of our method. In all our simulations, the target is located  $10km$  away from the origin on the  $y$  axis, the transmitted signal's wavelength is  $\lambda = 0.03m$ , the signal bandwidth is  $300MHz$  (range resolution is therefore  $0.5m$ ). There are 8 antennas each in the x-axis and z-axis directions. Antenna 0 is located at the origin. In the first and second examples (target with isolated scatterers and two-ring target respectively), the distance between antenna elements is  $4m$  and the cross-range unambiguous distance is  $75m$ . However, in the third example (aeroplane target),

the chosen distance between antenna elements is  $3m$  so that the cross-range unambiguous distance is  $100m$ , as the target is larger.

Distance to target	10 km
Wavelength	0.03 m
Signal Bandwidth	300 MHz
Resultant range resolution	0.5 m
No. of antenna in each axis(X & Y)	8

Table 2.1: Imaging system parameters.

### 2.4.1 Target with Isolated Scatterer

We first examine the proposed three-dimensional imaging and motion compensation method using the signals of a target which contains an isolated scatterer. The target consists of 7 scatterers located at the local coordinates  $(0, 0, 0; 2, 0, 0; 0, 0, 10; 2, 0, 20; 1, -2, 1; -1, 2, -3; 3, 2, 3)$ . Fig. 2.4 depicts the three-dimensional model of the target while the three different views of the target are shown in Fig. 2.5. In all the plots, the volume of the point is used to express the power of the scatterer, with a higher power being represented by a larger volume.

The target moves along a straight line with speed  $Vx = -63.66m/s$ ,  $Vy = 3m/s$  and  $Vz = 0m/s$ . The data collection time is dependent on the required cross-range resolution. For a target moving with constant velocity, a longer data

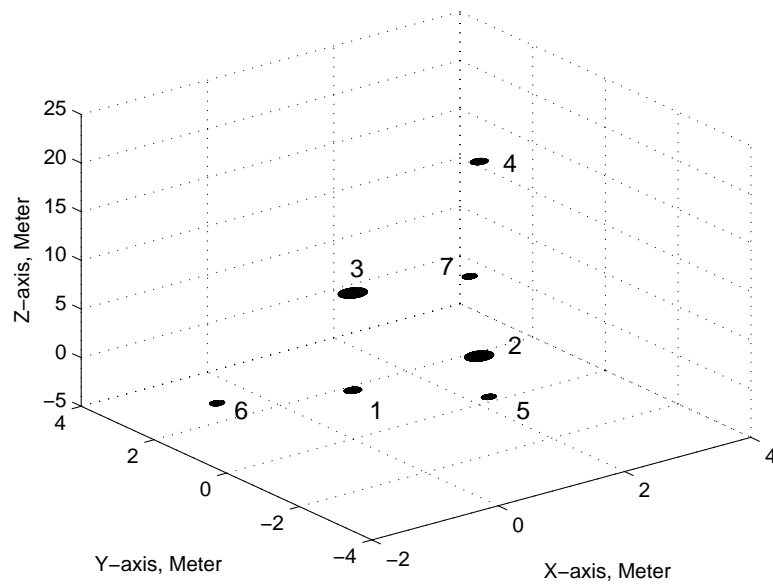


Fig. 2.4: 3D model of the target (target with isolated scatterer).

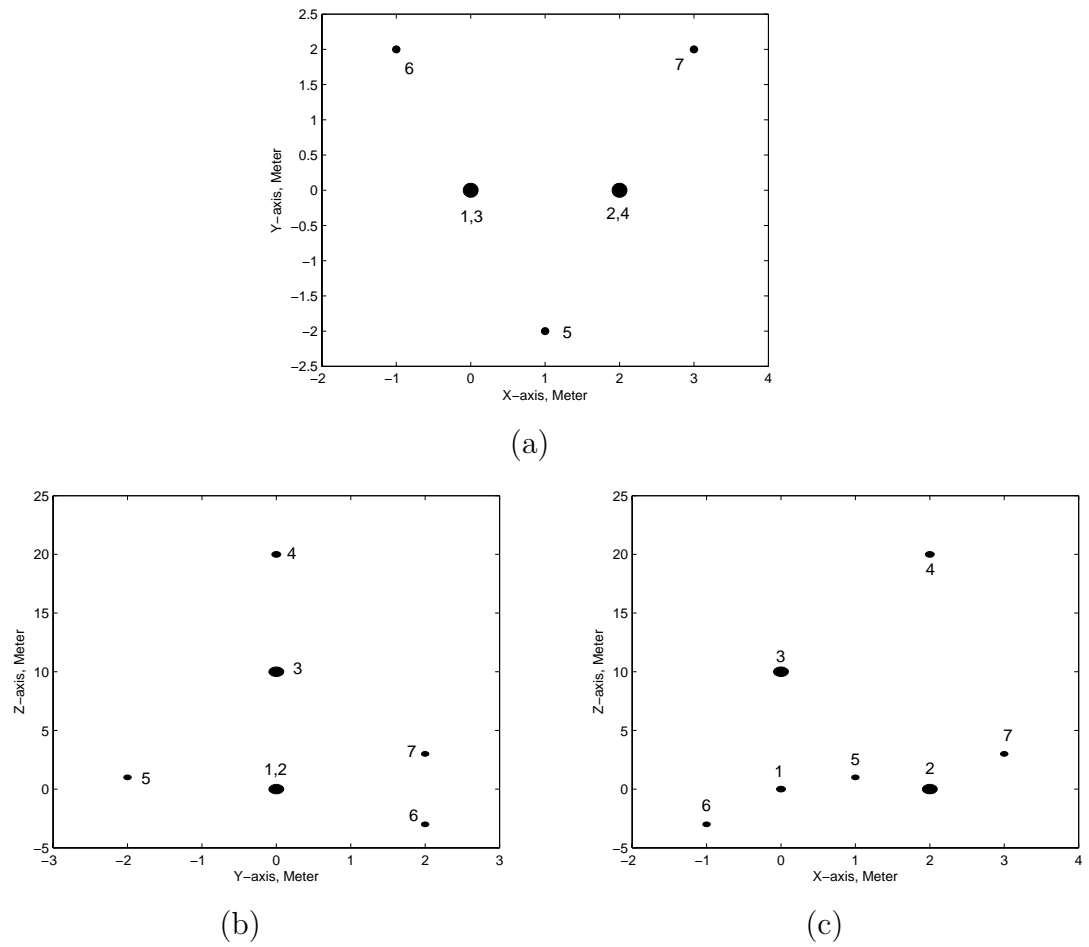


Fig. 2.5: Projected views of the target model (target with isolated scatterer) (a)XY Plane (b)YZ Plane (c)XZ Plane.

collection time allows for better cross-range resolution. In this case, the data collection time is 4.7124s and during this time interval, the cross-range distance moved is 300m, the rotated angle is  $1.7189^\circ$  and the resulting cross-range resolution is 0.5m. There are 8 sampling points in one range cell and match filtering is used to obtain the range profile. The scatterer nearest to the radar is an isolated scatterer, which is used to do radial and cross-range motion compensation. The ISAR image of antenna 0 is shown in Fig. 2.6.

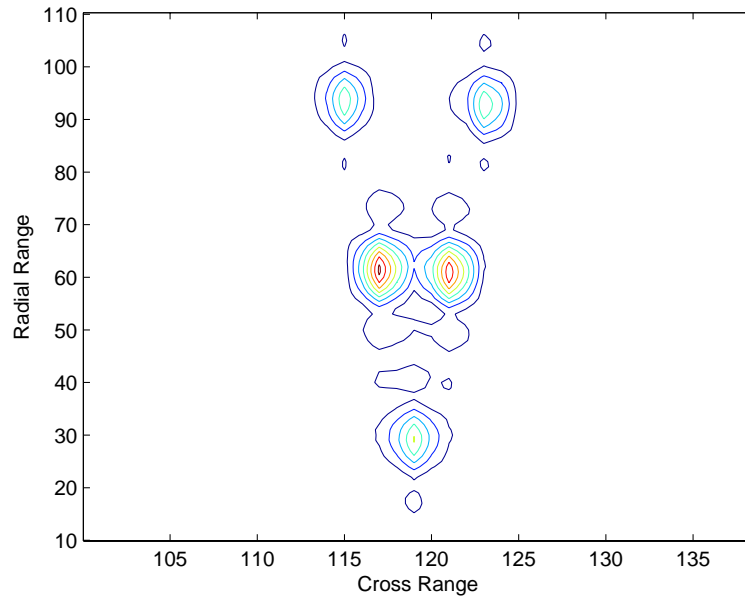


Fig. 2.6: Contour plot of ISAR image (target with isolated scatterer).

The reconstructed three-dimensional image and the three projected image views using antenna array configuration are shown in Fig. 2.7 and Fig. 2.8 respectively. For simplicity of comparison, the reconstructed three-dimensional image using the

three-antenna interferometry technique is shown in Fig. 2.9. It can be seen that as scatterers 1 and 3 have the same x coordinate and y coordinate, and they coincide in the ISAR image. Scatterers 2 and 4 coincide in the ISAR image for the same reason. Using the antenna array configuration, the coordinates of all scatterers are correctly reconstructed. But using the three-antenna interferometry technique, only the positions of scatterers 5, 6 and 7 are correct.

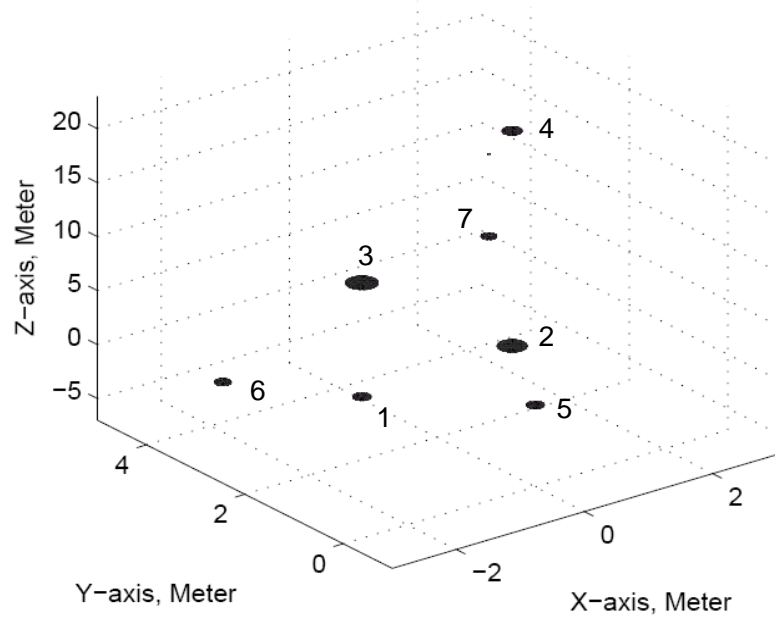


Fig. 2.7: 3D image obtained by the antenna array method (target with isolated scatterer).

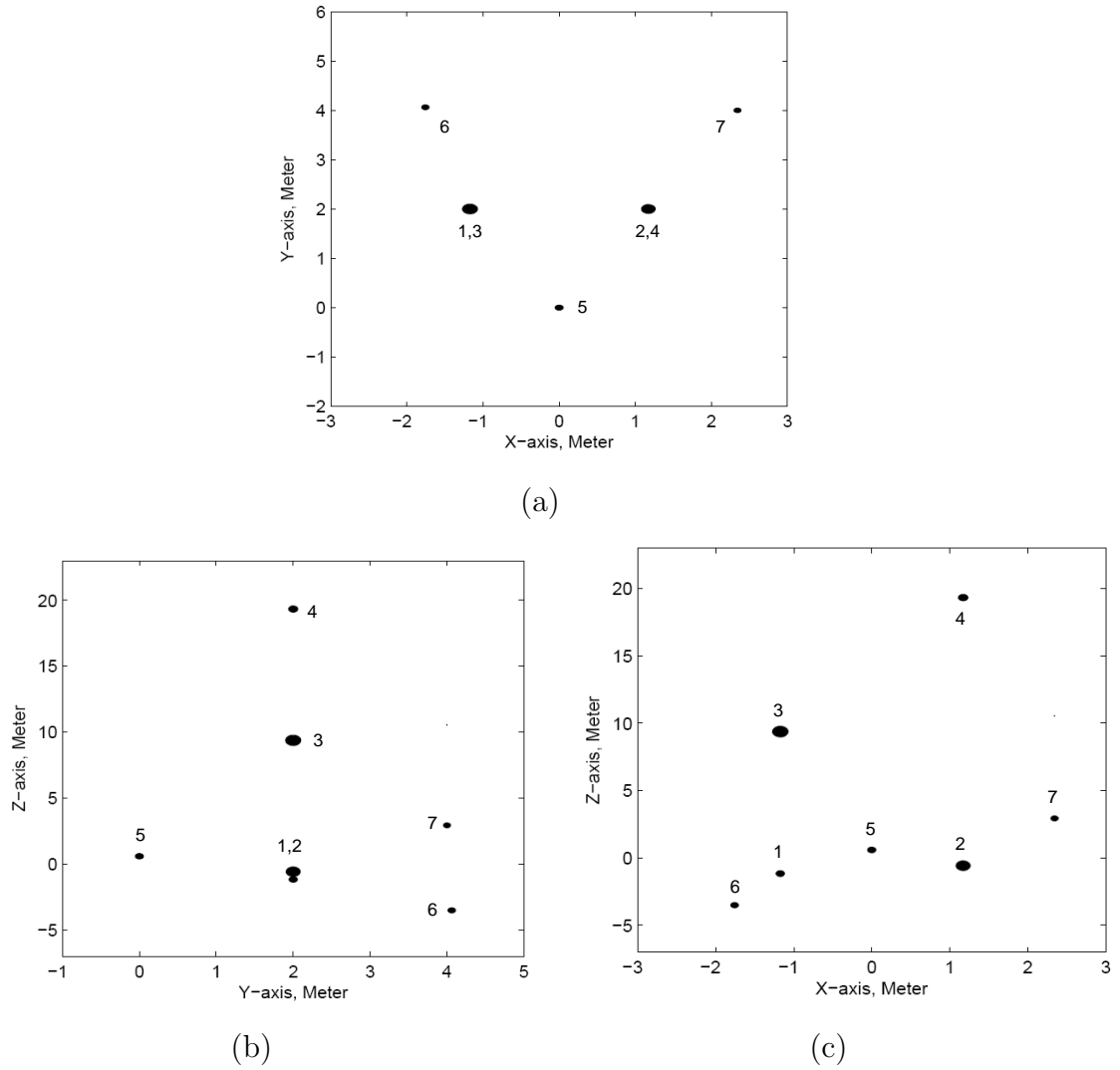


Fig. 2.8: Projected views of the image obtained by the antenna array method (target with isolated scatterer) (a)XY Plane (b)YZ Plane (c)XZ Plane.

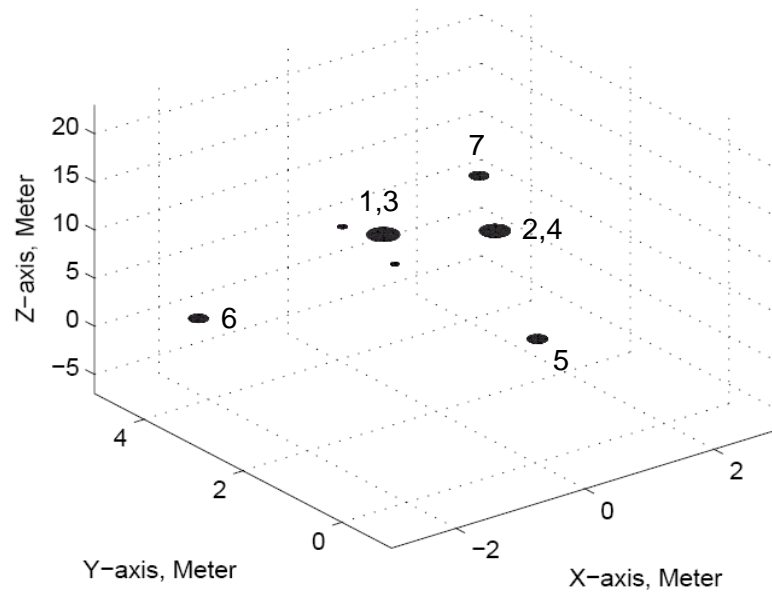


Fig. 2.9: 3D image obtained by three-antenna method (target with isolated scatterer).



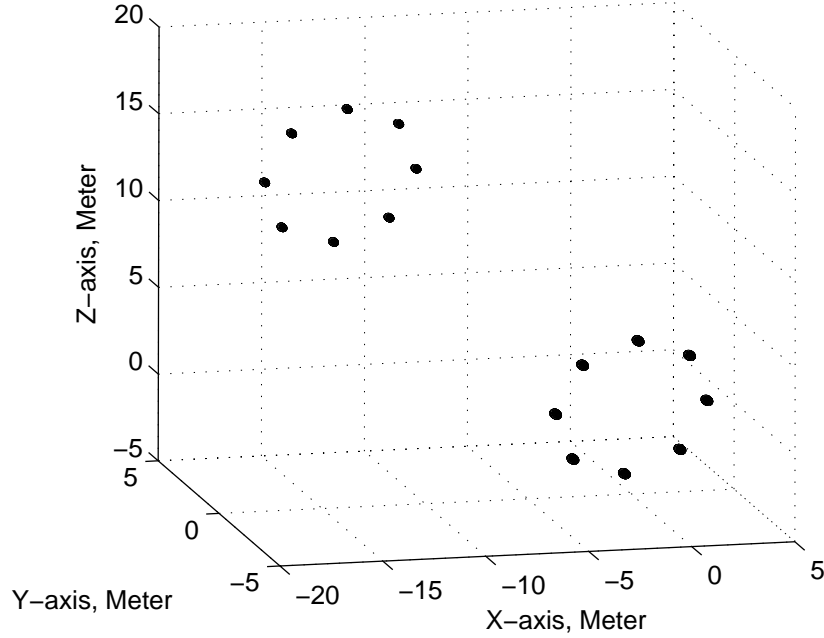


Fig. 2.10: 3D model of the target (two-ring target).

### 2.4.2 Two-ring Target

In this example, we demonstrate the cross-range motion compensation using parameter estimation method based on cross correlation of ISAR images. The target comprises of 16 scatterers and looks like two rings. The radius of each ring is  $4m$ , and the distance between the two rings is  $20m$ . Fig. 2.10 and Fig. 2.11 show the target's three-dimensional model and three projected views, respectively. The target moves along a straight line with speed  $V_x = 63.66m/s$ ,  $V_y = 3m/s$  and  $V_z = 63.66m/s$ . The data collection time is  $4.7124s$ .

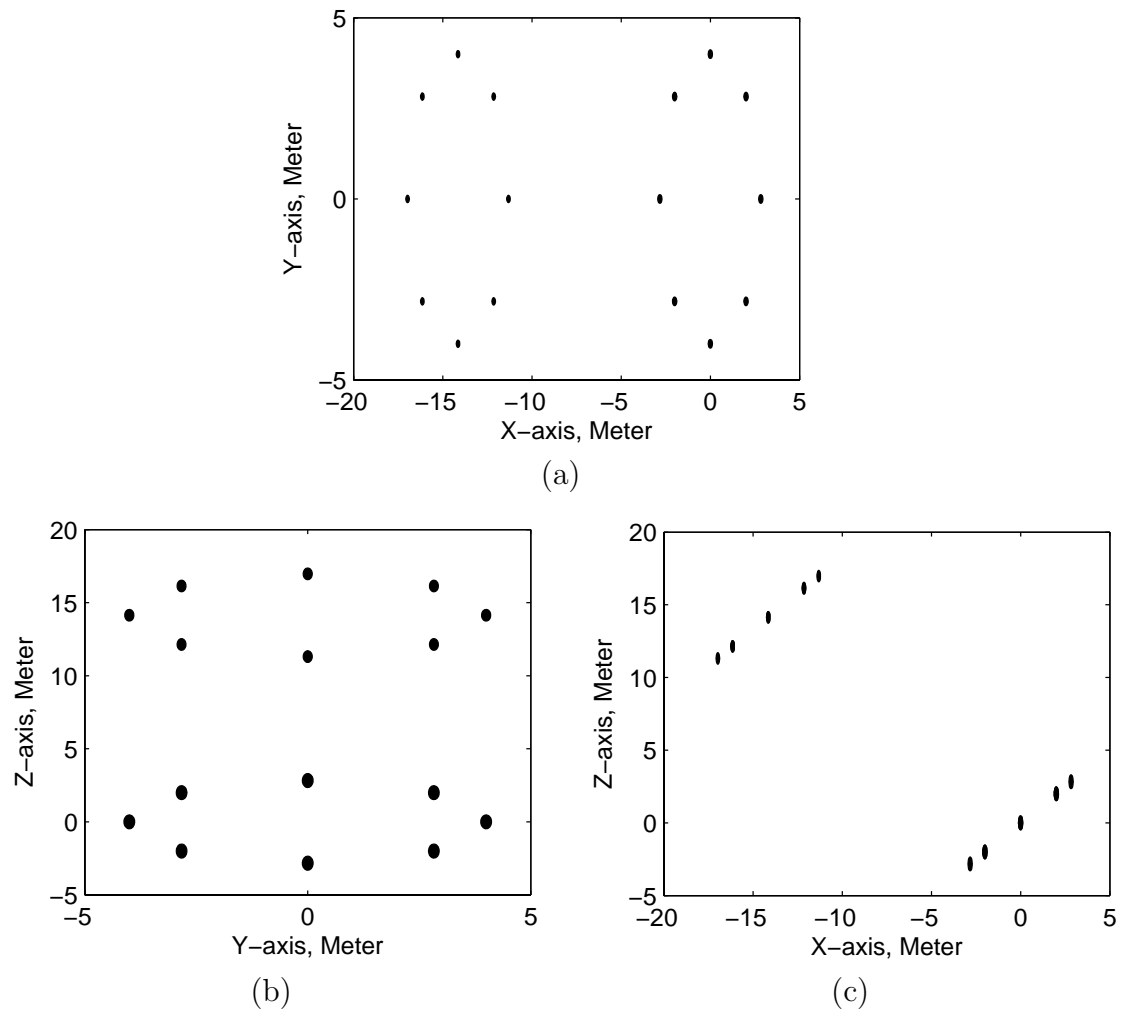


Fig. 2.11: Projected views of the target model (two-ring target) (a)XY Plane (b)YZ Plane (c)XZ Plane.

As the axis of the target is perpendicular to the direction of the target's moving speed, the corresponding points of the two rings are projected onto the same range-Doppler unit and therefore appear as one ring in the ISAR image as shown in Fig. 2.12.

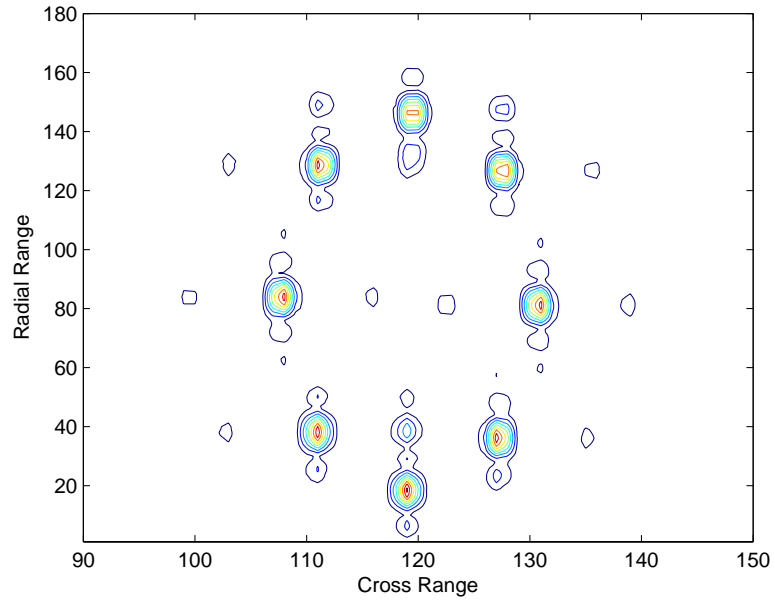


Fig. 2.12: Contour plot of ISAR image (two-ring target).

In this case, there is no range unit with a "physically isolated scatterer" to do radial and cross-range motion compensation simultaneously. However, we can use the so called "synthesis isolated scatterer" to do radial motion compensation. The method of cross-range correlation of ISAR images presented in this chapter is used to estimate the cross-range motion parameters. Fig. 2.13 shows the contour plot of the correlation function of the speed and acceleration in the x direction. The

peak point corresponds to the estimated speed and acceleration, which is equal to the actual value (about  $64\text{m/s}$  and  $0\text{m/s}^2$ , respectively). Fig. 2.14 and Fig. 2.15 show the three-dimensional image and the three projected views of the two rings reconstructed by using the antenna array.

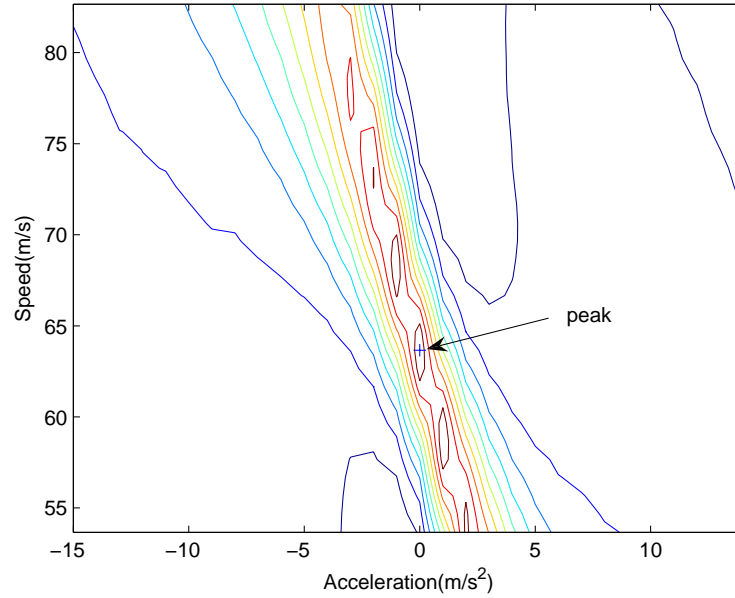


Fig. 2.13: Contour plot of correlation function of the ISAR images of the different antennas (two-ring target).

Fig. 2.14 and Fig. 2.15 are almost identical to the original image shown in Fig. 2.10 and Fig. 2.11. This is due to the spatial separation ability of the antenna array to separate the two rings. The reconstructed three-dimensional image using three-antenna interferometry is shown in Fig. 2.16. The three-dimensional image is different from the original target's image as the obtained  $x$  and  $z$  coordinates is an average of the original  $x$  and  $z$  coordinates and lie somewhere between them.

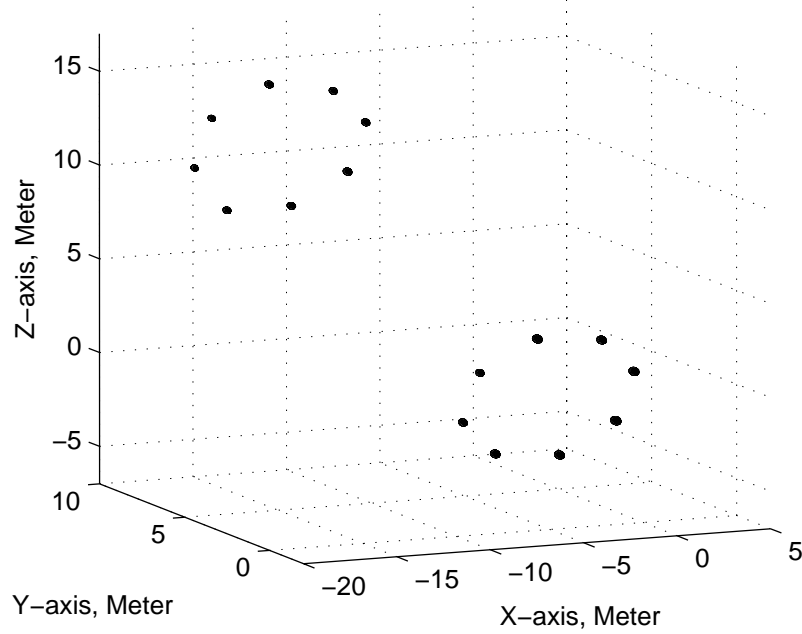


Fig. 2.14: 3D image obtained by the antenna array method (two-ring target).

### 2.4.3 Aeroplane Target

In this example, we demonstrate the cross-range motion compensation using parameter estimation method based on DOA estimation. The target is a complex aeroplane target. Fig. 2.17 and Fig. 2.18 show the target's three-dimensional model and three projected views, respectively.

The target moves along a straight line with speed  $V_x = 100m/s$ ,  $V_y = 3m/s$  and  $V_z = 0m/s$ , and the data collection time is  $3s$ . These true radial motion parameters are used to do radial motion compensation. The ISAR image is shown

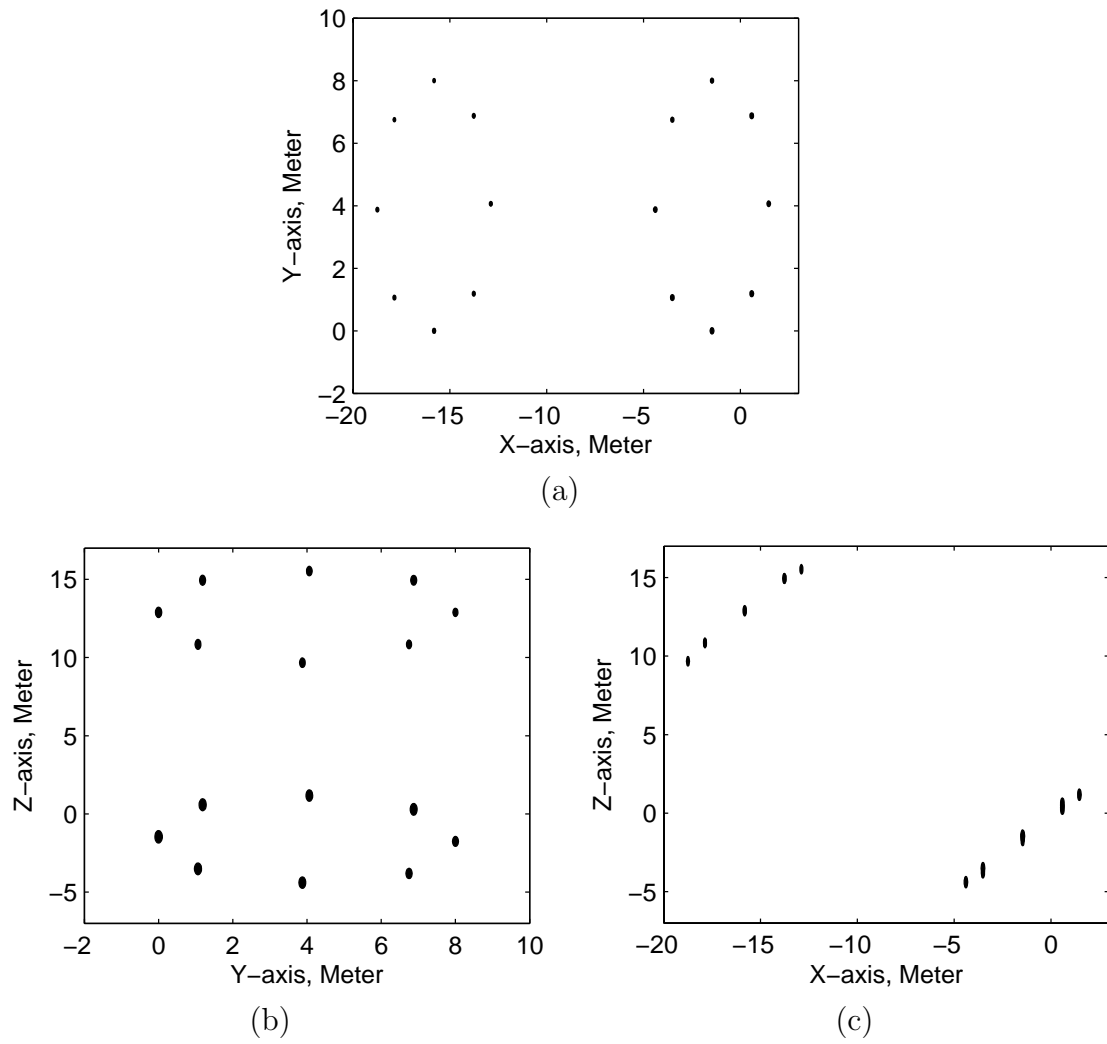


Fig. 2.15: Projected views of the image obtained by the antenna array method (two-ring target) (a)XY Plane (b)YZ Plane (c)XZ Plane.

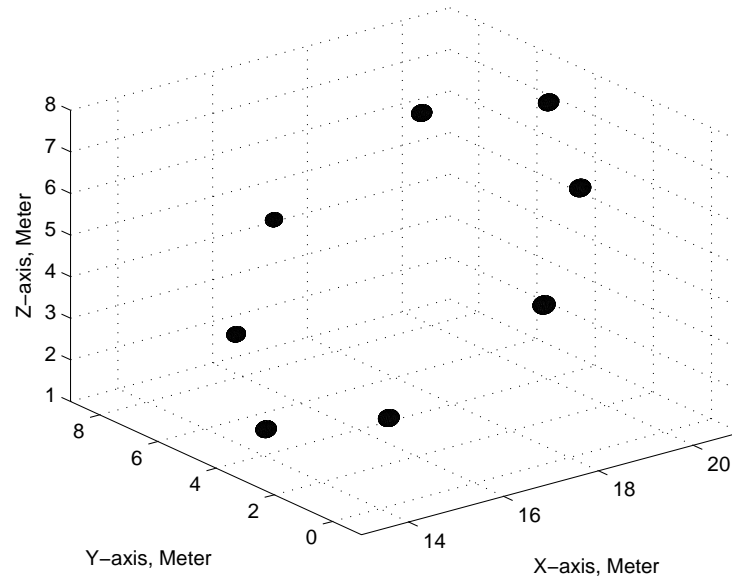


Fig. 2.16: 3D image obtained by the three-antenna method (two-ring target).

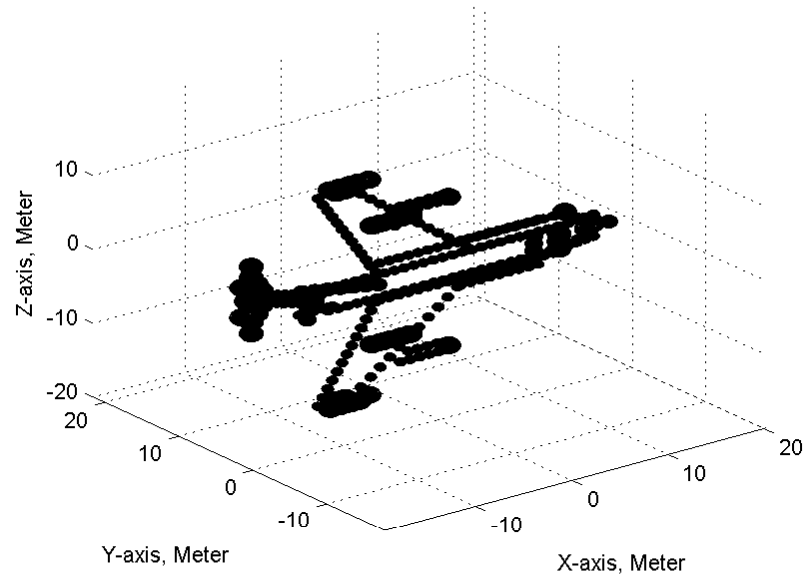


Fig. 2.17: 3D model of the target (aeroplane target).

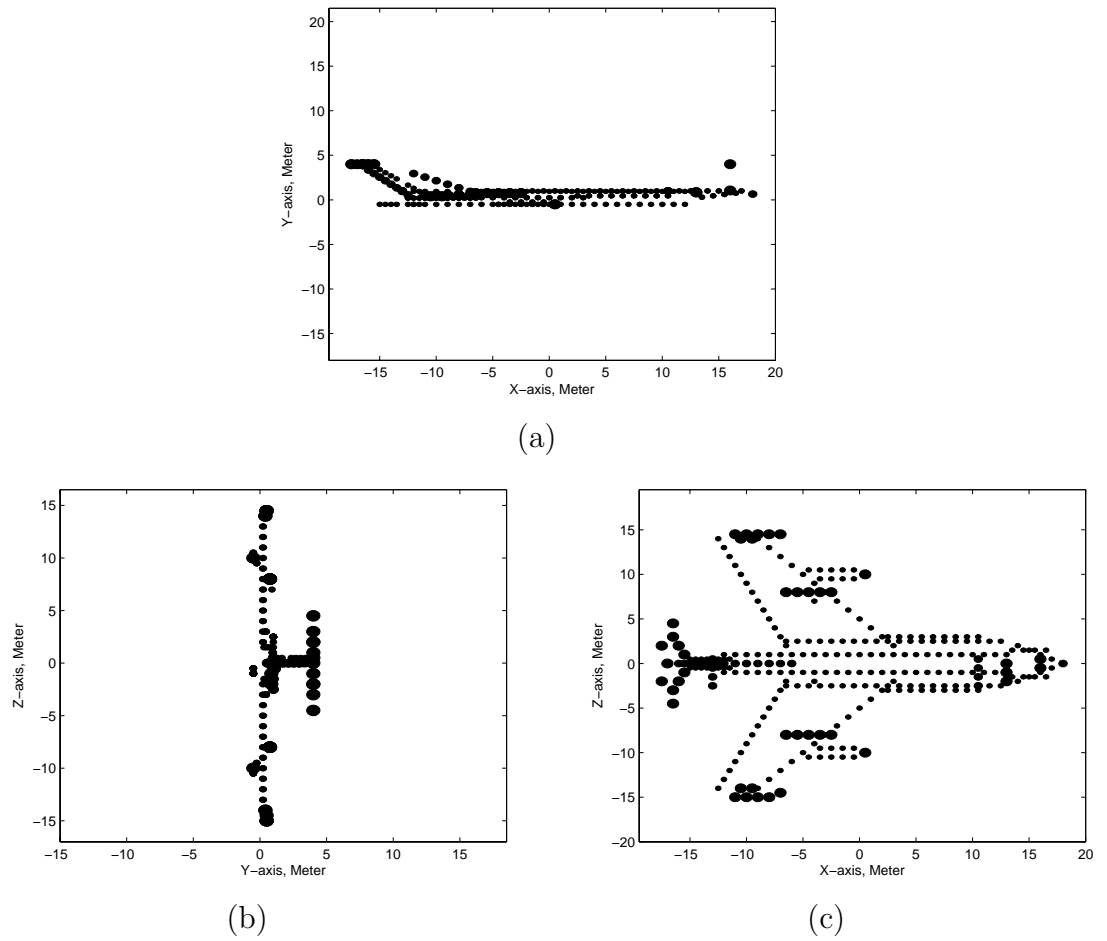


Fig. 2.18: Projected views of the target model (aeroplane target) (a)XY Plane (b)YZ Plane (c)XZ Plane.



in Fig. 2.19 and is similar to Fig. 2.18(a). It can be seen that many scatterers in the  $z$  direction are projected onto the same ISAR image unit.

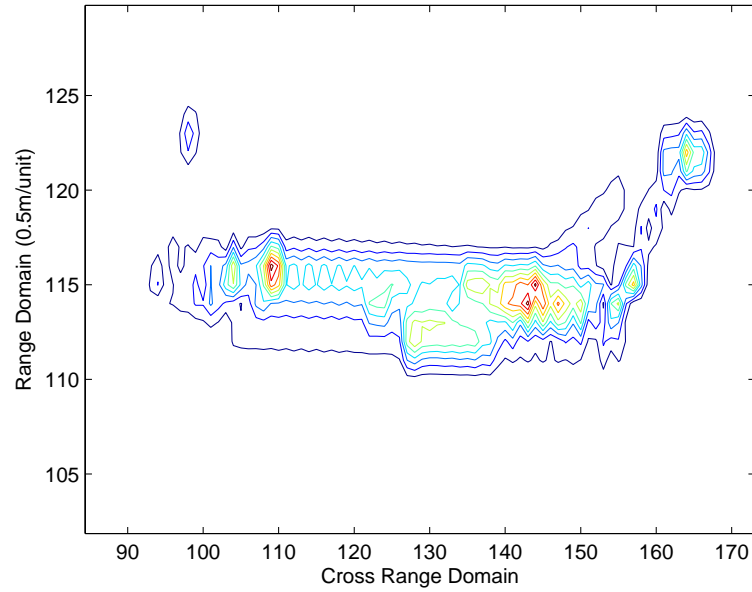


Fig. 2.19: Contour plot of ISAR image (aeroplane target).

Fig. 2.20 and Fig. 2.21 show the estimated cross-range motion in the  $x$  and  $z$  direction and they are approximately straight lines. Fig. 2.22 and Fig. 2.23 show the three-dimensional image and the three projected views of the reconstructed images by using the antenna array method, here we have assumed that there are at most two scatterers in one ISAR unit and the maximum likelihood frequency estimation method has been used[74].

The reconstructed three-dimensional image and three projected views using

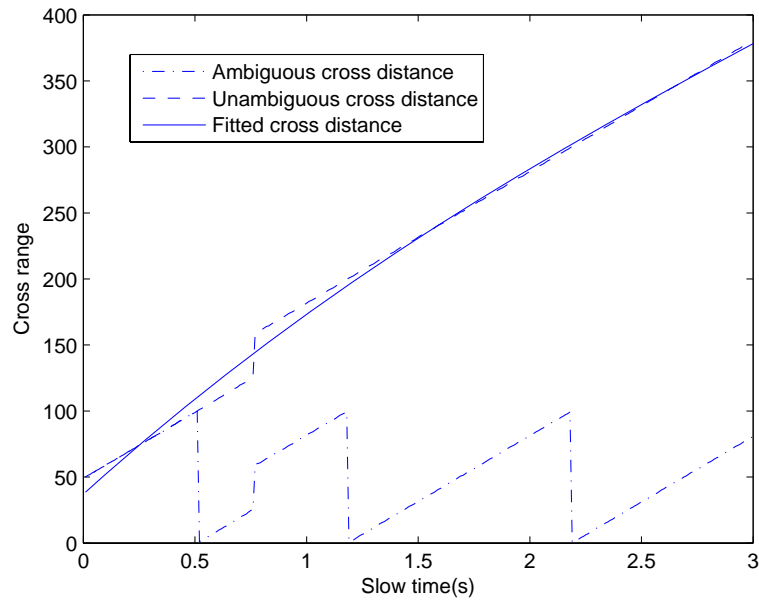


Fig. 2.20: X-direction cross-range estimation plot (aeroplane target).

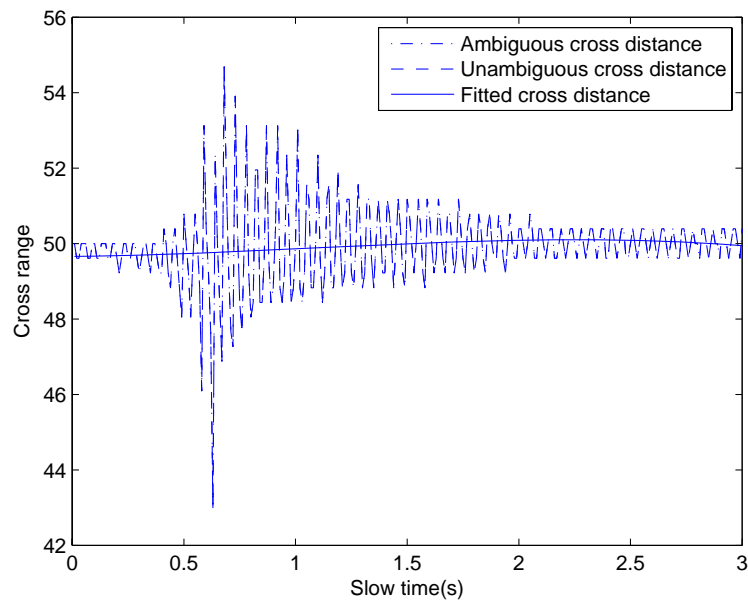


Fig. 2.21: Z-direction cross-range estimation plot (aeroplane target).

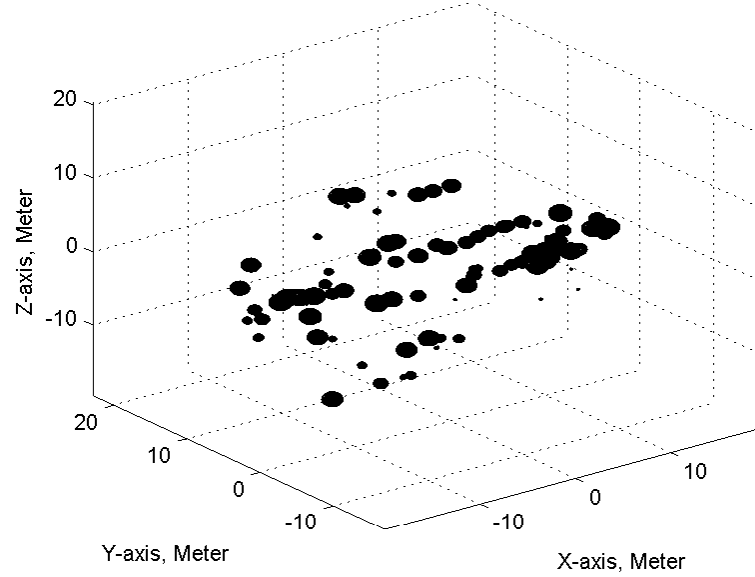


Fig. 2.22: 3D image obtained by the antenna array method (aeroplane target).

the three-antenna interferometry method is also shown in Fig. 2.24 and Fig. 2.25 respectively for comparison purposes.

As there are more scatterers in the  $z$  direction compared to other direction, many of these scatterers are projected onto the same ISAR units. The result is that the three-dimensional image obtained by the three-antenna configuration is poor, especially in the  $z$  direction. The image obtained by the array based configuration has been shown to be significantly better.

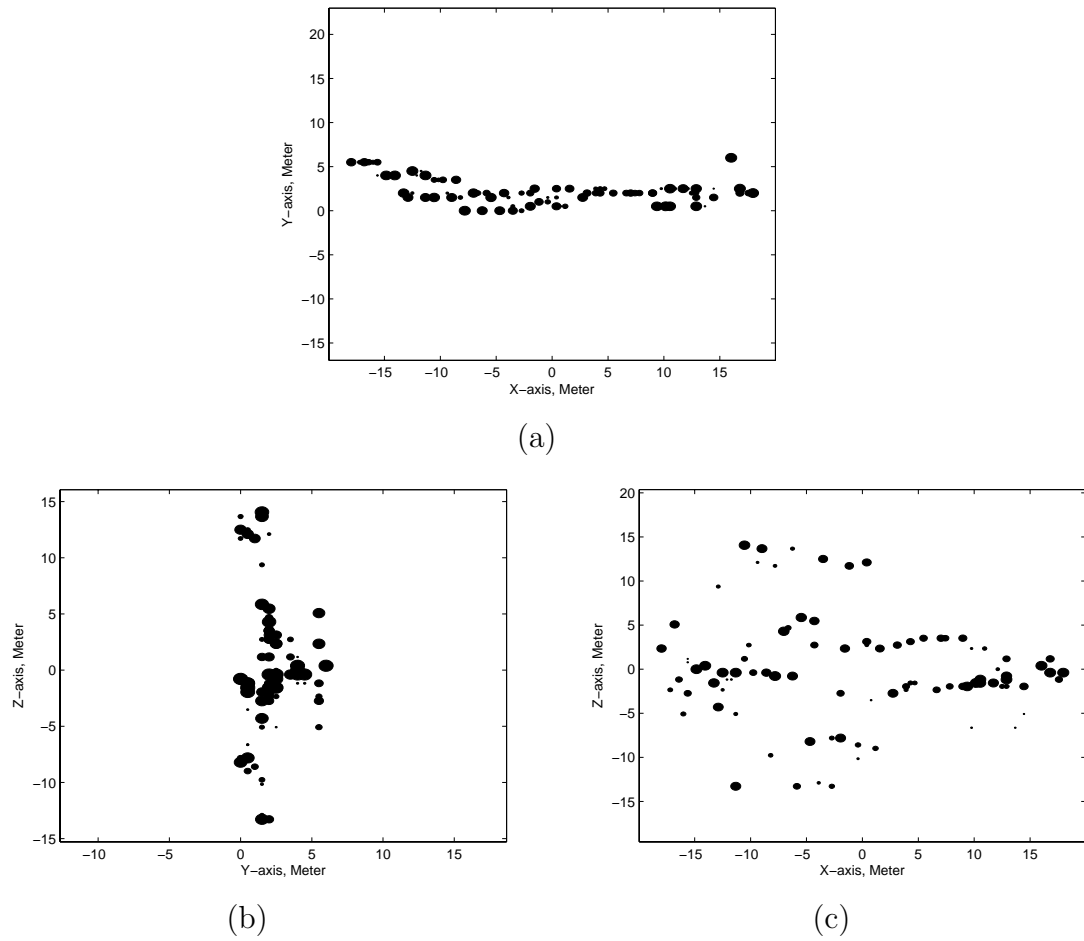


Fig. 2.23: Projected views of the image obtained by the antenna array method (aeroplane target) (a)XY Plane (b)YZ Plane (c)XZ Plane.

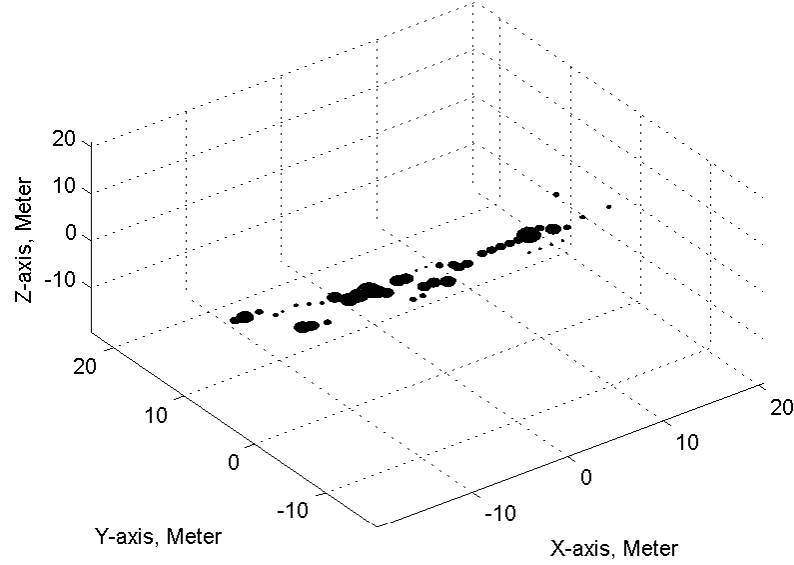


Fig. 2.24: 3D image obtained by the three-antenna method (aeroplane target).

## 2.5 Conclusions

In this chapter, a three-dimensional imaging method using two perpendicular antenna arrays is proposed. The criteria for determining if a particular range cell contains a physically isolated scatterer is also proposed. Translational and cross-range motion can be compensated by the isolated scatterer's signal. In the case where there is no physical isolated scatterer, two cross-range motion parameters estimation methods are proposed, one using array processing to get the spatial frequency (contains cross-range distance information), another doing a parameter search to obtain the peak of the correlation between ISAR images of the different antennas. A scatterer registration strategy has also been proposed. Simulation results have illustrated the effectiveness of the proposed methods as shown by the

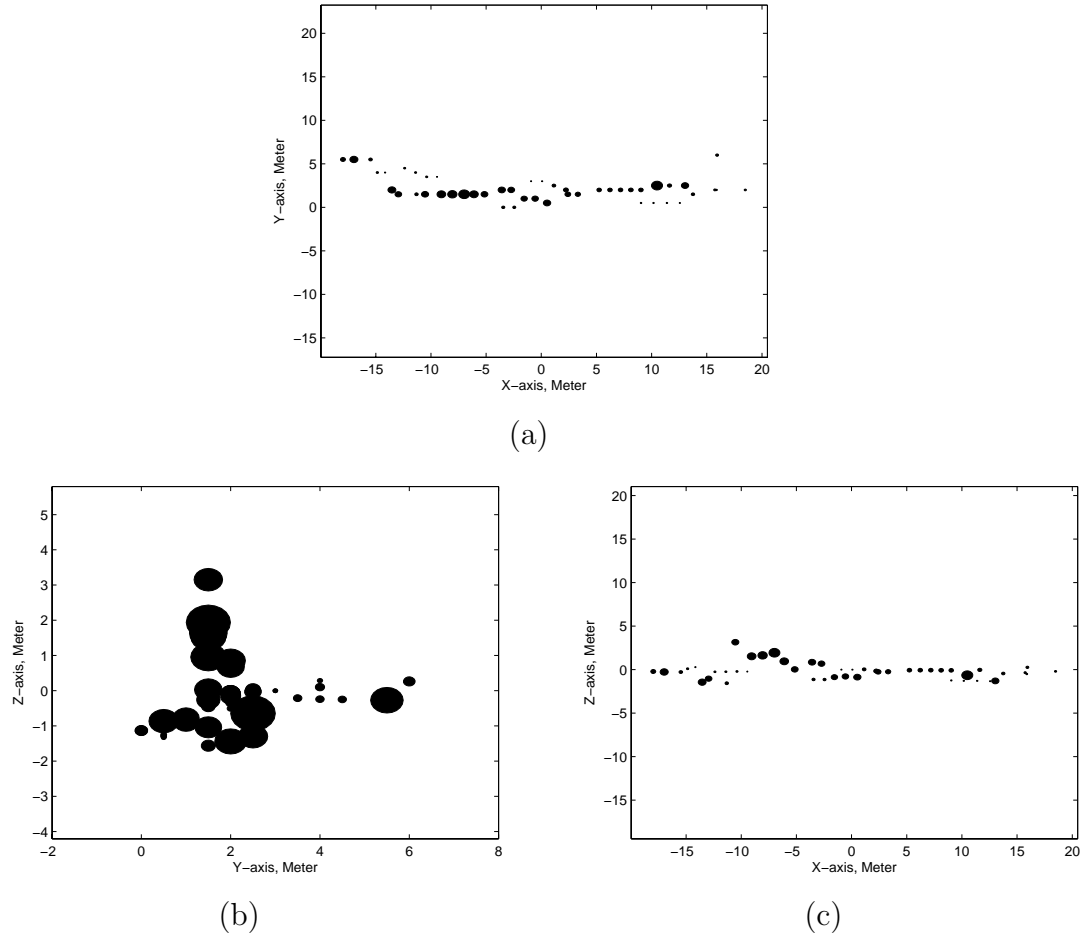


Fig. 2.25: Projected views of the image obtained by the three-antenna method (aeroplane target) (a)XY Plane (b)YZ Plane (c)XZ Plane.

improved images obtained by the array based algorithm and proposed methods.

# Chapter 3

## Sparse Array ISAR Imaging

### 3.1 Introduction

Conventional antenna array inverse synthetic aperture radar three-dimensional imaging system does imaging in two major steps: (1)first getting the ISAR image of the different antennas and (2)using array DOA estimation on every strong scatterer to get the spatial position of that scatterer. The synthetic aperture formed by the target's motion is used to separate the scatterers while the antenna array aperture is only used for position measurement. This is discussed in Section 2.1.

In this chapter, a new imaging method employing a combined two-dimensional sparse-array beamforming technique with ISAR imaging is proposed. It reaps the benefits of the sparse array to achieve a large aperture while using ISAR

imaging to lower the sidelobe of the sparse array beam pattern, thereby achieving a high resolution ISAR image. Also, two target rotational parameters estimation methods are being proposed for maneuvering targets where these parameters are not available.

### 3.1.1 Problems Examined

As discussed in the previous chapter, it is possible to have scatterers that are at different physical positions but having the same range-Doppler value. These scatterers are projected onto the same range-Doppler unit and are termed synthesis scatterers. The existence of synthesis scatterers in ISAR imaging needs to be considered or the imaging may not be accurate and identification would be difficult.

Reported literatures on three-dimensional imaging methods[19][20][21][22][23][72] requires at least two antennas for imaging. The two-antenna based interferometric technique however, can only measure a scatterer's position, but cannot separate synthesis scatterers. As multiple scatterers can be separated by antenna arrays, a three-dimensional imaging configuration using cross azimuth and perpendicular antenna arrays is proposed in the previous chapter and in [75].

A new difficulty of the scatterers' coordinate registration problem arises for the case of the cross antenna arrays configuration. The situation now is that, for the



array signal from one range-Doppler unit, there may be several spatial frequencies corresponding to several scatterers and we have to decide which of the two spatial frequencies in the two arrays corresponding to a particular scatterer. Although the rotational axis and amplitude matching method[75] can solve this problem partially, it is not always effective.

In our work, we extend the use of the cross antenna array configuration of [75] to a two-dimensional sparse array case. The work can also be seen as an extension of method [39] using a temporal camera as discussed in Section 2.1.1. Using our proposed sparse-array method, the scatterers' coordinates registration problem can be resolved completely and the three-dimensional image can be obtained by beamforming in one snap shot. However, in order to obtain fine spatial resolution, a very wide antenna aperture is required, and therefore many antenna elements are required if a two-dimensional full antenna array is used.

The advantage of a sparse array is that although it has a wider aperture, the number of antenna elements can be greatly reduced compared to a full array[76]. It however, has the drawback of high sidelobe levels. Therefore, using the conventional one snap shot spatial signal processing has disadvantages of low SNR and high sidelobe level which degrades the image quality. Fortunately, sparse-array beamforming when combined with ISAR imaging can reduce the sidelobe level

and increase the SNR as to be shown in our work.

Due to the large aperture formed by the sparse array, a long coherent time duration is not needed to separate scatterers. Therefore, during a short time duration, the rotation of the target relative to the antenna array may be approximated as an uniform rotation. Techniques[24][25][26][27][28][29] such as time frequency analysis or super resolution spectrum analysis are not necessary. The rotation vector can then be estimated by combining the two-dimensional sparse-array beamforming and ISAR imaging. After obtaining the rotational parameters, the three-dimensional images at different times can be combined coherently.

This chapter is organized as follows. In Section 3.2, the spatial time signal models of antenna array configurations are derived. The envelope alignment, motion compensation, and imaging algorithm are then discussed in Section 3.3 and 3.4. Simulation results are presented in Section 3.6. In Section 3.7, we conclude our work on sparse-array imaging.

### 3.2 Spatial and Time Domain Signal Model for Three-dimensional Motion

The geometry of three-dimensional imaging based on antenna array is shown in Fig. 3.1.

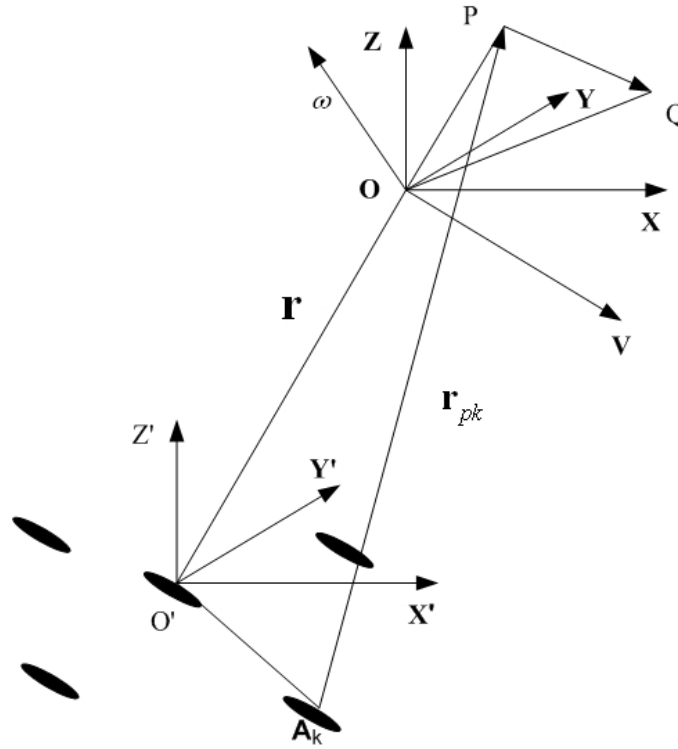


Fig. 3.1: Geometry of the radar and the target.

The origin of the three-dimensional coordinate system  $(X', Y', Z')$  is denoted as  $O'$ , the transmit antenna's position coincides with the origin and the two-dimensional receive antenna array is located near the origin  $O'$ . The position of the receive antenna element  $A_k$  is also denoted as vector  $\mathbf{d}_k = \overrightarrow{O'A_k}$ . A local coordinate system  $(O, X, Y, Z)$  parallel to the radar coordinate system is used to

describe the position of the target. Point  $P$  located in  $(x, y, z)$  is expressed as  $\mathbf{p} = \overrightarrow{OP}$ .

Let the transmitted signal from antenna  $O'$  be  $\tilde{s}(t) = \exp(j2\pi ft)$ . The backscattered signals from scatterer  $P$  received at antennas  $O'$  and  $A_k$  are

$$s_{p0}(t) = \exp\left(j2\pi f\left(t - \frac{2r_{p0}}{c}\right)\right) \quad (3.1)$$

and

$$s_{pk}(t) = \exp\left(j2\pi f\left(t - \frac{r_{p0} + r_{pk}}{c}\right)\right) \quad (3.2)$$

respectively, where  $r_{p0} = |\overrightarrow{O'P}| = |\overrightarrow{O'O} + \overrightarrow{OP}| = |\mathbf{r} + \mathbf{p}|$ ,  $r_{pk} = |\overrightarrow{A_kP}| = |\overrightarrow{A_kO'} + \overrightarrow{O'O} + \overrightarrow{OP}| = |\mathbf{r} + \mathbf{p} - \mathbf{d}_k|$ ,  $c$  is the speed of light and  $f$  is the carrier frequency.

For simplicity, we ignore the effects of path loss on the signal amplitude. Let the signal from receiving antenna 0 be the reference signal, then we have

$$s_{p0}^*(t)s_{pk}(t) = \exp\left(j2\pi \frac{r_{p0} - r_{pk}}{\lambda}\right), \quad (3.3)$$

where  $\lambda$  is the wavelength. The difference between  $r_{p0}$  and  $r_{pk}$  is

$$\begin{aligned}
\Delta r &= r_{p0} - r_{pk} \\
&= |\mathbf{r} + \mathbf{p}| - |\mathbf{r} + \mathbf{p} - \mathbf{d}_k| \\
&= \frac{(\mathbf{r} + \mathbf{p})^T(\mathbf{r} + \mathbf{p}) - (\mathbf{r} + \mathbf{p} - \mathbf{d}_k)^T(\mathbf{r} + \mathbf{p} - \mathbf{d}_k)}{r_{p0} + r_{pk}} \\
&= \frac{2(\mathbf{r} + \mathbf{p})^T \mathbf{d}_k - \mathbf{d}_k^T \mathbf{d}_k}{r_{p0} + r_{pk}}.
\end{aligned} \tag{3.4}$$

The received array signal can then be expressed as

$$\mathbf{s}_p = s_{p0}(t) \times [1, \dots, e^{j2\pi \frac{2(\mathbf{r} + \mathbf{p})^T \mathbf{d}_k - \mathbf{d}_k^T \mathbf{d}_k}{\lambda(r_{p0} + r_{pk})}}, \dots]^T. \tag{3.5}$$

As the position of the antennas are known, the term  $\mathbf{d}_k^T \mathbf{d}_k$  can be canceled by preprocessing. After that, the distance difference from scatterer  $P$  to antenna 0 and to antenna  $k$  is proportional to the projection of the scatterer  $P$  to the vector  $\mathbf{d}_k$ .

Let  $Q$  be another scatterer, the received array signal backscattered from scatterer  $Q$  is

$$\mathbf{s}_q = e^{-j4\pi \frac{r_{q0}(t)}{\lambda}} \times [1, \dots, e^{j2\pi \frac{2(\mathbf{r} + \mathbf{q})^T \mathbf{d}_k - \mathbf{d}_k^T \mathbf{d}_k}{\lambda(r_{q0} + r_{qk})}}, \dots]^T. \tag{3.6}$$

Let  $P$  be the focus point and after compensation using  $\mathbf{s}_p$ ,  $\mathbf{s}_q$  becomes

$$\hat{\mathbf{s}}_q(t) = \mathbf{s}_p^*(t) \odot \mathbf{s}_q(t) = e^{-j4\pi \frac{r_{q0}(t) - r_{p0}(t)}{\lambda}} \times [1, \dots, e^{j2\pi \left( \frac{2(\mathbf{r}+\mathbf{q})^T \mathbf{d}_k - \mathbf{d}_k^T \mathbf{d}_k}{\lambda(r_{q0} + r_{qk})} - \frac{2(\mathbf{r}+\mathbf{p})^T \mathbf{d}_k - \mathbf{d}_k^T \mathbf{d}_k}{\lambda(r_{p0} + r_{pk})} \right)}, \dots]^T, \quad (3.7)$$

where  $\odot$  is the element-wise product. We assume that the translational velocity vector of the target is  $\mathbf{v}$ , while the target rotates around its rotational axis  $\omega = [\omega_x, \omega_y, \omega_z]^T$  ( $|\omega| = 1$ ) with rotation speed  $\Omega$ . Define a skew symmetric matrix

$$\hat{\omega} = \begin{pmatrix} 0 & -\omega_z & \omega_y \\ \omega_z & 0 & \omega_x \\ -\omega_y & \omega_x & 0 \end{pmatrix}, \quad (3.8)$$

then the rotation matrix is denoted as  $R(t) = I + \sin(\Omega t)\hat{\omega} + (1 - \cos(\Omega t))\hat{\omega}^2$  [77].

Denote  $\vec{v} = (\mathbf{v} - \mathbf{n}_0^T \mathbf{v} \mathbf{n}_0) / \tilde{r} - \Omega \hat{\omega} \mathbf{n}_0$  and after simplifying, (3.7) can be expressed as

$$\hat{\mathbf{s}}_q(t) = e^{-j4\pi \frac{r(0) + \vec{v}^T \vec{PQ}}{\lambda}} \times [1, \dots, e^{\frac{j2\pi(\vec{PQ} - \vec{PQ}^T \mathbf{n}_0 \mathbf{n}_0)^T \mathbf{d}_k}{\lambda \tilde{r}}}, \dots], \quad (3.9)$$

where  $\mathbf{n}_0$  is the radar line of sight unit vector and  $\mathbf{r}_0$  is the initial value. For the details of the derivation, please refer to the appendix A. Due to the large aperture formed by the sparse array, a long coherent time duration is not needed to separate scatterers. Therefore, in this chapter, we only consider imaging for case of small angle rotation, such that during the data collection duration, the relative position between different scatterers do not change dramatically, that is

$$\mathbf{r}_q(t) - \mathbf{r}_p(t) \approx \mathbf{r}_q(0) - \mathbf{r}_p(0) = \overrightarrow{PQ}.$$

Generally, fine range resolution can be obtained by transmitting a wideband signal. Let the transmitted wideband linear frequency modulated signal be

$$\tilde{s}(t) = \tilde{\chi}(t) \exp \left\{ j2\pi \left( ft + \frac{\mu}{2} t^2 \right) \right\}, |t| < \frac{T}{2}, \quad (3.10)$$

where  $\mu$  is the chirp rate and  $T$  is the chirp pulse duration.  $\tilde{\chi}(t)$  is the envelope of the transmitted signal satisfying  $\tilde{\chi}(t) = 1$ , for  $|t| < \frac{T}{2}$ , and  $\tilde{\chi}(t) = 0$ , for  $|t| > \frac{T}{2}$ .

The received signal of one antenna is

$$s(t) = \rho \times \tilde{\chi}(t - \tau) \exp \left\{ j2\pi \left[ f(t - \tau) + \frac{\mu}{2} (t - \tau)^2 \right] \right\}. \quad (3.11)$$

After demodulation and match filtering, the received signal can be expressed as [68]

$$\begin{aligned} s(t) &= \rho \times \tilde{\chi}(t - \tau) \exp(-j2\pi f\tau) \\ &\quad \times (T - |t - \tau|) \times \text{sinc}(\mu(T - |t - \tau|)(t - \tau)) \end{aligned} \quad (3.12)$$

$$= \chi(t - \tau) \exp(-j2\pi f\tau), \quad (3.13)$$

where  $\text{sinc}(x) = \frac{\sin(\pi x)}{\pi x}$  and  $\chi(t) = \tilde{\chi}(t)(T - |t|) \times \text{sinc}(\mu(T - |t|)t)$  describes the signal envelope after pulse compression. The wideband array signal from  $Q$  after

pulse compression can be expressed as

$$\mathbf{s}_q(t) = \alpha_q \times e^{-j4\pi r_q(t)/\lambda} \times \begin{bmatrix} \chi(t - \frac{2r_{q,0}(t)}{c}) \times 1 \\ \chi(t - \frac{r_{q,0}(t) + r_{q,1}(t)}{c}) \times e^{j2\pi \frac{2(\mathbf{r} + \mathbf{q})^T \mathbf{d}_k - \mathbf{d}_k^T \mathbf{d}_k}{\lambda(r_{q0} + r_{qk})}} \\ \vdots \\ \chi(t - \frac{r_{q,0}(t) + r_{q,K-1}(t)}{c}) \times e^{j2\pi \frac{2(\mathbf{r} + \mathbf{q})^T \mathbf{d}_k - \mathbf{d}_k^T \mathbf{d}_k}{\lambda(r_{q0} + r_{qk})}} \end{bmatrix} \quad (3.14)$$

### 3.3 Envelope Alignment

In this section, the need to do envelope alignment, as well as the way to do it is discussed. As the delays  $r_{p,k}(t)$  are time varying, the echo's envelope are shifted with time. Motion compensation can only be done after the signals' envelopes are aligned. For the case of multiple antennas ISAR imaging, compared to single antenna ISAR imaging, we need to know whether the different antenna's one-dimensional range profiles are aligned at every time instance. For the broadside case, from (3.4), it can be seen that for our parameters of interest, such as  $\tilde{r} = 10000m$ ,  $|\mathbf{d}_k| = 100m$ , and scatterer  $P$  on the broadside of antenna array satisfies  $(\mathbf{r} + \mathbf{p})^T \mathbf{d}_k \approx 0$ . But more importantly,  $\Delta r = 100 \times 100 / (2 \times 10000) = 0.5m$ . Since  $\Delta r$  is comparable to range resolution, therefore range alignment is needed for the different antennas. If the target is located in the slant-range direction (off broadside), then range envelope alignment between the different antennas is also necessary as  $2(\mathbf{r} + \mathbf{p})^T \mathbf{d}_k / (r_{p0} + r_{pk}) \approx \mathbf{n}_0^T \mathbf{d}_k$ , is usually larger than range resolution.



Another consideration is whether there is a constant shift between the range profiles of the different antennas. If there is a constant shift quantum between adjacent antennas, the envelope shift quantum for antennas  $k$  relative to the first antenna can be easily calculated. The envelope alignment can then be easily done by shifting the envelope according to the relative shift of each adjacent antenna and this will lower computational power requirements. Otherwise, the shift between envelopes has to be calculated by correlation which is computationally more expensive.

After envelope alignment and motion compensation using the methods discussed in Section 2.3.3, the signal of (3.9) can be obtained.

### 3.4 Three-dimensional Imaging Algorithms

In this section, we review and discuss the potential limitations of two three-dimensional imaging methods that are closely related to our proposed work, namely 1) Interferometric imaging using three antenna elements and 2) Imaging based on DOA estimation of cross antenna array. However, the bulk of the discussion would still be on our proposed processing method 3) Imaging based on combination of sparse-array beamforming and ISAR imaging.

### 3.4.1 Interferometric Imaging using Three Antenna Elements

The geometry of the three-antenna imaging system is shown in Fig. 3.2. One antenna which acts as both the transmitting and receiving antenna is located at  $O'$ , the other two receiving antennas  $A$  and  $B$  are located in the  $X$  and  $Y$  axis, and denoted as antenna 1 and antenna 2 respectively. The distance from both  $A$  and  $B$  to  $O'$  is  $d$ .

For simplicity, let the origin of the coordinate system  $(X, Y, Z)$  be the focusing point denoted by  $O$ . The position of scatterer  $Q$  relative to  $O$  along the  $X$  direction can be obtained by comparing the phase of the received signal from antenna 1 and antenna 0. Similarly, the relative position of  $Q$  along  $Y$  direction can also be obtained. Together with the range information obtained by wideband pulse compression, the three-dimensional position of the scatterer  $Q$  can be obtained. The phase of the signal  $Q$  can be obtained by carrying out ISAR imaging on each of the three antennas' received signal. One should be careful to make sure that the phase information is kept unchanged during the ISAR imaging process.

According to (3.9), the phase difference  $\varphi_x$  between antenna 0 and antenna 1

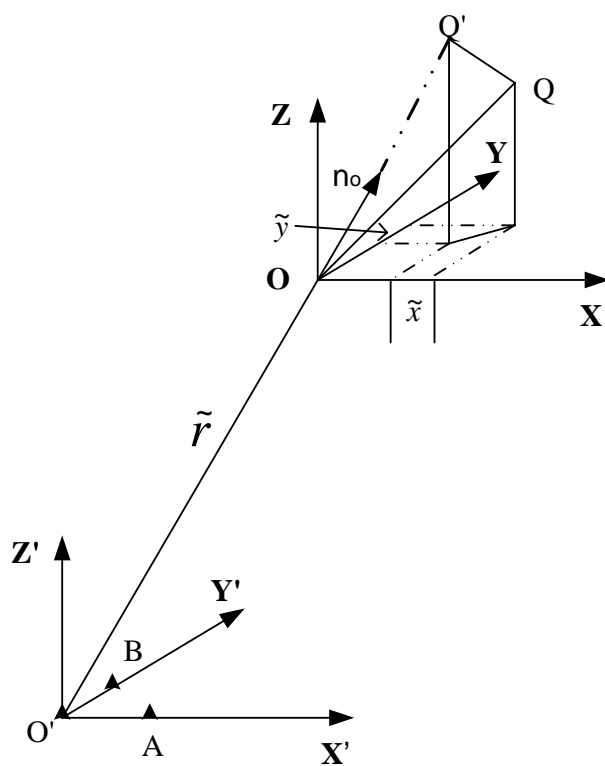


Fig. 3.2: Three-antenna ISAR imaging system.

which can be obtained by ISAR imaging is

$$\varphi_x = \frac{2\pi(\mathbf{q} - \mathbf{q}^T \mathbf{n}_0 \mathbf{n}_0)^T \mathbf{d}}{\lambda \tilde{r}}, \quad (3.15)$$

Similarly, the phase difference  $\varphi_y$  between antenna 0 and antenna 2 can also be obtained. Denote  $\overrightarrow{Q'Q} = \mathbf{q} - \mathbf{q}^T \mathbf{n}_0 \mathbf{n}_0 = \{\tilde{x}, \tilde{y}, \tilde{z}\}$ ,  $r = \mathbf{q}^T \mathbf{n}_0$  and  $\mathbf{q} = \{x, y, z\}$ , then we have

$$\tilde{x} = \varphi_x \frac{\lambda \tilde{r}}{2\pi d} \quad (3.16)$$

$$\tilde{y} = \varphi_y \frac{\lambda \tilde{r}}{2\pi d} \quad (3.17)$$

$$\tilde{x} = x - r n_x \quad (3.18)$$

$$\tilde{y} = y - r n_y \quad (3.19)$$

According to  $\mathbf{q}^T \mathbf{n}_0 = r$ , it is easy to obtain

$$x = \tilde{x} + r n_x \quad (3.20)$$

$$y = \tilde{y} + r n_y \quad (3.21)$$

$$z = \frac{r - x n_x - y n_y}{n_z} \quad (3.22)$$

As the period of phase is of modulo  $2\pi$ , in order to ensure that there exists an

unique relationship between  $\tilde{x}$  and  $\varphi$ , one should ensure that  $|\frac{2\pi\tilde{x}d}{\lambda\tilde{r}}| < \pi$ . Therefore the maximum cross-range unambiguous width is

$$\tilde{x} \in X = [-\frac{\lambda\tilde{r}}{2d}, \frac{\lambda\tilde{r}}{2d}]. \quad (3.23)$$

In order to obtain precise position measurement,  $d$  should be large enough such that the unambiguous width is just sufficient to cover the target, but not the space beyond that. For the case where  $f = 10GHz$ ,  $\tilde{r} = 10km$  and the non-ambiguous width is  $300m$ ,  $d$  should be  $1m$  which is much larger than the half wavelength used in DOA estimation. As two antennas can only measure the position of one scatterer, measurement errors will occur if several scatterers are projected onto the same ISAR image pixel due to the fact that they have the same Doppler frequency. As most targets are non-cooperative complex objects flying in the sky, this situation is likely to occur and is unavoidable.

### 3.4.2 Imaging based on DOA estimation of Cross Antenna Array

Antenna array can separate scatterers in the spatial domain. If the three antennas are replaced by two perpendicular linear arrays forming a cross shape, it becomes the antenna array configuration of the previous chapter. Let the array inter-element distance be  $d$  and the number of antenna elements in each axis be

$K$ . Let  $P$  be the focussing center and using the local coordinate system, the received array signal of  $Q$  in  $X$  axis antenna array after motion compensation, can be expressed as

$$\hat{\mathbf{S}}_{\mathbf{q}} = e^{-j4\pi \frac{r(0) + \bar{\mathbf{v}}^T \mathbf{q}}{\lambda}} \times [1, \dots, e^{j2\pi \frac{\tilde{x}dk}{\lambda \tilde{r}}}, \dots, e^{j2\pi \frac{\tilde{x}d(K-1)}{\lambda \tilde{r}}}] \quad (3.24)$$

The discrete spatial frequency is

$$f_s = \tilde{x}d/(\lambda \tilde{r}). \quad (3.25)$$

Then we have

$$\tilde{x} = f_s \lambda \tilde{r} / d. \quad (3.26)$$

Similarly, we can obtain the expression for  $\tilde{y}$ . The details of obtaining the coordinates  $(x, y, z)$  from  $(\tilde{x}, \tilde{y}, \tilde{z})$  is discussed in the last subsection.

The cross antenna array requires a large number of antennas for fine resolution. As the unambiguous distance is  $\lambda \tilde{r} / d$ , the cross-range resolution is  $\lambda \tilde{r} / (K \times d)$  if conventional Fourier analysis is used. Usually, an array with many antennas are needed to attain fine resolution. For example, we assume that the target is 30m wide and that the required cross-range resolution is 1m. As the focusing center cannot be controlled, the unambiguous width designed should be at least 60m and the number of antennas needed would be 60. This can be expensive to implement

although super-resolution spectrum analysis such as the Relax method[29] can be used to reduce the required number of antennas.

Another issue is the multiple scatterer registration problem. As the cross array is a one-dimensional array in each direction, the scatterer registration problem will occur if there are more than one scatterer. Let  $Q_1, Q_2$  be two scatterers corresponding to one ISAR image pixel, the frequencies obtained by the two antenna array would be  $[f_{x1}, f_{x2}]$  and  $[f_{y1}, f_{y2}]$ . The combination of  $[f_{x1}, f_{x2}]$  and  $[f_{y1}, f_{y2}]$  give rise to four possible scatterers,  $[f_{x1}, f_{y1}], [f_{x2}, f_{y2}], [f_{x1}, f_{y2}]$  and  $[f_{x2}, f_{y1}]$ . Therefore, two scatterers are illusionary scatterers and non-existent. The amplitude and rotational axis matching criterion proposed in [75] also fail to match the two scatterers if the estimated rotational axis is not correct.

### 3.4.3 Imaging based on Combination of Sparse-array Beamforming and ISAR imaging

Let us now discuss our proposed method of 3D imaging using a combination of sparse-array beamforming and ISAR imaging. We begin our discussion by assuming that the rotation vector  $\vec{\nu}$  is known. The method for estimating the rotation vector is discussed in Section 3.5. As  $\vec{\nu}^T \mathbf{n}_0 = 0$ , and from (A.6), the space-time

signal received from any point  $Q$  after motion compensation can be written as,

$$\mathbf{s}_{\mathbf{q}}(t) = e^{-j4\pi \vec{\nu}^T (\mathbf{q} - \mathbf{q}^T \mathbf{n}_0 \mathbf{n}_0) t / \lambda} \times [1, \dots, e^{j2\pi \frac{(\mathbf{q} - \mathbf{q}^T \mathbf{n}_0 \mathbf{n}_0)^T (\mathbf{d}_k - \mathbf{d}_k^T \mathbf{n}_0 \mathbf{n}_0)}{\lambda \tilde{r}}}, \dots]. \quad (3.27)$$

Denoting  $\tilde{\mathbf{q}} = \mathbf{q} - \mathbf{q}^T \mathbf{n}_0 \mathbf{n}_0$  and  $\tilde{\mathbf{d}}_k = \mathbf{d}_k - \mathbf{q}^T \mathbf{n}_0 \mathbf{n}_0$ , (3.27) can be expressed as

$$\mathbf{s}_{\mathbf{q}}(t) = e^{-j4\pi \vec{\nu}^T \tilde{\mathbf{q}} t / \lambda} \times [1, \dots, e^{j2\pi \frac{\tilde{\mathbf{q}}^T \tilde{\mathbf{d}}_k}{\lambda \tilde{r}}}, \dots]. \quad (3.28)$$

The amplitude of scatterer  $Q$  can be obtained by match filtering the received signal(after motion compensation) with  $\mathbf{s}_{\mathbf{q}}(t)$ .

### Space Time Match Filtering Method

We now discuss the performance of the space time match filtering method. Let  $Q_1$  and  $Q_2$  be two scatterers located on a plane perpendicular to  $\mathbf{n}_0$  and denote  $\mathbf{q}_{12} = \mathbf{q}_2 - \mathbf{q}_1 = \tilde{\mathbf{q}}_2 - \tilde{\mathbf{q}}_1$ .

The signals from scatterers  $Q_1$  and  $Q_2$  are then

$$\mathbf{s}_{q1}(t) = e^{-j4\pi \vec{\nu}^T \tilde{\mathbf{q}}_1 t / \lambda} \times \left[ 1 \dots e^{j2\pi \frac{\tilde{\mathbf{q}}_1^T \tilde{\mathbf{d}}_k}{\lambda \tilde{r}}} \dots e^{j2\pi \frac{\tilde{\mathbf{q}}_1^T \tilde{\mathbf{d}}_K}{\lambda \tilde{r}}} \right]^T \quad (3.29)$$

and

$$\mathbf{s}_{q2}(t) = e^{-j4\pi \vec{\nu}^T \tilde{\mathbf{q}}_2 t / \lambda} \times \left[ 1 \dots e^{j2\pi \frac{\tilde{\mathbf{q}}_2^T \tilde{\mathbf{d}}_k}{\lambda \tilde{r}}} \dots e^{j2\pi \frac{\tilde{\mathbf{q}}_2^T \tilde{\mathbf{d}}_K}{\lambda \tilde{r}}} \right]^T. \quad (3.30)$$



Let the coherent integration time be  $T$ , the correlation between  $\mathbf{s}_{q1}(t)$  and  $\mathbf{s}_{q2}(t)$  is

$$r(\mathbf{q}_{12}) = \int_0^T \mathbf{s}_{q1}^*(t) \mathbf{s}_{q2}(t) dt = \int_0^T e^{-j4\pi \vec{\nu}^T \mathbf{q}_{12} t / \lambda} dt \times \sum_{k=0}^{K-1} e^{j2\pi \mathbf{q}_{12}^T \hat{\mathbf{d}}_k / (\lambda \tilde{r})}. \quad (3.31)$$

The first term corresponds to time domain processing, while the second term corresponds to spatial domain processing. Cross-range resolution is determined by  $r(\mathbf{q}_{12})$ .

Let us consider some special cases:

1) When  $\vec{\nu}^T \mathbf{q}_{12} = 0$ , then  $\mathbf{q}_{12}$  is perpendicular to the plane of ISAR. In this case, the Doppler information do not provide any useful information for the separation of  $Q_1$  and  $Q_2$ , and only the antenna array information is useful.

2) The  $K$  virtual antennas  $\tilde{\mathbf{k}}_k$  are arranged as a linear array on the  $x$  axis,  $\mathbf{q}_{12}$  and  $\vec{\nu}$  are along the  $X$  axis. When the target rotates, it appears as if the real antenna has been shifted, thereby creating a virtual antenna. As the target rotates further, a synthetic aperture is formed as shown in Fig. 3.3. Denoting  $x = |\mathbf{q}_{12}|$  and  $v = |\vec{\nu}|$ , then

$$\begin{aligned}
r(x) &= \int_0^T e^{-j4\pi\Omega xt/\lambda} dt \times \sum_{k=0}^{K-1} e^{j2\pi xkd/(\lambda\tilde{r})} \\
&= T e^{-j2\pi vxT/\lambda} \frac{\sin(2\pi vxT/\lambda)}{2\pi vxT/\lambda} \times e^{\frac{j\pi x(K-1)d}{\lambda\tilde{r}}} \times \frac{\sin(\pi xdK/\lambda\tilde{r})}{\sin(\pi xd/\lambda\tilde{r})}
\end{aligned} \tag{3.32}$$

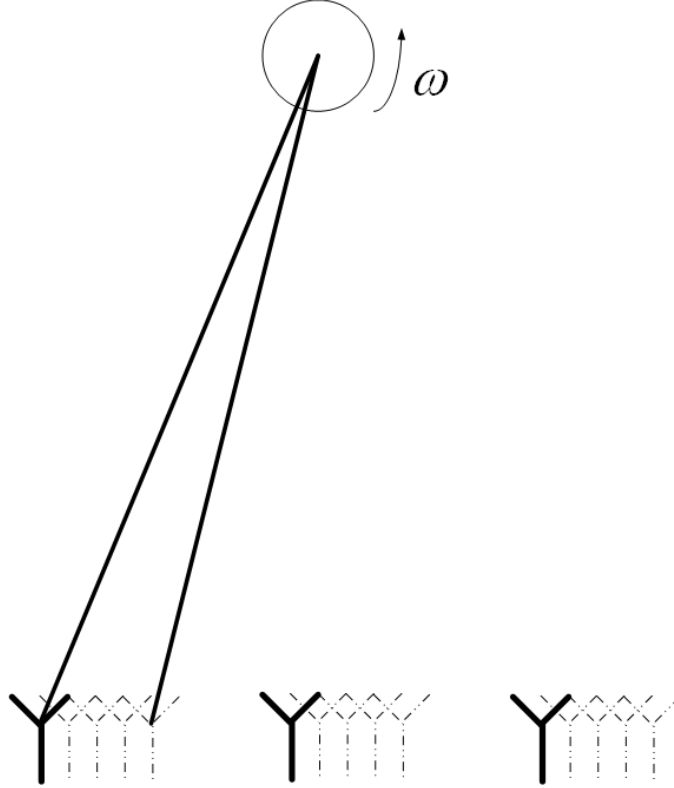


Fig. 3.3: Physical and synthetic antenna aperture.

### Spatial Beam Pattern

The spatial beam pattern of the array  $\frac{\sin(\pi xdK/\lambda\tilde{r})}{\sin(\pi xd/\lambda\tilde{r})}$  shown in Fig. 3.4 is a periodic function of  $x$  with period  $\lambda\tilde{r}/d$ . The first cross zero point of  $\frac{\sin(2\pi vxT/\lambda)}{2\pi vxT/\lambda}$  occurs at  $x = \frac{\lambda}{2vT}$ . If  $\frac{\lambda}{2vT} < \frac{\lambda\tilde{r}}{d}$ , ( $vT > d/2\tilde{r}$ ), the grating lobe of the spatial beam pattern produced by the antenna array can be canceled. A sample of the synthetic beam pattern is shown in Fig. 3.4. For the special case of  $vT = d/2\tilde{r}$ , which refer to

the situation where the synthetic aperture formed by the target motion (equivalent to the target remaining stationary and the physical antenna element moving to the virtual antenna elements position), has moved such that the virtual antenna elements have filled up half the inter-element distance between discrete antenna elements in the array. In this case, we have

$$r(x) = KTe^{j\pi x(K-2)d/\lambda\tilde{r}} \frac{\sin(\pi xKd/\lambda\tilde{r})}{\pi x d/\lambda\tilde{r}} \quad (3.33)$$

This is a *sinc* function. We only fill up half the inter-element distance due to the round trip nature of the radar signals. The real and virtual aperture is shown in Fig. 3.3.

For practical parameters such as  $\lambda = 0.03m$ ,  $r_0 = 30km$ ,  $d = 6m$ ,  $K = 10$ ,  $v = 1$  and  $T = 0.0004s$  the cross-range unambiguous distance is  $150m$  and the cross-range resolution obtained by antenna array beamforming is  $15m$  compared to the cross-range resolution of  $\frac{\lambda}{2\Omega T} = 50m$  obtained by ISAR imaging. The plot of  $r(x)$  is shown in Fig. 3.4.

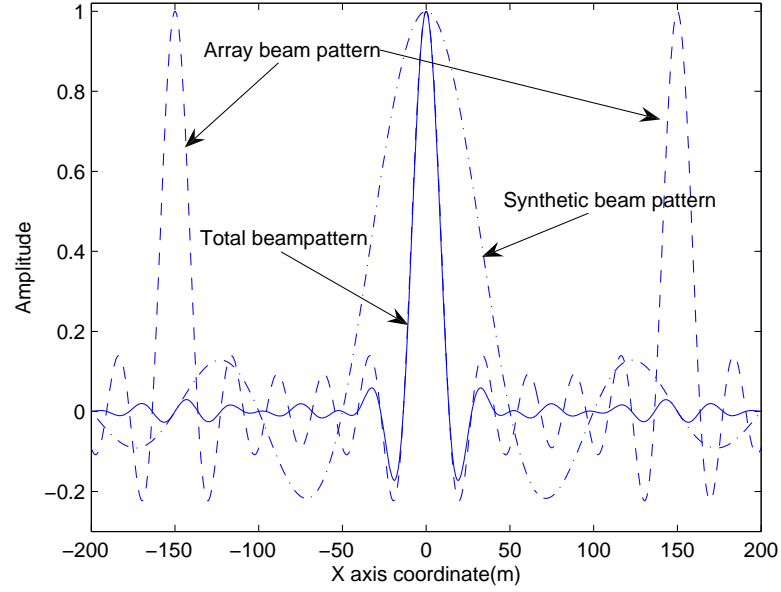


Fig. 3.4: Beam pattern of physical, synthesis and combined array.

### Achievable Cross-range Resolution

Fig. 3.4 shows that the final resolution is determined by the product of the array and synthetic beam pattern. If the main lobe width of the time spectrum is narrower than the non-ambiguous width, the synthetic beampattern has no ambiguity. At the same time, the synthetic beam pattern also has a lower sidelobe compared to the other two. Keeping the antenna elements constant, the cross-range resolution obtained improved with the decrease of the non-ambiguous width, but the mainlobe width of the time spectrum must be smaller than the non-ambiguous width.

It is also possible for the cross-range resolution obtained by ISAR processing

to be better than that obtained by array processing if the synthetic aperture obtained by the the movement of the target is wider than that formed by the antenna array. In such cases, the main benefit of array processing is to increase the SNR. As the resolution achievable by ISAR processing cannot be guaranteed, we can not depend on ISAR resolution in system design. Also, ISAR processing does not have the ability to separate scatterers perpendicular to the ISAR image plane. Therefore the unambiguous width much be wide enough to cover the expected imaging target on system design.

Since the rotational axis can not be controlled, a two-dimensional pseudo uniform antenna array is the best choice. The aperture is determined by the antenna array. In order to ensure fine space resolution, the antenna space aperture should be large, which means that many antenna elements are required and the antenna array hardware will be expensive to implement. Time domain processing only contribute to a higher SNR and lower sidelobe.

### **Use of Sparse Array**

One way to reduce the number of antenna elements is to use a sparse array. A sparse array provides wider aperture while reducing the number of antenna elements[76]. However, it has a drawback of high side lobe level and the sidelobes are difficult to control. An observation is that Doppler processing can reduce the

sidelobe level of the sparse array. Therefore, it can be combined with the sparse array to allow the sparse array to be used. Let  $N$  be the number of sparse antenna array elements, the average sidelobe level is about  $-\sqrt{N}$ dB. According to (3.31), the synthetic beampattern is the product of Doppler spectrum and the spatial spectrum. Fig. 3.5 shows the 256 sparse antenna elements array used in our simulation. It has an aperture equivalent to that of a 1024( $32 \times 32$ ) full array.

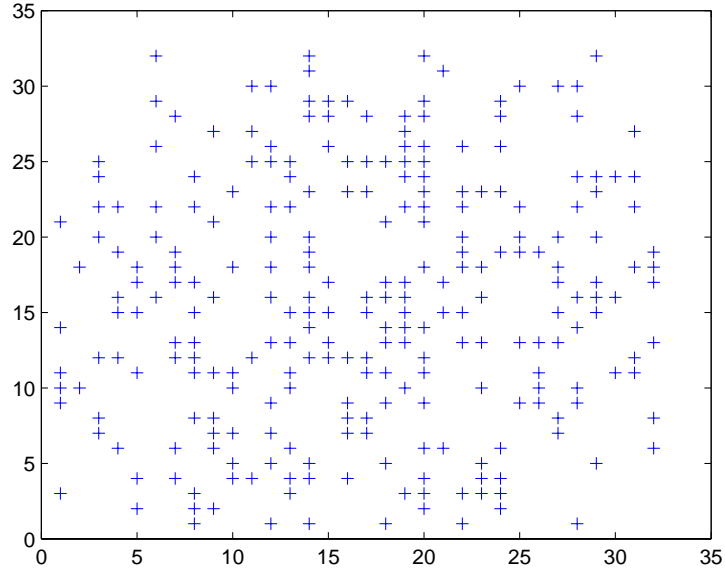


Fig. 3.5: Position of antenna elements.

Fig. 3.6 shows the space beam pattern of the 256 sparse antenna array. The synthetic beam pattern is shown in Fig. 3.7 where the  $\vec{\nu}$  is along the  $Y$  axis. It can be seen that the sidelobe of the beam pattern along the  $X$  direction has been suppressed. The highest sidelobe level of the sparse array in Fig. 3.6 is about

-16dB while the highest sidelobe level when sparse array is combined with ISAR processing in Fig. 3.7 is lower than -20dB.

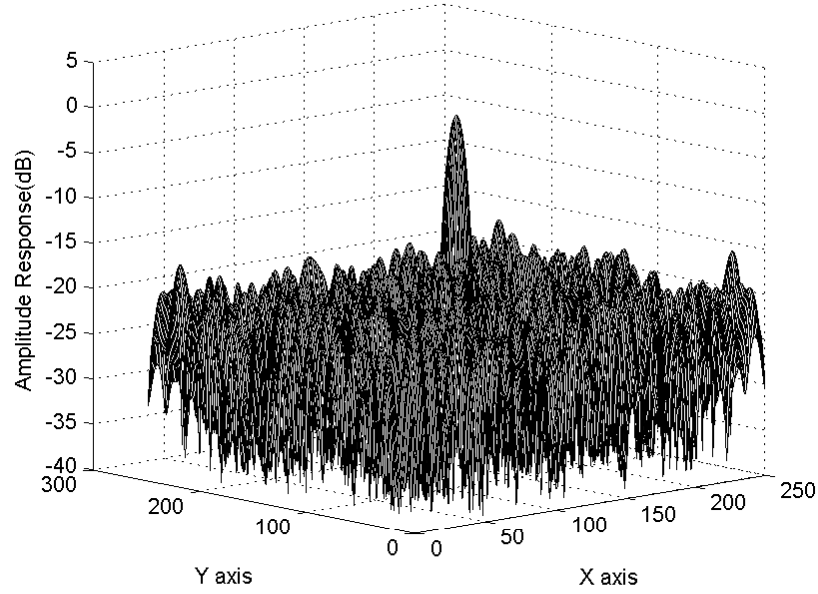


Fig. 3.6: Beam pattern of sparse array.

The above analysis shows that scatterers along the rotational axis direction can only be separated by antenna array processing, while scatterers perpendicular to the rotational axis can be separated by the combined antenna array and ISAR imaging method. The image quality is also different in the different directions.

### 3.5 Estimation of Synthesis Rotation Vector

From our definition, the  $\vec{v}$  is perpendicular to the radar line of sight. Denote the  $(U, V)$  plane to be perpendicular to the radar line of sight, then  $\vec{v}$  is parallel to and

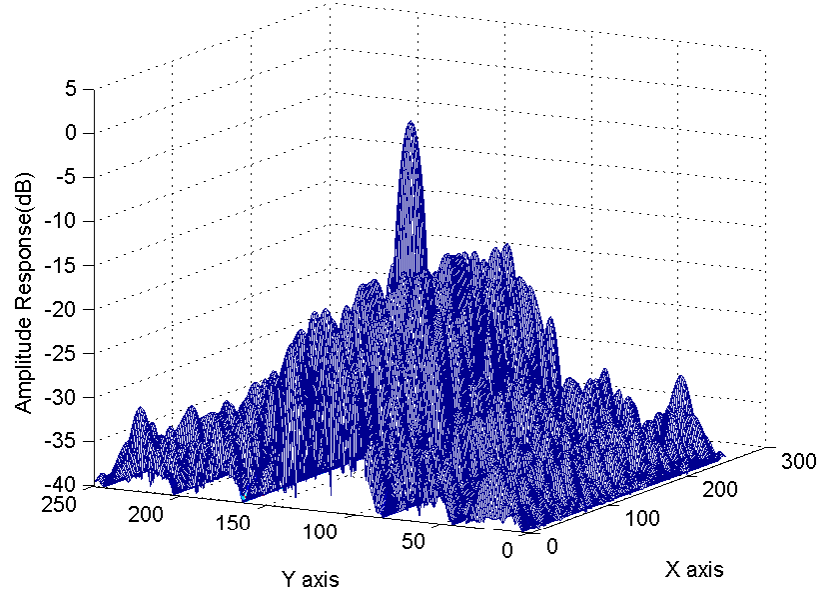


Fig. 3.7: Beam pattern combining sparse array and ISAR processing .

lies on the  $(U, V)$  plane. Let the rotational axis be the  $V'$  axis in a new coordinate system  $(U', V')$ , where the  $U'$  axis coincides with  $\vec{\nu}$ . The rotational angle between the  $U'$  axis and the  $U$  axis is  $\theta$ . For every scatterer, its coordinates in the  $(U, V)$  and  $(U', V')$  coordinate system is denoted as  $(u, v)$  and  $(u', v')$ , respectively. The coordinates transformation from  $(u, v)$  to  $(u', v')$  is given as

$$\begin{pmatrix} u' \\ v' \end{pmatrix} = \begin{pmatrix} \cos \alpha & \sin \alpha \\ -\sin \alpha & \cos \alpha \end{pmatrix} \begin{pmatrix} u \\ v \end{pmatrix} \quad (3.34)$$



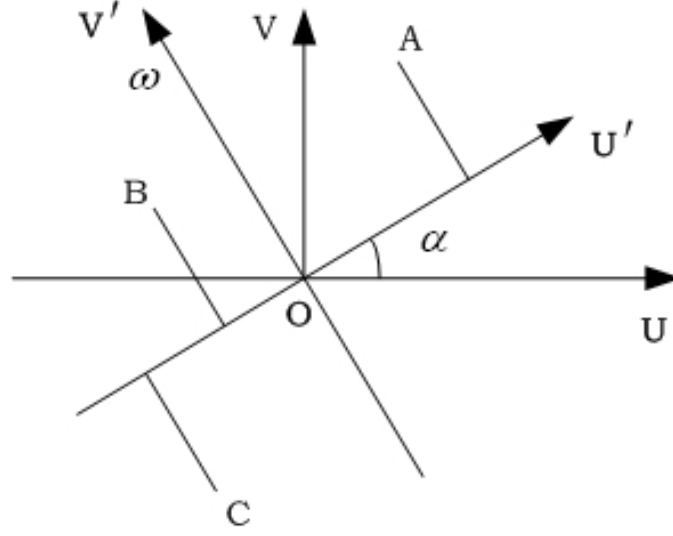


Fig. 3.8: Relation between rotation axis and scatterers' coordinates.

The Doppler frequency of this scatterer is

$$f_d = 2vu'/\lambda = \frac{2\nu}{\lambda}(\cos \alpha, \sin \alpha) \begin{pmatrix} u \\ v \end{pmatrix} \quad (3.35)$$

If there are more scatterers whose Doppler and positions, which can be obtained by ISAR imaging and DOA estimation respectively, are known, then  $v$  and  $\alpha$  can be estimated by using the minimum mean square error estimation.

If the obtained coordinate is based on the  $(X, Y, Z)$  coordinate system, the following estimation method can be used. The doppler frequency of scatterer  $Q_i$  is  $f_d = -2\vec{v}^T \mathbf{q}_i/\lambda$ , where the coordinate of  $Q$  is taken with reference to the  $(X, Y, Z)$  coordinate system, can be obtained from wideband pulse compression and antenna

array DOA estimation. Assuming that  $f_{di}$  and position  $\mathbf{q}_i$  has been estimated and as  $\vec{\nu}$  is perpendicular to  $\mathbf{n}_0$ , an estimation of  $\vec{\nu}$  can be obtained by solving the following constraint optimization problem:

$$\begin{aligned} \min_{\nu} \sum_i (-\frac{2\vec{\nu}^T \mathbf{q}_i}{\lambda} - f_{di}) \\ s.t. \vec{\nu}^T \mathbf{n}_0 = 0 \end{aligned} \quad (3.36)$$

The solution of the above optimization problem is

$$\vec{\nu} = \frac{-\lambda}{2} \mathbf{R}^{-1} (\mathbf{r}_{\mathbf{q}f_d} - \frac{\mathbf{n}_0^T \mathbf{R}^{-1} \mathbf{r}_{\mathbf{q}f_d} \mathbf{n}_0}{\mathbf{n}_0^T \mathbf{R}^{-1} \mathbf{n}_0}) \quad (3.37)$$

where  $R = E\{\mathbf{q}\mathbf{q}^T\}$ ,  $\mathbf{r}_{\mathbf{q}f_d} = E\{\mathbf{q}f_d\}$ .

The cross-range position and the Doppler frequency can be obtained by doing a three-dimensional Fast Fourier Transform (FFT) for signal on several range units with high energy level and then search for the peak value. The position of the peak value gives the cross-range position and Doppler frequency.

### 3.6 Simulation Results

In our simulation, the distance of the target to antennas is 10 km, the transmitted signal's wavelength is  $\lambda = 0.03m$ , the signal bandwidth is  $300MHz$  corresponding to a range resolution of  $0.5m$ . 256 antennas are sparsely arranged on the grids within a two-dimensional square area. The distance between two grids is  $4m$ . The

aperture is  $128 \times 128 m^2$ . The cross-range unambiguous distance is  $25m$ . The target is composed of 11 scatterers with local coordinates (10,4,6; 7,4,3; 4,4,0; 1,4,-3; -2,4,-6; 2,6,0; 2,2,0; -2,6,2; -2,2,2; 0,8,0; 0,0,0) and is placed  $10km$  away along the  $z$  axis.

Distance to target	10 km
Wavelength	0.03 m
Signal Bandwidth	300 MHz
Resultant range resolution	0.5 m
No. of antenna elements	256
Antenna array size	$128 \times 128 m^2$

Table 3.1: Imaging system parameters.

Fig. 3.9 depicts the original three-dimensional image of the target. The volume of the point is used to express the power of the scatterer. The target rotates uniformly around its axis  $[0,1,0]$  with an angular speed of 1 radian per second. The data collection time is 0.0013s, therefore the angle of rotation is  $0.0716^\circ$  which results in a cross-range resolution of  $4m$ . An isolated scatterer has been used to do motion compensation. In the event that there is no isolated scatterer, radial motion compensation and cross-range motion compensation has to be carried out separately as discussed in Section 2.3.3. ISAR image of antenna 0 is shown in Fig. 3.10. The estimated  $\vec{\nu} = [0.9731, 0.0708]$  is quite close to the true  $\vec{\nu} = [1, 0]$ .

The reconstructed three-dimensional image is shown in Fig. 3.11. The volume of the scatterer is used to express its power with a larger volume representing

a larger power. We also see some small dots which arises as we search for the existence of scatterers after doing a three-dimensional FFT. However, the volume of the dots is very small and it means that the power is very small and the scatterers are non-existent. These "artifacts" could be cleaned up on the application of a simple "threshold" algorithm. The threshold can be determined by averaging the power of the  $N^{th}$  scatterer which has the highest power. A higher threshold could mean that more scatterers are discarded and the resolution could be reduced. Conversely, a lower threshold could mean that some noise may be taken as a scatterer, thus providing a wrong ISAR image of the target. Therefore, the choice of the threshold is important as it determines the accuracy of the ISAR image.

After processing, it can be seen that the reconstructed three-dimensional image shown in Fig. 3.11 is similar to that of the original target image shown in Fig. 3.9.

### 3.7 Conclusions

In this chapter, we proposed a three-dimensional imaging method by combining two-dimensional beamforming and ISAR imaging. The two-dimensional sparse array provides the real aperture while ISAR processing lowers the sidelobe. Two target rotational parameter estimation methods have also been presented. Simulation results have successfully demonstrated the effectiveness of our proposed method.

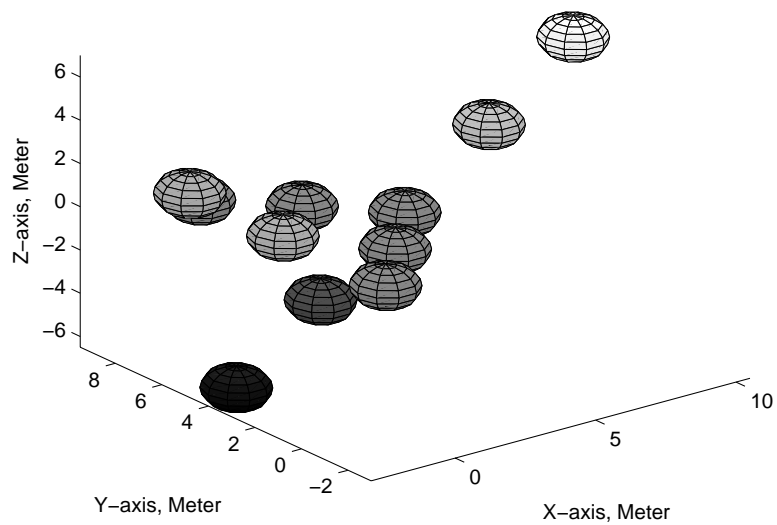


Fig. 3.9: Target's three-dimensional image.

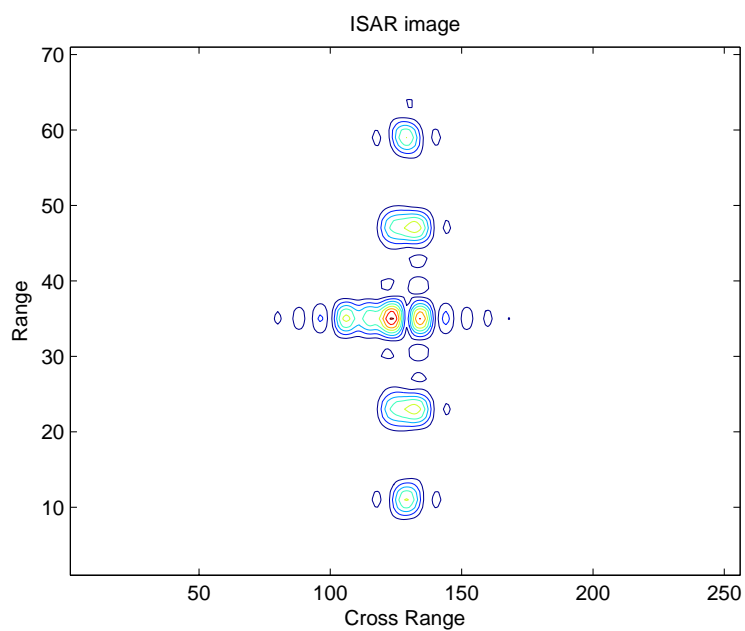


Fig. 3.10: Target's ISAR image.

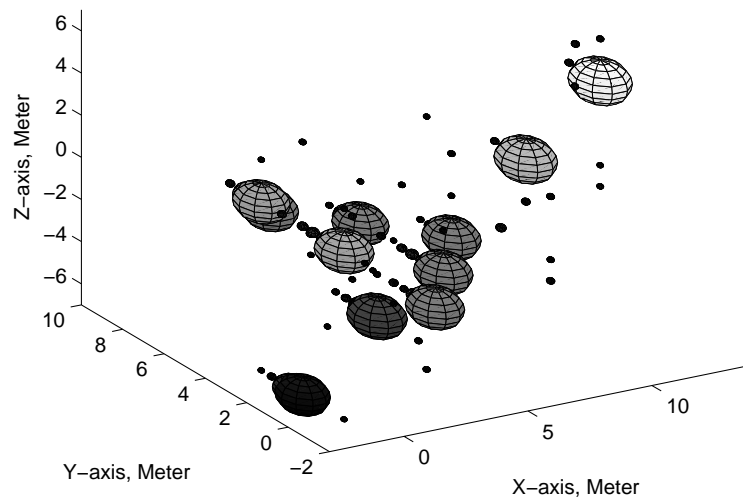


Fig. 3.11: Reconstructed three-dimensional image.

## Chapter 4

# Micro-Doppler extraction using Hough Transform

### 4.1 Introduction

The rotation of structures in a target introduces additional frequency modulations on the returned signals and also generates sidebands about the center Doppler frequency of the target. In other words, the body image will be contaminated due to the interference from the rotating parts. In this chapter, an imaging method for moving targets with rotating parts is presented. The method is simple to implement and is based on the Hough transform(HT), which is widely used in image processing. Using the standard Hough transform(SHT) and an extended Hough Transform(EHT), we put forward a separation method by detecting the

straight lines and the sinusoids on the range profile. A computer simulation has also been provided to illustrate the effectiveness of the proposed method.

#### 4.1.1 Micro-Doppler Phenomena

Mechanical vibrations or rotation of structures in a target introduce additional frequency modulations on returned signals and generate sidebands about the center Doppler frequency of the target's body. This is known as the micro-Doppler phenomenon[30][31][32][33]. The micro-Doppler features can be regarded as a unique signature of an object with movements and provide additional information for the classification, recognition, and identification of the object[34][35].

To make use of these weak features, high-resolution time-frequency techniques with a high dynamic range has been developed to extract these time-varying micro-Doppler signatures[30][34][35][36]. A four parameter adaptive chirplet signal representation method[37] has been used for the separation of rotating parts from the target body in [38]. On the other hand, the existence of the micro-Doppler could also mean that the body image will be contaminated due to the interference from these vibrating or rotating parts, although the relative intensity of the micro-Doppler effect is generally weak [38][78]. However, if these "contaminants" are not weak, then they would pose a serious problem in the actual image formation.



### 4.1.2 Problem Examined

The micro-Doppler information is very useful for radar target identification and classification. In this Chapter, we attempt to find a simple separation method that can be used in inverse synthetic aperture radar(ISAR) imaging of targets with rotating parts, particularly for those whose main body's range profile may be overshadowed by that of the rotating parts, such as the horizontal rotor of a helicopter.

A clear ISAR image of the moving target that comprises of rotating parts cannot be obtained using the conventional range-Doppler imaging principle due to the presence of the micro-Doppler. After the detection of the straight lines and the sinusoids, which correspond to the non-rotating parts and the rotating parts, respectively, the range profile components of the rotating parts can be eliminated.

### 4.1.3 Possible Approach

In this chapter, we utilized the HT in an imaging method for moving target with rotating parts. This method is different from that of [38], in which the signal of the rotating parts is separated from the signal of the body in the parameter space, while here we do the separation on the range profile image. It is known that, after motion compensation, the range profile of a "rigid" scatterer on the range-slow-time plane is a straight line perpendicular to the range axis. Thus, we can find the

line's position at the range axis using the SHT and then conduct cross compression for the detected spectrum, i.e., cross integration in the direction of the slow-time.

On the other hand, the micro-Doppler signal of a rotating scatterer on the target is a sinusoid of a certain phase and amplitude[30][31] in the range-slow-time plane. If its parameters (frequency and amplitude) can be estimated, the position of this scatterer on the range-slow-time plane can be determined and can then be eliminated from the range profile. The methods put forward in [79] and [80] cannot be used here because the methods are developed to produce the borehole wall image in scientific drill or oil exploration and have assumed a fixed sinusoidal period. Therefore, the methods cannot detect multiple sinusoidal frequencies. Here, we put forward an EHT with four parameters in the Hough space for sinusoid detection and estimation and for the subsequent elimination of rotating components from the range profile. The remainder on the range profile is then those of the non-rotating parts, and cross compression can be conducted to obtain the target body's ISAR image.

While this chapter focuses on the application of the classification and imaging of helicopters and hence most of the analysis are directed toward the rotor's micro-Doppler within a certain frequency band, it can easily be extended to deal with other rotating bodies whose frequencies of revolutions fall within different

bands. Similarly, the method presented herewith can easily be extended to the imaging of a maneuvering target by using the range instantaneous Doppler (RID) algorithm[25][81][82] instead of the range Doppler (RD) algorithm in ISAR imaging. In addition, Radon transform can also be utilized to compensate for the radial velocity of the maneuvering target[83]. The Wigner-Hough transform can be used as a substitute for the simple HT to implement line detection.

This chapter is organized in the following manner. Section 4.2 describes the signals of the rotating target using the point-scattering model, including the micro-Doppler effect. In section 4.3, the SHT is reviewed, and an EHT is introduced for the detection of the sinusoids, and then the imaging algorithm is presented. Finally, the performance of the algorithm is analyzed in section 4.4.

## 4.2 Signal Model and Micro-Doppler

In this section, the signal model used in our analysis and the micro-doppler induced by a rotating point of a target is discussed.

### 4.2.1 Signal Model

The point scatterer is usually used in a radar imaging algorithm to model the radar signal scattered by an unknown target. The point-scattering model may simplify the analysis while preserving the micro-Doppler effect[31][38].

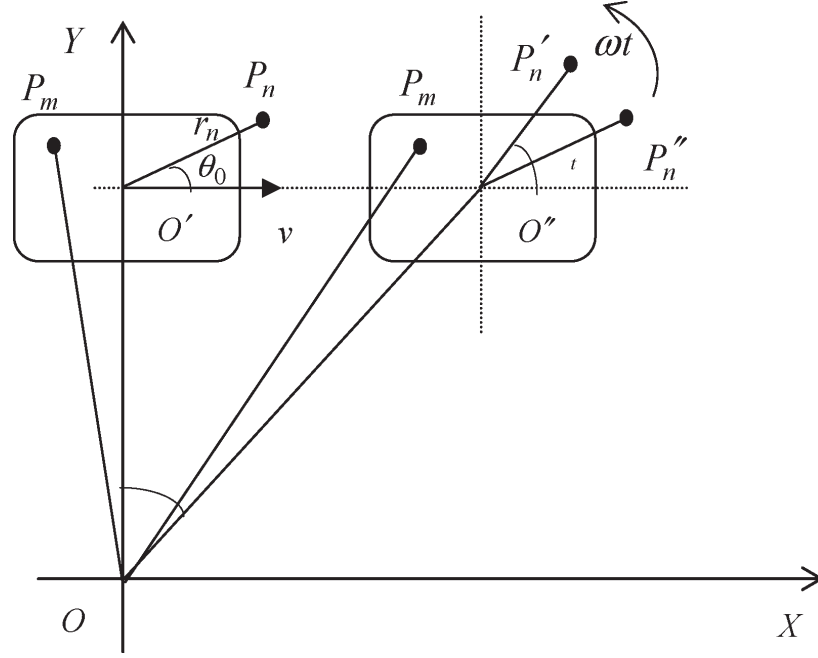


Fig. 4.1: Geometry of a radar and target with a rotating scatterer.

Without loss of generality, we consider the scattering mode in a 2-D plane, as shown in Figure 4.1. The detailed discussion in the 3-D space is covered in [30] and [31]. The radar is stationary and located at the origin  $O$  of the radar coordinate system  $XOY$ . At the initial coherent processing time, the center of the target, i.e.,  $O'$ , is located on the Y-axis. The distance of the target center from the radar is  $R_c$ . Assume that the target moves with a velocity  $v$  along the direction of the X-axis. The moving target is composed of a finite number of non-rotating scatter points  $P_m$  with the position  $(x_m, y_m)$ ,  $m = 1, 2, \dots, M$ , and a finite number of rotating scatter points  $P_n$  with the position  $(x_n, y_n)$ ,  $n = 1, 2, \dots, N$ , respectively.

### 4.2.2 Micro-Doppler effect

Assume that the scatterers  $P_n$  rotate about the target center  $O'$  with a constant rotation rate  $\omega_n$  and different rotation radii  $r_n$ . The Doppler frequency shift induced by the targets motion can be written as

$$f_D = \frac{2}{\lambda} \cdot \frac{x_m v}{R_m(0)} + \frac{2}{\lambda} \cdot r_n \omega \cos(\omega_n \tau + \theta_{n0}) \quad (4.1)$$

where  $\theta_{n0}$  is the initial rotation angle of  $P_n$ ,  $R_m(0)$  denotes the distance of  $P_m$  from the radar at the initial time,  $\lambda$  is wavelength,  $x_m$  is the x-coordinate of scatterer  $m$  and  $r_n$  is the radius of rotation of scatterer  $n$ . The first term in (4.1) is the Doppler shift due to the rigid body translation, and the second term is the micro-Doppler due to the rotation of the scatterers, i.e.,  $f_{microDoppler}$ .

$$f_{microDoppler} = 2\lambda \cdot r_n \omega \cdot \cos(\omega_n \tau + \theta_{n0}) \quad (4.2)$$

In the following, we consider the range profiles of the target with rotating parts, i.e., the Fourier properties of the received signal in the fast-time domain. Let  $p(t)$  be the transmitted radar signal, which is a linear frequency-modulated (LFM) radar signal, i.e., a pulsed chirp signal

$$p(t) = \text{rect}\left(\frac{t}{T_p}\right) \cdot \exp\left(j2\pi\left(f_c t + \frac{1}{2}\mu t^2\right)\right) \quad (4.3)$$

where  $\text{rect}(t) = 1$  for  $-1/2 \leq t \leq 1/2$  and is zero otherwise;  $f_c$  is the carrier

frequency;  $T_p$  is the chirp pulse duration; and  $\mu$  is the chirp rate. After stretch processing[3][5], we obtain the range reconstruction of the target via the fast-time-domain compression, as follows:

$$S_c(f, \tau) = \sum_m \sigma_m T_p \cdot \text{sinc} \left( T_p \left( f + 2 \frac{\mu}{c} (\Delta R_m(\tau)) \right) \right) \cdot \exp \left( j \frac{4\pi}{\lambda} \cdot \Delta R_m(\tau) \right) \\ + \sum_n \sigma_n T_p \cdot \text{sinc} \left( T_p \left( f + 2 \frac{\mu}{c} (\Delta R_n(\tau)) \right) \right) \cdot \exp \left( j \frac{4\pi}{\lambda} \cdot \Delta R_n(\tau) \right) \quad (4.4)$$

where the detailed expressions for  $\Delta R_m(\tau)$  and  $\Delta R_n(\tau)$  are shown in Appendix A. It can be seen that the value of the range profiles will peak at

$$f_m = -\frac{2\mu}{c} \cdot \Delta R_m(\tau) \\ = -\frac{2\mu}{c} \cdot \left( \Delta R_m(0) + x_m \cdot \frac{v\tau}{R_m(0)} \right) \quad (4.5)$$

$$f_n = -\frac{2\mu}{c} \cdot \Delta R_n(\tau) \\ = -\frac{2\mu}{c} \cdot r_n \sin(\omega_n \tau + \theta_{n0}) \quad (4.6)$$

where (4.5) and (4.6) correspond to the non-rotating scattering points and the rotating scattering points, respectively (for details, refer to Appendix A). By

multiplying (4.5) and (4.6) with the coefficient  $-c/(2\mu)$ , the frequencies  $f_m$  and  $f_n$  can be translated to provide the distances of the scatter points  $P_m$  and  $P_n$  from the reference point, respectively. They depict the position of the respective scatter points on the range profiles. Considering the second term inside the bracket of (4.5), it is not difficult to find that the term  $x_m v \tau / R_m(0)$  is very small as compared to the first term,  $\Delta R_m(0)$ . For example, let the pulse repetition interval be  $T = 1/1000s$ ,  $R_m(0) = 10km$ ,  $v = 300m/s$ , and  $x_m = 50m$ ; then, the difference of the distances between the two echoed signals introduced by the term  $x_m v \tau / R_m(0)$  is only 1.5mm, whereas  $\Delta R_m(0)$  is generally in the order of several centimeters. In addition, the term  $v \tau / R_m(0)$  shown in Figure 4.1 actually corresponds to the rotating angle  $\angle O'OO''$  between the two echoed signals[23], which is about  $10^{-5}$  rad with a wavelength of 0.03m and a range resolution of 0.5m. Thus, the said term can be neglected in (4.5), and we have

$$f_m = -\frac{2\mu}{c} \cdot \Delta R_m(\tau) = -\frac{2\mu}{c} \cdot \Delta R_m(0) \quad (4.7)$$

This means that the location of the non-rotating scatter points in the frequency axis is independent of the slow-time. In other words, the distance of the non-rotating scatter points from the reference point is stationary, whereas the distance of the rotating scatter points from the reference point varies with the slow-time. It is easy to find from (4.6) that the distance of the rotating scatter point from

the reference point is a sinusoid function of the slow-time. Thus, the range profile, which is a two-dimensional function of distance and slow-time, will consist of straight lines and sinusoids. It can be seen expressly from a simple example, as shown in Figure 4.2 and 4.3.

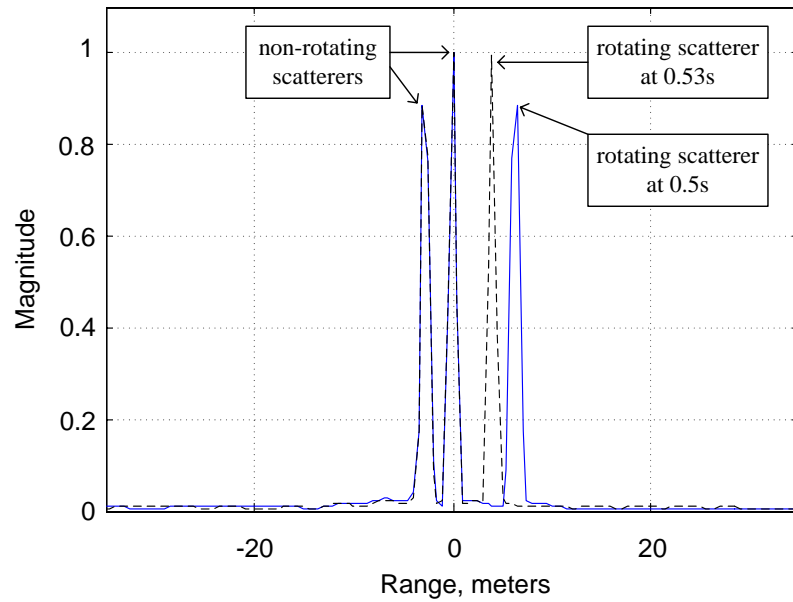


Fig. 4.2: Comparison of the range profile at two different time instance.

Figure 4.2 depicts two range profiles at different slow-time  $\tau$ , where the solid and dotted lines denote the range profiles at the slow-time  $\tau = 0.5s$  and  $\tau = 0.53s$ , respectively. The target comprises of one rotating scatter point and two non-rotating scatter points. One of the non-rotating points can be viewed as the reference point and taken as the rotation center. It can be seen that the positions of the non-rotating points are fixed, and the position of the rotating point shows an obvious change with time. Figure 4.3 is the range profile that is constructed



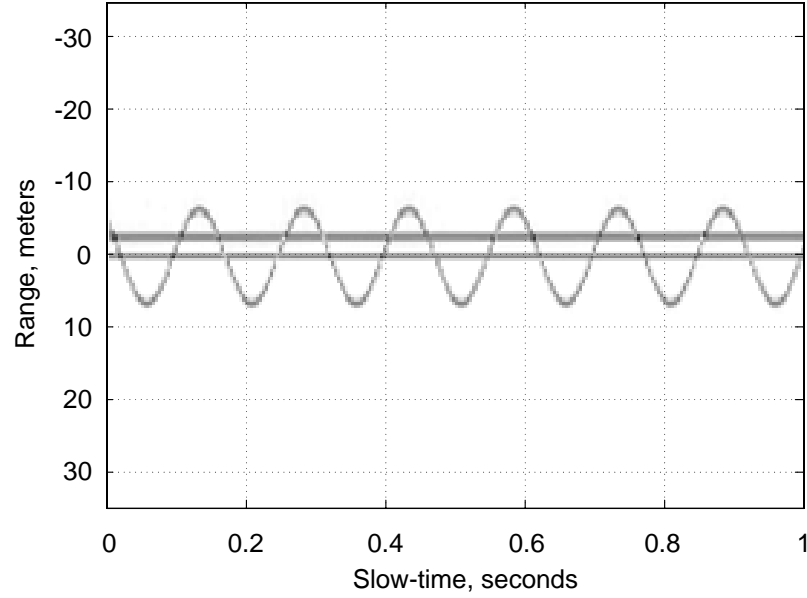


Fig. 4.3: Range profile of a target that comprises of two non-rotating scatter points and a rotating scatter point.

directly from the absolute intensity of the two-dimensional function  $S_c(f, \tau)$ . It can be seen that the traces of the non-rotating scattering points are presented as two straight lines, and the trace of the rotating scatter point is a sinusoid in which the distance of the scatter from the reference point varies along with the line that is produced by the reference point.

### 4.3 HT and Micro-Doppler Extraction Algorithm

In this section, we present an Extended Hough transform and the steps for micro-Doppler extraction.

The HT has been recognized as one of the most popular methods for the detection of line segments. It was first introduced by Hough[84] and was later improved through the adoption of the angle-radius notation to replace the slope-intercept formalism that was initially used. This way, it avoided potential difficulties with singularities for lines parallel to the axes[85]. The advantage of the HT is its stability and robustness when working on images where noise is present. As such, the HT has been used in wide-ranging applications as reported in the literatures[86][87][88][89][90]. In addition to the SHT that is used for detecting straight lines, the generalized HT (GHT) can be used for detecting curves[79][80][85][91][92][93][94]. Specific schemes have also been proposed for the detection of circles, ellipses[95][96], and sinusoids[79][85][93]. These special methods are based on specific features of the patterns and usually have lower computational costs.

### 4.3.1 Standard Hough Transform

The Standard Hough Transform(SHT) maps the straight line on an image space  $(x, y)$  into a point in the HT space via the following equation:

$$\rho = x \cos \theta + y \sin \theta \quad (4.8)$$

All points  $(x_i, y_i)$  on a straight line in the image correspond to a point  $(\rho, \theta)$  in the HT space. Additionally, using trigonometric identities, (4.8) can be rewritten

as

$$\rho = \sqrt{x^2 + y^2} \cdot \sin(\theta + \arctan \frac{y}{x}) \quad (4.9)$$

In general, any point  $(x_i, y_i)$  in the image space can be mapped to a sinusoidal curve in the HT space according to (4.9). For this reason, the HT can also be considered as a point-to-curve transformation. The mapping in (4.9) results in a sinusoid with an amplitude and phase dependent on the  $x - y$  value of the data point that is mapped. The maximum value for  $|\rho|$  is equal to the length of the diagonal across the  $x, y$  data space[97]. Any one of the sinusoidal curves in the Hough parameter space corresponds to the set of all possible lines in the data space through the corresponding data point. If a line of points does exist in the  $x - y$  data space, this line is represented in the Hough parameter space as the point of intersection of all the mapped sinusoids. In addition, the longer the line in the image, the higher the corresponding peak in the Hough parameter space. That is, the dominant features in the Hough parameter space are the most prominent features in the image[91]. For the simulations in this chapter, we use the following equation, similar to (4.8) to detect the straight line:

$$\rho = f \cos \theta + \tau \sin \theta \quad (4.10)$$

### 4.3.2 Extended Hough Transform

The HT has also been developed to extract curves of other shapes, both analytic and non-analytic. However, there exist some limitations and drawbacks in the HT. The drawbacks are that the number of calculating operations and storage requirements are relatively large and that the endpoints and connectivity of the line segments cannot be easily determined or guaranteed. In general, the HT can be used to extract the curves feature with the following basic principle: the parameters  $(a_1, a_2, \dots, a_N)$  are used to represent the curve, and each parameter accumulator simply counts the number of points  $(x_i, y_i)$  fitted into the curve equation

$$f(a_1, a_2, \dots, a_N, x_i, y_i) = 0. \quad (4.11)$$

The accumulator, which contains the local maxima in the Hough space, may correspond to the presence of a curve.

In this chapter, we intend to extract the sinusoids on the range profile image and put forward an Extended Hough Transform(EHT) for this application. According to (4.6), we depict the sinusoid in the frequency-slow-time domain (or the range-slow-time domain) with the following four-parameter transform:

$$f = r \cdot \sin(\omega\tau + \theta_0) + d \quad (4.12)$$

where  $r$  is the maximum amplitude,  $\omega$  is the angle frequency,  $\omega = 2\pi/T_r$ ,  $T_r$  is the period,  $\theta_0$  is the initial phase, and  $d$  can be seen as the baseline and depicts the position of the sinusoid in the frequency axis[79]. (4.12) is readily expanded to define the mapping equation for the plane  $(f, \tau)$  to the four parameter space  $(r, \omega, \theta_0, d)$ . As mentioned in section 4.2, the range profile of a target is composed of straight lines and sinusoids, which denote the non-rotating parts and the rotating parts of the target, respectively. The method presented here is based on the following fact: if these straight lines and sinusoids can be detected with the HT, the return of the non-rotating parts and the rotating parts can be separated in range profile space accordingly. In the next section, we describe our algorithm in detail. For clarity, we present our simulation results step by step according to the algorithm. In our simulations, (4.13) is used to detect the sinusoid on the plane  $(f, \tau)$ :

$$d = f - r \cdot \sin(\omega\tau + \theta_0) \quad (4.13)$$

It should be noted that the displacement of the rotating scatterer must be greater than the range resolution of the radar system so that the micro-motion of the scatterer can be detected.

### 4.3.3 Proposed Extraction Algorithm

The implementation of the extraction of the straight lines and the sinusoids is summarized in the following steps:

**Step 1)** Apply the EHT described in (4.13) to  $I(f, \tau)$ . Find the parameters of the sinusoid and then obtain the respective parameter pairs  $(f_n, \tau_{n_k})$ ,  $(n = 1, 2, \dots, N; k = 1, 2, \dots, n_K)$  using the relationship described in (4.6).

**Step 2)** Extract a new image  $I_1(f, \tau) = |S_1(f, \tau)|$  such that

$$S_1(f, \tau) = \begin{cases} 0, & f_i \in \{f_n | n = 1, 2, \dots, N\} \text{ and } \tau_j \in \{\tau_{n_k} | n_k = 1, 2, \dots, n_K\} \\ S_c(f, \tau), & \text{otherwise} \end{cases} \quad (4.14)$$

**Step 3)** Apply the SHT described in (4.10) to  $I_1(f, \tau)$  to find the locations of the straight lines  $f_m (m = 1, 2, \dots, M)$  at the frequency(or range) axis . This step is used to detect the location of the straight lines, i.e., the location of the non-rotating scatterers in the range axis.

**Step 4)** Extract a new image  $I_2(f, \tau) = |S_2(f, \tau)|$  such that

$$S_2(f, \tau) = \begin{cases} S_1(f_i, \tau), & f_i \in \{f_m | m = 1, 2, \dots, M\} \\ 0, & \text{otherwise} \end{cases} \quad (4.15)$$

Here, the lines from  $I_1(f, \tau)$  is extracted and a new range profile  $I_2(f, \tau)$  is reconstructed.

**Step 5)** Taking Fourier transform with respect to the slowtime  $\tau$  of the newly obtained data matrix  $S_2(f, \tau)$  from Step 4), the ISAR image of the target can be obtained.

### Remediation Processing

Since the sinusoid is removed from the range profile, the intersecting points with the straight-line range profile would also be removed. However, it should be noted that, too many points may be removed if the frequency of the sinusoid is too high. If the rotating frequency of a rotating scatterer is not very high, like e.g. 6Hz, the resultant straight-line range profile will not lose too many points. Therefore, the discontinuities would not have a strong impact on the final ISAR image because the final image is achieved via an integration process along the slow-time.

However, if the scatterer rotates at a higher rotating frequency, such as at a frequency of 20Hz, many points on the straight-line range profile would be wiped out during the removal of the sinusoids. Subsequently, when using the HT to detect the straight line, the corresponding peak of the straight line on the HT space may be lower than the detection threshold. Hence, the algorithm may not

be able to detect the straight line. Losing a straight line will result in the lost of the corresponding scatterer in the final ISAR image. Hence, a remediation processing is necessary for the straight-line range profile that was extracted in Step 2), i.e.,  $I_1(f, \tau)$ . This remediation processing involves replacing  $S_1(f, \tau)$  by  $S'_1(f, \tau)$  as given by:

$$S'_1(f, \tau) = \begin{cases} \frac{\sqrt{\omega_n}}{2\pi} k \cdot S_1(f, \tau), & f \in \{d_n - r_n, d_n + r_n\} \text{ and } n = 1, 2, \dots, N \\ S_1(f, \tau), & \text{otherwise} \end{cases} \quad (4.16)$$

where  $k$  is a scalar coefficient, which is taken to be 0.5-1.5 (obtained via experimental optimization). Its value is chosen to increase monotonically along with  $\omega_n$ . The higher the  $\omega_n$ , the larger the  $k$  would be. This is reasonable because more points will be removed if  $\omega_n$  is higher. After the remediation processing, fine imaging results can usually be achieved.

## 4.4 Simulation Results

The simulation is carried out in the point-scattering mode with five non-rotating scatterers and two rotating scatterers. Both the rotating scatterers rotate around one of the non-rotating scatterers. The rotating rates are 6Hz and 20Hz, while the rotating radii are 6m and 1m respectively. The radar carrier frequency  $f_c = 10\text{GHz}$ , and the bandwidth  $B = 300\text{MHz}$ . Assume an LFM signal with a



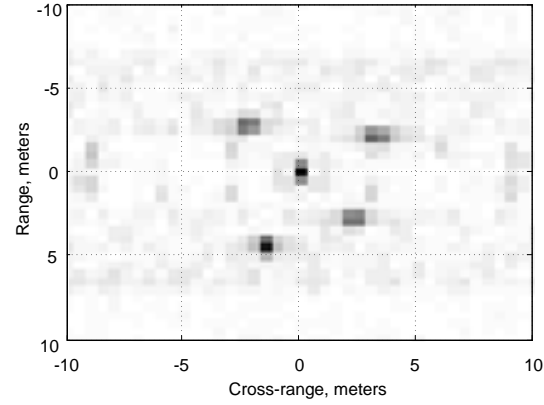
pulsewidth  $T_p = 1\mu s$  and that stretch processing is utilized with a range resolution  $\Delta_R = 0.5m$ . For a pulse repetition frequency (PRF) of 1000Hz and a velocity  $v = 300m/s$  of a moving target, an imaging integration time of 1 s would result in the cross-range resolution of  $\Delta_C = 0.5m$ .

Distance to target	10 km
Wavelength	0.03 m
Signal Bandwidth	300 MHz
Range resolution	0.5 m
Cross-range resolution	0.5 m
Rotating point 1	6 Hz (at 6 m radius)
Rotating point 2	20 Hz (at 1 m radius)

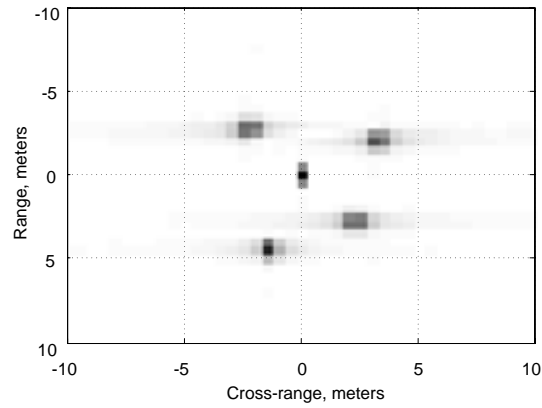
Table 4.1: Simulation parameters.

For simulating a practical situation, we added Gaussian white noise to the echoes, where the signal-to-noise ratio (SNR) is 0 dB. Fig. 4.4(a) is the resulting image of the moving target, and for a comparison, the ISAR image of the target without the rotating scatterer is shown in Fig. 4.4(b).

It can be seen that the image has been contaminated due to the existence of the rotating scatterer. We have assumed a uniform reflectivity for both the non-rotating and rotating targets. While, in general, the reflectivity of the main target body will be much higher than that of the rotating parts, however, there may be situations where the reflectivity of the rotating parts is much higher and thus overwhelms the signal from the main target body. It is noted that the former is a



(a)



(b)

Fig. 4.4: ISAR image for a target consisting of (a) both non-rotating and rotating scatterers, (b) only non-rotating scatterers.

trivial problem, and this chapter is set up to address the latter. A good example is the helicopter blades, which we consider in this chapter.

An  $I \times J$  range profile image  $I(f, \tau) = |S_c(f, \tau)|$  obtained with the simulation data is depicted in Fig. 4.5, where the non-rotating scatterers and the rotating scatterers are clearly depicted as straight lines and sinusoids, respectively.

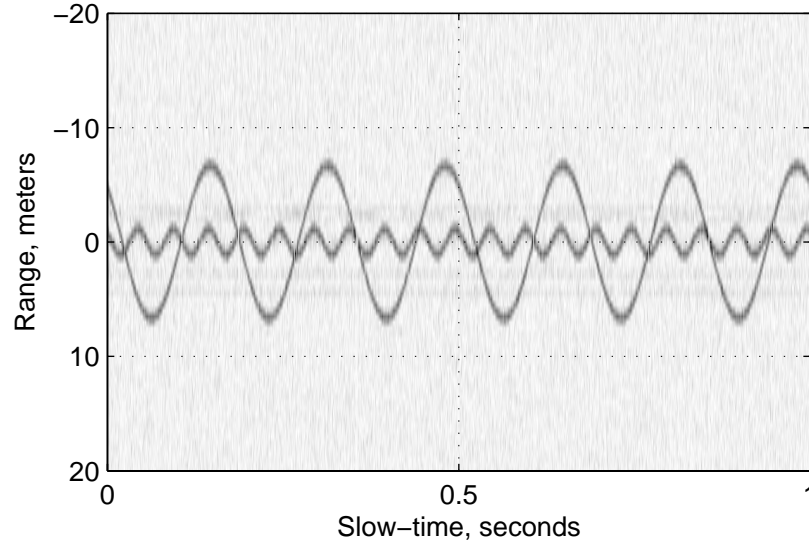


Fig. 4.5: Range profile of a target with both rotating scatterers and non-rotating scatterers(SNR = 0 dB).

The processing steps discussed in the previous section is used. First, we apply the EHT described in (4.13) to  $I(f, \tau)$ . This step is used to detect the parameters of the sinusoids. From the range profile  $I(f, \tau)$ , we obtained seven sinusoids whose parameters are described in Table 4.2. Note that the number of parameter pair is greater than the number of the sinusoids. This is due to the periodic property of the sinusoid. From Table 4.2, it can be seen that the values of the rotating rate  $\omega$  are 125.6637 and 37.6991; that is, the two rotating frequencies of the sinusoids are 20Hz and 6Hz. The corresponding radius of rotation is 1m and 6.5m respectively. The radius of 6.5m differ slightly from the simulated 6m, and this is due to the resolution of 0.5m for the range profile image. Hence the method is accurate in

determining the rotation parameters.

$n$	1	2	3	4	5	6	7
$d$	167	167	167	167	167	167	167
$r$	2	13	2	2	2	2	13
$\omega$	125.6637	37.6991	125.6637	125.6637	125.6637	125.6637	37.6991
$\theta_0$	18	18	24	37	43	62	62

Table 4.2: Sinusoidal Parameters obtained using EHT.

Next, a new image  $I_1(f, \tau) = |S_1(f, \tau)|$  is extracted. The recovered range profile ( $I_1(f, \tau)$ ) is shown in Fig. 4.6.

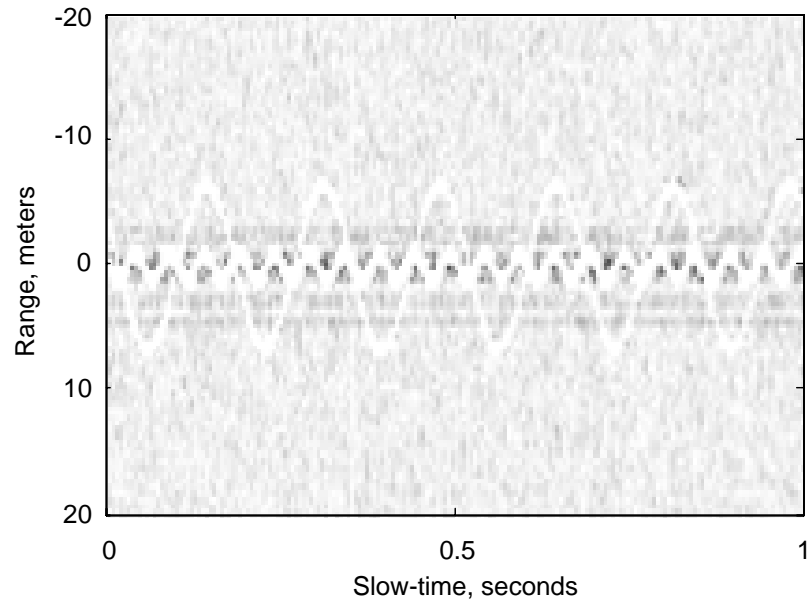


Fig. 4.6: Range profile after the spectrum of the rotating scatterer has been eliminated from the original range profile.

In the new range profile, it can be seen that the sinusoids have been eliminated,

which means that the effects of the rotating scatterers have been removed. However, due to the existence of Gaussian white noise, the straight line in the range profile is not clearly depicted. Moreover, some points in the straight line have also been eliminated along with the removal of the sinusoids. Hence, the scatterers, which correspond to the straight lines, cannot be integrated via image processing due to the missing information. The remediation process discussed in section 4.3.3 must be done to recover these points. The imaging result without remediation processing is shown in Fig. 4.7.

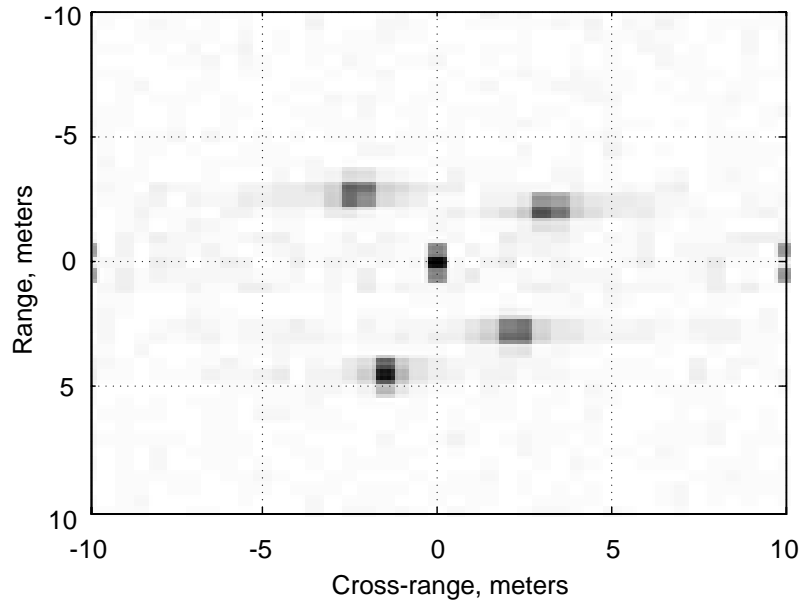


Fig. 4.7: ISAR imaging result after the spectrum of the rotating scatterer has been eliminated.

Applying Step 3), we use the SHT described in (4.10) to  $I_1(f, \tau)$  to detect the

locations of the straight lines, i.e. the location of the non-rotating scatterers in the range axis. In the simulation, taking the threshold as 0.7, we obtained eight parameter pairs, as shown in Table 4.3. (Note that we selected the position  $(160, 1)$  of matrix  $I_1(f, \tau)$  as the origin point in the simulation.) Although we should only have 5 lines, we get eight parameters as one line in  $I_1(f, \tau)$  may be spread over several  $f$ . From these parameters, the locations of the straight lines in the range-slow-time domain  $f_m$  can be determined via (4.10) using the locations of the peaks  $(\rho_m, \theta_m)$ .

$m$	1	2	3	4	5	6	7	8
$\rho$	1	2	3	5	7	12	13	16
$\theta$	0	0	0	0	0	0	0	0

Table 4.3: Straight Line Parameters obtained using SHT.

Applying Step 4), we extract the straight lines from  $I_1(f, \tau)$  and reconstructed a new range profile  $I_2(f, \tau)$ , as shown in Fig. 4.8. Here, it can be seen that the effect of the Gaussian white noise has also been removed.

Finally, by taking Fourier transform with respect to the slow-time  $\tau$  of the newly obtained data matrix  $S_2(f, \tau)$  from Step 4), the ISAR image of the target can be obtained. The final ISAR image is shown in Fig. 4.9.

It is noted that Fig. 4.9 is very close to the ISAR image without the rotating

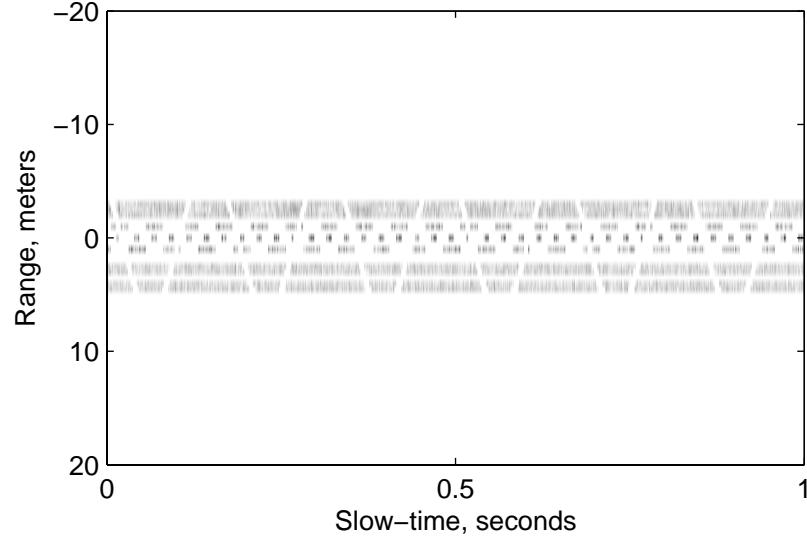


Fig. 4.8: Range profile after the spectrum of the rotating scatterer has been eliminated.

part, as shown in Fig. 4.4(b). In addition, we have obtained some basic information on the rotating parts from Step 1). Although it may not be possible to reconstruct a focused image of the rotating part if the PRF of the radar is too low, as mentioned in [38], we can still identify the rotating center and the lengths of the rotating radii (in this case, the length of the helicopter blades), as well as the rotation rates from Table 4.2, where  $d = 167$  indicates that the rotating center is located in the  $167^{th}$  range cell. The two rotating frequencies of the sinusoids, i.e., 20Hz and 6Hz, mean that the rotating rates of the two rotating scatterers are 20Hz and 6Hz, respectively; while the rotating radius of the rotating scatterer can be calculated by the following formula:

$$r_n = r \cdot \Delta_R \quad (4.17)$$

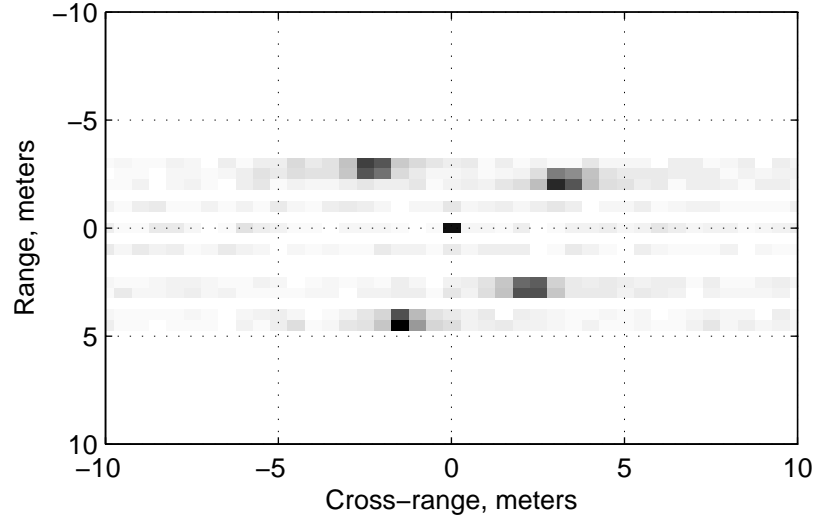


Fig. 4.9: Final ISAR imaging result after the spectrum of the rotating scatterer has been eliminated.

By doing a simple calculation, the radii of the rotating scatterers are obtained.

The radii are  $r_1 = 1m$  and  $r_2 = 6.5m$ , which are close to the true values. All these information are very useful for target identification application.

## 4.5 Comments and Discussions

In this section, we discuss the performance of the proposed algorithm. The micro-Doppler separation method presented in this chapter is based on the HT to detect the return of the non-rotating parts and the rotating parts. Its performance is thus affected by the limitations of the SHT and the EHT put forward in this chapter.

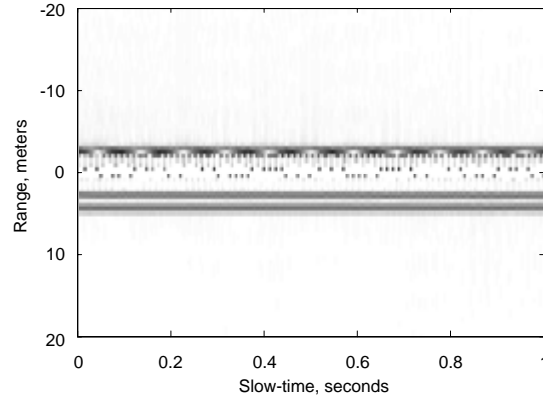
We know that by using the HT for detecting patterns, the computer's storage



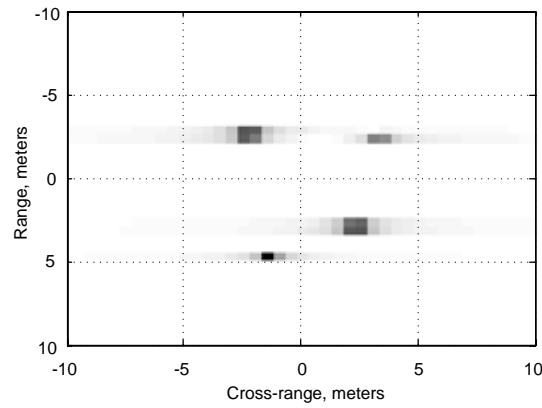
and the computational time increases exponentially with the number of dimensions in the parameter space[92][95]. As the EHT presented here is a four-parameter mapping, its computation cost and the requirement for storage are much higher than those of a general SHT. In our simulation, the computation time for obtaining the parameter set  $(r, f_r, \theta_0, d)$  was approximately 48 minutes on a personal computer with an Intel Pentium IV (2.8 GHz) processor. This disadvantage has prevented it from being used in real-time applications, and thus, more efforts should be done to speed up the computation of the algorithm by using parallel processing, for example.

The remediation processing method presented in section 4.3.3 will also not work properly if the rotating frequency is too high. Simulations have shown that if a large number of points on the straight line (e.g., 90%) have been removed (because of the removal of the sinusoids), then the image of the scatterer, which corresponds to the straight line, cannot be obtained.

Fig. 4.10 presents a worst-case example, where we have a single scatterer rotating at a frequency of 160Hz (9600r/min) at a distance (radius) of 1m from the center. It is noted that too many points on the straight line (corresponding to a scatterer located at the rotating center) are removed when we extract the sinusoid. As a result, the corresponding scatterer in the ISAR image is lost. However, in



(a)



(b)

Fig. 4.10: Processed result of a rotating scatterer with a rotating frequency of 160Hz and radius of 1m (a)Range profile and (b)ISAR image.

a practical situation, the rotating frequency of the main rotor of a helicopter is usually less than 10Hz (examples are 394, 350, and 406r/min or 6.6, 5.8 and 6.8Hz, respectively, for the AS350, AS365, and EC120 of the Eurocopter Company).

To illustrate the effectiveness of the remediation processing, we run a simulation with a scatterer rotating at a frequency of 50Hz at a radius of 1m (without

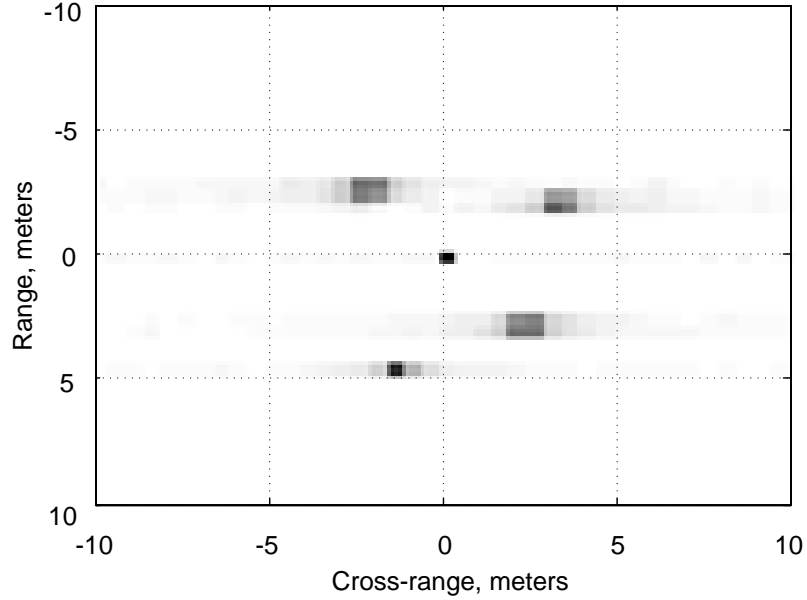


Fig. 4.11: Imaging result of a rotating scatterer with a rotating frequency of 50Hz and a radius of 1m after remediation processing.

noise). Other simulation parameters remained unchanged. As shown in Fig. 4.11, the obtained imaging result is reasonably good.

While the rotating frequency of the tail rotor is much higher at around 2000r/min (approximately 33Hz), it is still within the capability of this algorithm as it has an upper limit of approximately 100Hz. A point to note is that the current algorithm is developed with the aim to solve a certain class of problem, i.e., the imaging of a moving target with large rotating parts (e.g., blades) but at a moderately slow (below 100Hz or 600r/min) frequency. There are, of course, moving targets whose rotating parts rotate at small radii, at high frequencies (hundreds or thousands

of hertz), and in a non-uniform manner. However, the current algorithm is not poised to be an all rounded solution, and we will not discuss these situations in this chapter.

The main advantages of the HT are its robustness to noise and discontinuities in the pattern to be detected[79][85][93]. An extraction method of a three-parameter sinusoid was presented in [79], which described a practical implementation of a computationally efficient and robust method for characterizing the sinusoid curves with considerable noise and clutter. As our current four-parameter EHT is only a simple variation of the SHT, the noise and clutter performance would not be significantly different from that of the SHT. In fact, it should be better due to its additional(fourth) parameter space. The simulation results that were presented in the preceding section also validated the method's robustness to noise.

In the case of imaging a ground moving target with a strong clutter background, the SNR is much lower than that of the moving targets in the air. Therefore, we must suppress the strong ground clutter before the return signals of the target can be detected. The method for removing ground clutter while at the same time preserving the micro-Doppler information will be a subject of further research.

## 4.6 Conclusions

The micro-Doppler information is very useful for radar target identification and classification. It arises from the vibrations and rotations of the scatterer. A clear ISAR image of the moving target that comprises of rotating parts cannot be obtained using the conventional range-Doppler imaging principle due to the presence of the micro-Doppler. In this chapter, the HT has been used to extract the features from the range profile of the target return based on the different representation formats of the rotating parts and the non-rotating parts on the range profile image. After the detection of the straight lines and the sinusoids, which correspond to the non-rotating parts and the rotating parts respectively, the components of the rotating parts can be eliminated. Thus, the focused ISAR image can be obtained, together with the information of the extracted rotating parts. The simulation results presented illustrate the effectiveness of the proposed method.

# Chapter 5

## Micro-Doppler removal by Range Grouping

### 5.1 Introduction

In ISAR imaging, most works have assumed the target to be a rigid body, a body without any rotating, vibrating or moving parts. However, most targets in real life are not. Mechanical vibration, movement or rotation of structures in a target, such as the rotor of a helicopter or the turret of a tank target, introduces additional frequency modulation on returned signals and generates side-bands about the center Doppler frequency of the target's body. This is known as the micro-Doppler phenomenon[30][31][32][33].

Although micro-Doppler features can be regarded as an unique signature of an object with movements and provide additional information for classification, recognition and identification of the object, the existence of the micro-Doppler could mean that the body image will be contaminated due to the interference from these vibrating, moving or rotating parts.

There are several methods such as the high-resolution time-frequency analysis[30] and the four-parameter adaptive Chirplet signal representation method[38], that have been used for the separation of rotating parts from the target body. The methods are based on separation at the signal level. On the other hand, our proposed method is based on the separation of the rotating or moving parts from the target body on the Range Profile Image. This is possible as we know that, after the motion compensation, the range profile of the body is a straight line along with the slow-time. Thus, the straight line can be detected and separated from the varying curve which represents the rotating or moving body parts.

Separation on the Range Profile level has also been carried out to separate high frequency rotating parts such as the horizontal rotor of a helicopter based on the Hough Transform(HT)[84] as described in the previous chapter. However, the rotation of a helicopter rotor is usually unilaterally in a single direction. There are other complex micro movements that one may wish to detect. For example,

the movement of the turret and gun of a tank would not be in a regular circular motion like in the case of the rotor of a helicopter. The turret may be moving in a clockwise or anti-clockwise movement, and the gun may be moving vertically up or down according to operational needs. Thus the Hough Transform may not be suitable to detect this movement on the Range Profile image as it would not be a regular sinusoid.

In this chapter, we attempt to find a simple separation method which can be used in ISAR imaging for the separation of the moving parts from the rigid body. This method is based on range grouping and is suitable for both targets with regular rotating body parts and other moving parts. The method is carried out on the Range Profile Image, different from other methods that do the separation at the signal level.

## 5.2 Simulation Model

The point scattering model is used in radar imaging to model the radar signal scattered by an unknown target. It can simplify the analysis while preserving the micro-Doppler effect[31][38]. Consider the scattering model in a 2-D plane as shown in Fig. 5.1.

The radar is stationary and located at the origin  $O$  of the radar coordinate



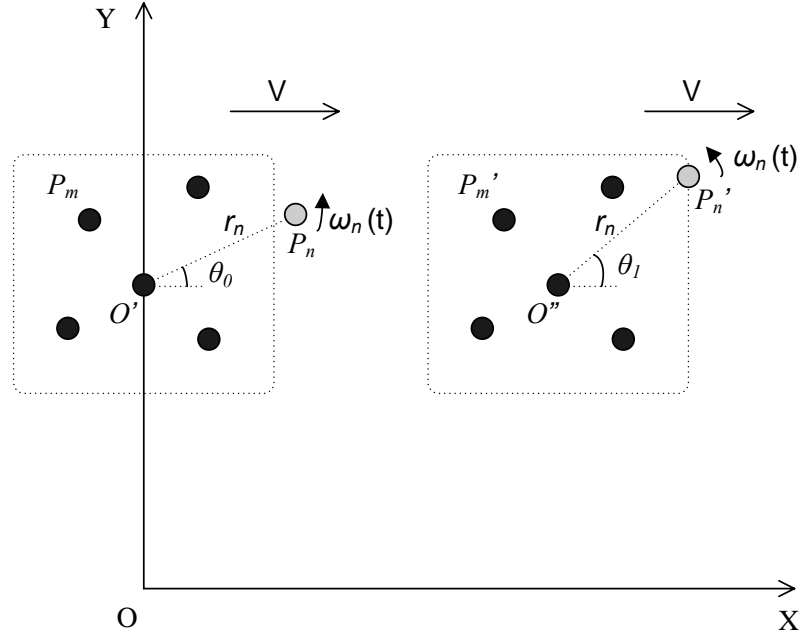


Fig. 5.1: Geometry of a target with a rotating scatterer

system  $XOY$ . The moving target is composed of a finite number of non-rotating scatter points  $P_m$  with the position  $(x_m, y_m)$  that makes up the rigid body, and a finite number of rotating scatter points  $P_n$  with the position  $(x_n, y_n)$ , respectively. In our model shown in Fig. 5.1, there are 5 non-rotating points and a rotating point.

At the initial coherent processing time, the center of the target,  $O'$ , is located at the Y-axis. Assume that the target moves in the X-axis direction with velocity  $V$ . After time  $t$ , the center of the target has moved by a distance of  $Vt$  to the new position  $O''$ . The points  $P_m$  simply undergo a translational motion in the X-axis direction, simulating rigid body motion.

The scatterers  $P_n$  rotate about the target center  $O'$  with a rotation rate  $\omega_n(t)$  and a rotation radii  $r_n$ . At the initial time, the angle the rotating point makes with  $O'$  is  $\theta_0$ . After time  $t$ , the rotating point has rotated by  $\int \omega_n(t)dt$  and the new angle it makes with  $O''$  is now  $\theta_1(t)$ .

In our simulation, a wideband signal is transmitted. Let the transmitted wideband linear frequency modulated signal be

$$s(t) = \chi(t) \exp\{j2\pi(ft + \frac{\mu}{2}t^2)\} \text{ for } |t| < \frac{T}{2} \quad (5.1)$$

where  $f$  is the carrier frequency,  $\mu$  is the chirp rate and  $T$  is the chirp pulse duration.  $\chi(t)$  is the envelope of the transmitted signal satisfying  $\chi(t) = 1$ , for  $|t| < \frac{T}{2}$ , and  $\chi(t) = 0$ , for  $|t| > \frac{T}{2}$ . The received signal is

$$r(t) = \rho \times \chi(t - \tau) \exp\{j2\pi[f(t - \tau) + \frac{\mu}{2}(t - \tau)^2]\} \quad (5.2)$$

After demodulation and match filtering, the received signal can be expressed as

$$\tilde{r}(t) = \rho \times \chi(t - \tau) \exp(-j2\pi f) \times \text{sinc}(\mu T(t - \tau)) \quad (5.3)$$

The range compressed signal from the different slow-time  $\tilde{r}(t)$  will then form

the range profile image. For simplicity sake, we assume that a range profile image has already been obtained as this has been discussed in the previous chapter.

In the first case where we are simulating the micro-Doppler of a helicopter, the rotating scatterer is used to simulate the rotor of a helicopter. The rotating scatterer rotates at a constant rotation rate  $\omega_n$ . The micro-Doppler would appear as a sinusoid in the range profile image. In the second case where we are simulating the micro-Doppler of the gun on a tank target due to a moving tank turret, the rotation would be at a varying rotation rate  $\omega_n(t)$ . The rotation speed may be varying or there may not be any rotation at times. The micro-Doppler in this case would not appear with a specific pattern in the range profile image.

Although the reflectivity of the rotating parts is usually lower than that of the non-rotating parts, there are situations where the reflectivity of the rotating parts may be higher. In our work, we have simulated the reflectivity of the rotation parts to be higher to determine its effect on the ISAR image.

### 5.3 Micro-Doppler Separation Steps

For simplicity sake, we assume that a  $I \times J$  range profile image  $RP(r, \tau)$  has been obtained where each column is the range profile at the slow-time  $\tau$ .  $RP(:, \tau) =$

$|S_{c,\tau}(t)|$  where  $S_{c,\tau}(t)$  is the range compressed signal at slow-time  $\tau$ . The implementation for the extraction of the sinusoids or curves from the range profile image is as follows:

**Step (a) :** Apply thresholding or methods such as Scale Invariant Feature Transform (SIFT)[98] to the range profile image to detect the presence of all points on the range profile image and record their locations at  $R_p(p = 1, 2, \dots, M + N)$  on the range-axis and  $\tau_p(p = 1, 2, \dots, M + N)$  on the slow-time axis, where  $M$  and  $N$  are the number of non-rotating and rotating points respectively.

**Step (b) :** Group the points into arrays according to different range  $R_r(r = 1, 2, \dots, K)$ , where  $R_K$  is the maximum range of the detected points.

**Step (c) :** Count the number of elements in each array  $R_r(r = 1, 2, \dots, K)$ .

**Step (d) :** If the number of elements in each array  $R_r(r = 1, 2, \dots, K)$  exceeds a certain predefined threshold number of elements,  $R_r$  is identified as a range where a straight line exists. The range is noted as  $R_{rs}(rs = 1, 2, \dots, KS)$ , where  $KS$  is the number of straight lines. Any point with range  $R_{rs}$  is a point on the straight line.

**Step (e) :** Points with range  $R_p \neq R_{rs}$  are points belonging to the rotating or moving parts.

**Step (f) :** Remove the points of the rotating, vibrating or moving parts from the range profile image by setting  $RP(R_p \neq R_{rs}, \tau_p) = 0$ .

## 5.4 Simulation Results

Simulation was carried out on two types of target: A) A target consisting of rigid body points and a rotating scatter point simulating the rotor of a helicopter rotating at high frequency; B) A target consisting of rigid body points and an irregular moving point, simulating the movement of the turret of a tank.

An advantage of the proposed method is its added ability to remove the micro-Doppler of rigid bodies with irregularly moving or vibrating body parts. The method in [99] is more suitable for rigid target bodies with unilaterally rotating body parts. Fig. 5.2 shows the simulated rigid body target without any rotating part. This is how the processed ISAR image after removing the micro-Doppler should look like.

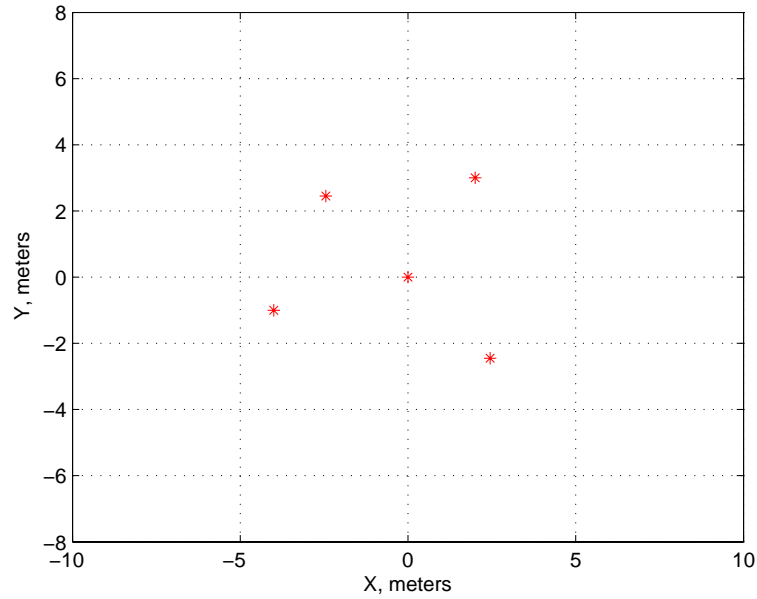


Fig. 5.2: Simulated target without rotating parts

#### 5.4.1 Simulated Helicopter Target

The motion compensated range profile simulating a helicopter target is shown in Fig. 5.3. The sinusoid in the range profile image represents the micro-Doppler effect. Applying the micro-Doppler separation steps described in the previous section, the micro-Doppler can be removed and the range profile after removing the micro-Doppler is shown in Fig. 5.4.

If the micro-Doppler is not removed, the ISAR image will be contaminated due to the interference from these rotating parts as seen in Fig. 5.5. After removing the micro-Doppler, the resulting ISAR image shows significant improvement as seen in Fig. 5.6 .

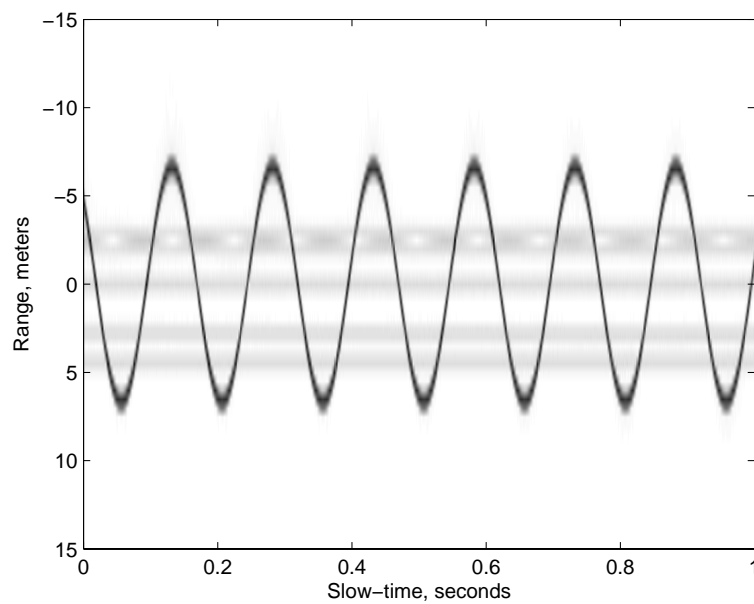


Fig. 5.3: Range profile of target with rotating parts before micro-Doppler separation

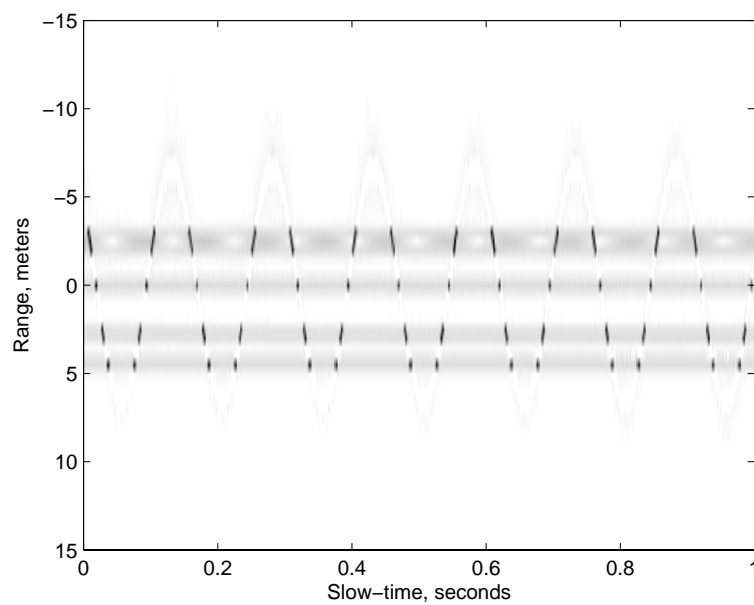


Fig. 5.4: Range profile of target with rotating parts after micro-Doppler separation

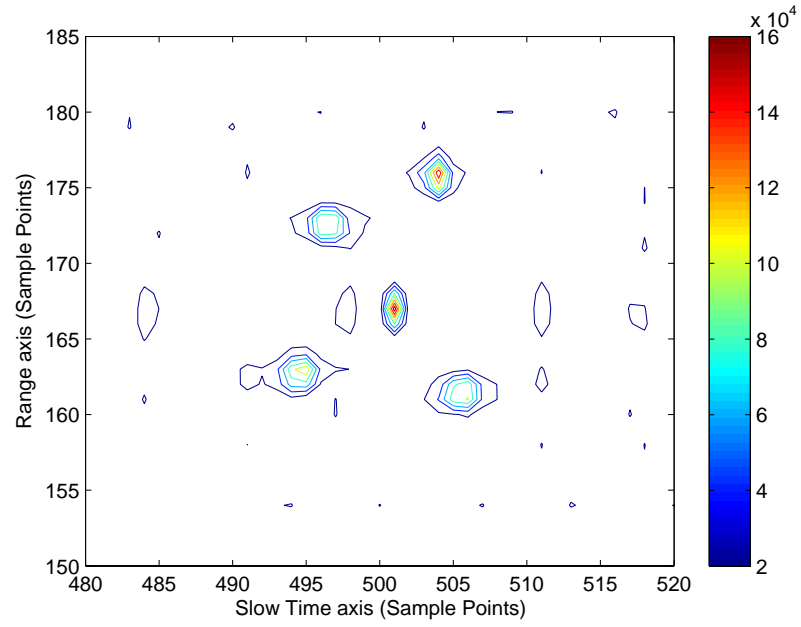


Fig. 5.5: ISAR image of target with rotating parts without micro-Doppler separation

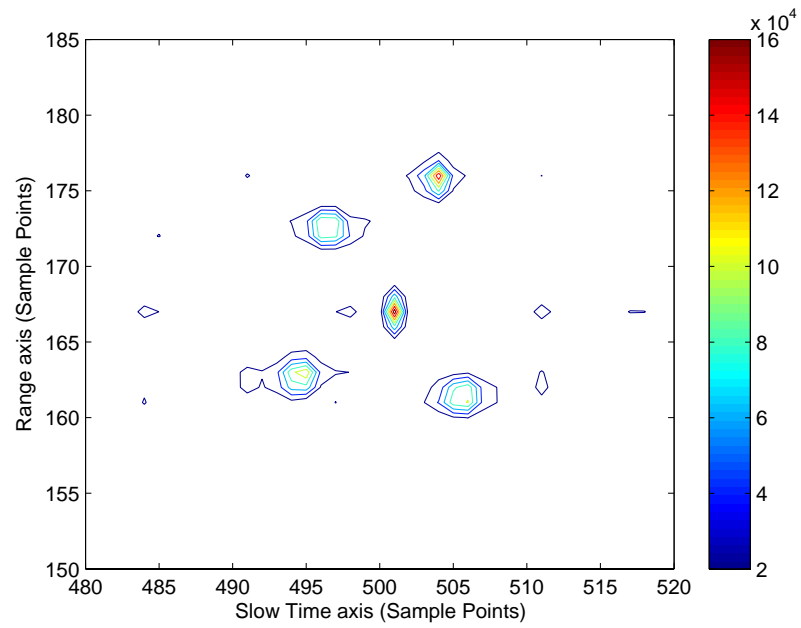


Fig. 5.6: ISAR image of target with rotating parts after micro-Doppler separation



### 5.4.2 Simulated Tank Target

For rigid body targets with irregularly moving or vibrating body parts, the micro-Doppler in the range profile image is not a sinusoid as in Section 5.4.1. Fig. 5.7 shows an example of the range profile of a tank target with its turret and gun moving in an irregular manner. It is different from the sinusoidal shape seen in the previous sub-section. In comparison, the range profile of an uncontaminated range profile is shown in Fig. 5.8.

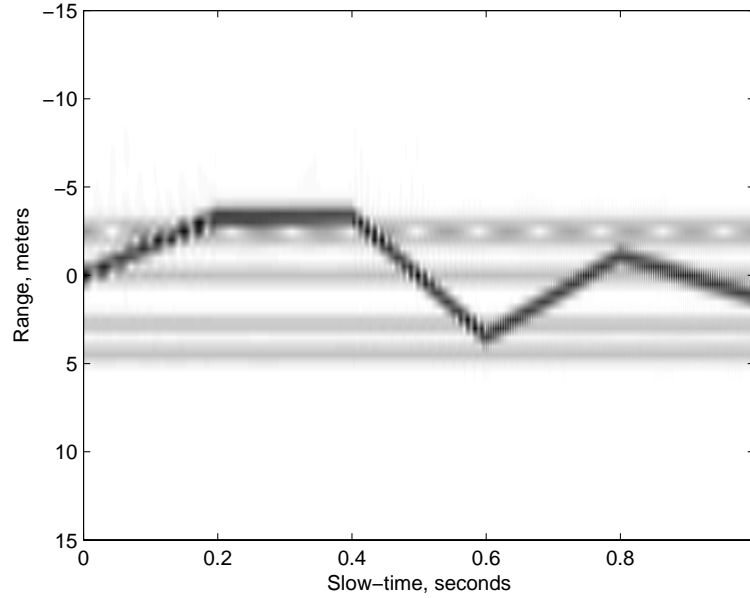


Fig. 5.7: Range profile of target with irregularly moving parts before micro-Doppler separation

The range profile after removing the micro-Doppler is shown in Fig. 5.9. It is shown that the micro-Doppler can be separated and removed.

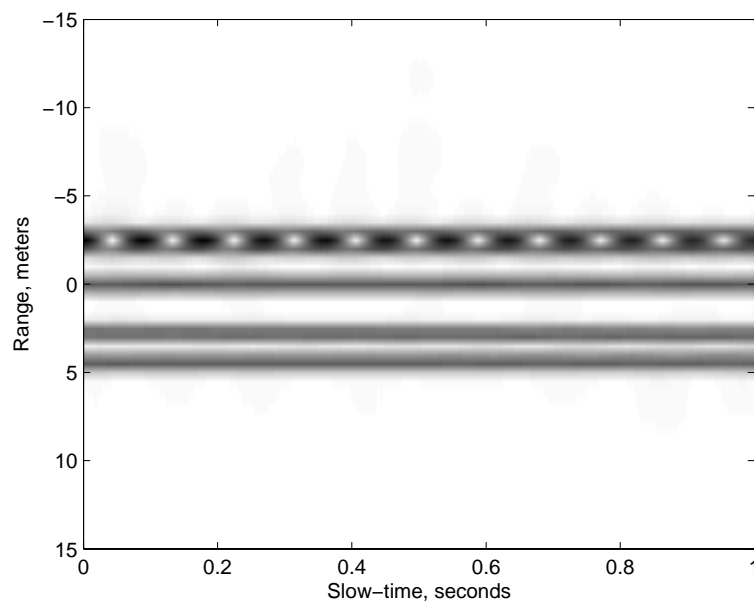


Fig. 5.8: Range profile of target without micro-Doppler contamination

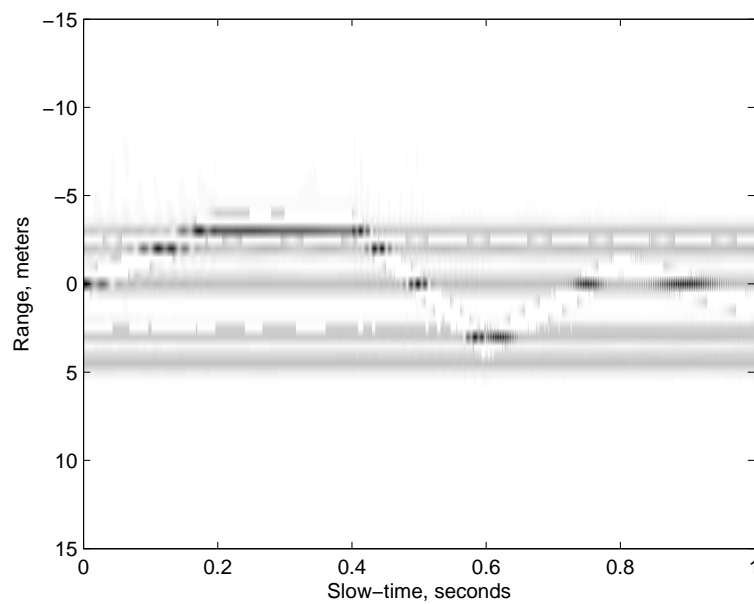


Fig. 5.9: Range profile of target with irregularly moving parts after micro-Doppler separation

The resulting ISAR image before and after micro-Doppler detection and removal is shown in Fig. 5.10 and Fig. 5.11 respectively. The processed ISAR image shows an improvement with the micro-Doppler removed.

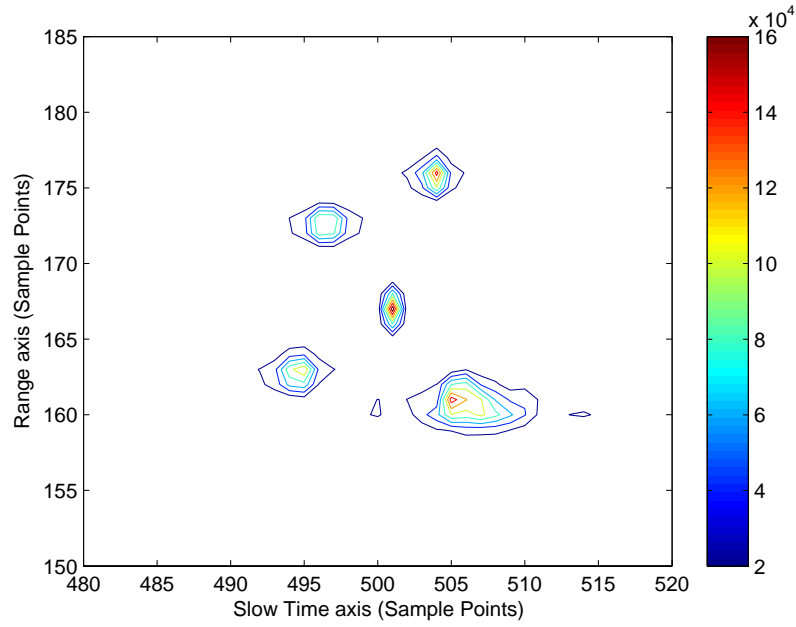


Fig. 5.10: ISAR image of target with irregularly moving parts without micro-Doppler separation

From both simulations above, we have demonstrated that the method is effective in improving the ISAR image for both rigid body targets with rotating parts and other moving parts.

However, the challenges remains when dealing with real data. The return signal due to the micro-Doppler may be much weaker or masked by the main body depending on its position, and may not be easily distinguishable from the rigid

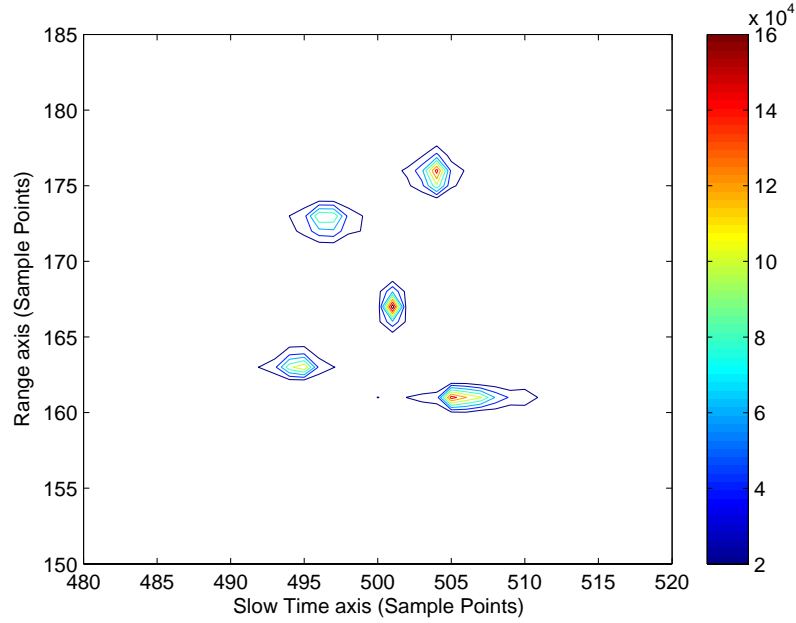


Fig. 5.11: ISAR image of target with irregularly moving parts after micro-Doppler separation

body scatterers. Therefore, it may not be totally removed, and any remaining micro-Doppler would contaminate the image.

## 5.5 Conclusions

We have discussed the problem of the micro-Doppler phenomenon caused by mechanical vibrations, movements or rotations of structures in a target. This means that the body image will be contaminated due to the interference from these rotating or moving parts. The simulation results have shown that the micro-Doppler can be separated in the Range Profile image and a better ISAR image can be obtained using the proposed separation method.

# Chapter 6

## Imaging of a Helicopter Target

### 6.1 Introduction

The basics of ISAR imaging and its applications has been discussed in the previous chapters. In general, ISAR imaging comprises of the following three steps, namely envelope alignment, radial motion compensation and spectrum analysis. Envelope alignment is the first step and alignment precision to one-eighth of a range cell is often necessary.

There are many papers that had discussed the problem of range alignment[12][69][100][101][102]. In [12], range alignment was implemented by locking the first strong peak of each pulse return into a specific range bin. Due to target scintillations, this range-locking method is not always reliable[69]. In [69], an adaptive

algorithm is presented. The algorithm uses the envelope correlation of the different echoes, while the reference envelope is obtained by exponentially averaging the previously received envelopes. Entropy minimum criterion has also been proposed [100] to replace the correlation maximum criterion in [69].

Conventional envelope alignment method of Inverse Synthetic Aperture Radar (ISAR) imaging assumes that the target is a rigid body, and therefore, the correlation between one-dimensional range profiles at neighboring time slots gives a larger value compared to correlation between time separated range profiles. But this is not the case for targets such as helicopter which have rotating body parts. According to the analysis of [103], [104] and [105], the reflected signal from the rotor is a "flashing-like" signal and the strength of the signal has the strongest value when the blade is perpendicular to the wavefront. Therefore its envelope is not a slow-time varying signal in the slow-time domain and conventional envelope alignment methods based on rigid target assumption is not suitable in this case.

In [101], an envelope alignment method for a target with a rotor is presented. The dynamic range of the range profile is used to judge if the range profile is severely affected by the rotor. Range profiles affected slightly are collected and averaged to form the reference range profile for range alignment. An amplitude limiter was also used to weaken the signal from the rotor. In the ISAR image

formed by [101], although the effects of the rotor are weakened, they can still be seen.

### 6.1.1 Problems Examined

In this chapter, the ISAR imaging for a helicopter target is proposed. An envelope alignment algorithm and zero-force windowing method is proposed. The target is assumed to have a trajectory described by a polynomial function during the imaging interval.

In our proposed method, for every range profile, correlation with other range profiles are done and the range profiles with a large correlation value are used to provide an initial estimate of the target motion parameters by polynomial fitting. By carrying out averaging on the estimated parameters, the effects of noise can be reduced. Also, as the rotor's signal is a "flashing-like" signal and the target body's signal is a slow-time varying signal, the difference of the received signal in slow time domain will generate peaks when there are strong return signals from the rotor. Zero-force windowing done at the flash position will weaken the effect of the rotor signal and improve the ISAR image of the helicopter body. Simulation results have shown the effectiveness of this algorithm.

## 6.2 Simulation Model

The geometry of the radar and the target is shown in Figure 6.1.

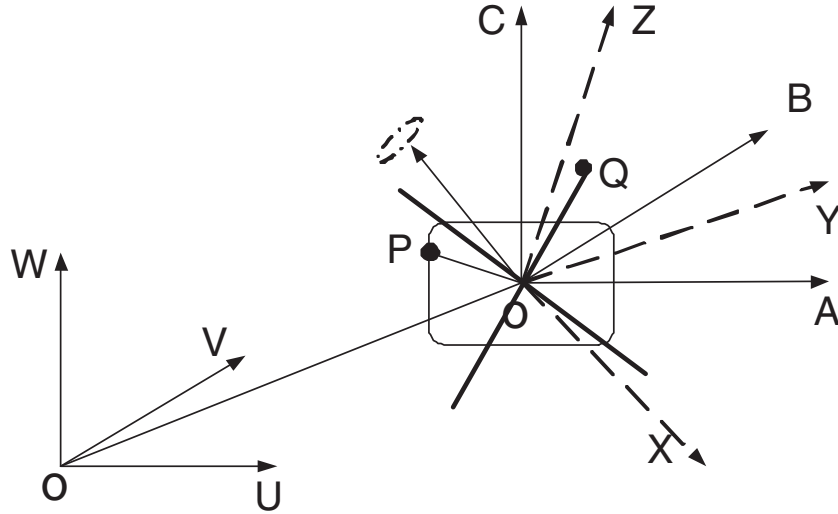


Fig. 6.1: Geometry of the radar and target.

The radar is located on the origin of the coordinate system  $(U, V, W)$ . There is a rotator on the target. There are two local coordinates on the target, one is  $(A, B, C)$  parallel to the coordinate system  $(U, V, W)$ , the other is the local coordinate system  $(X, Y, Z)$  which takes reference to the target and changes its orientation as the target maneuvers. The rotor rotates about its rotational axis with rotation speed  $\omega(t)$  while the coordinate transform matrix from  $(X, Y, Z)$  to  $(A, B, C)$  is  $\mathbf{T}$ , which is determined by the change of the target's pose.  $\mathbf{r}_0(t)$  is the vector of the reference point of the target relative to the coordinate  $(U, V, W)$ . So any point  $p$  on the target can be expressed in  $(U, V, W)$  coordinate as



$$\mathbf{r}(t) = \mathbf{r}_0(t) + \mathbf{T} \times \mathbf{p} \quad (6.1)$$

Let  $\omega(\mathbf{t})$  denote the rotation vector of the rotor in coordinate  $(X, Y, Z)$ . The instantaneous speed of any point  $Q$  on the rotor can be expressed as

$$\mathbf{q}(t) = \omega(\mathbf{t}) \times \overrightarrow{\mathbf{OQ}} \quad (6.2)$$

where  $\times$  is the vector cross product. The instantaneous vector of  $Q$  is

$$\overrightarrow{\mathbf{OQ}}(t) = \overrightarrow{\mathbf{OQ}}(0) + \int_0^t \mathbf{q}(t') dt' \quad (6.3)$$

therefore the instantaneous position of the point  $Q$  in the  $(U, V, W)$  coordinate system can be expressed as

$$\mathbf{r}_Q(t) = \mathbf{r}_0(t) + \mathbf{T} \times \overrightarrow{\mathbf{OQ}}(t) \quad (6.4)$$

The scalar range is

$$r_Q(t) = \|\mathbf{r}_0(t) + \mathbf{T} \times \overrightarrow{\mathbf{OQ}}(t)\| \quad (6.5)$$

where  $\|\cdot\|$  represents the Euclidean norm.

The rotor blade can be modeled as a stiff rod of length  $L$ . Let us consider a

rotor blade positioned at an angle  $\phi$  relative to the radar beam. Using a narrow-band signal, the wave reflected from the blade after demodulation will take the form[104][105]

$$\begin{aligned} u_r &= \int_0^l \exp(-j2\pi \frac{2x \cos \phi}{\lambda}) dx \\ &= L \times \exp(-j \frac{2\pi L \cos \phi}{\lambda}) \times \text{sinc}(\frac{2L \cos \phi}{\lambda}) \end{aligned} \quad (6.6)$$

where  $\lambda$  is the wavelength,  $\text{sinc}(x) = \frac{\sin(x)}{x}$ . The signal takes maximum value when the blade is perpendicular to the radar beam and drops sharply when the blade has rotated a few degrees[103].

In radar imaging, a wideband signal is transmitted. Let the transmitted wide-band linear frequency modulated signal be

$$s(t) = \chi(t) \exp\{j2\pi(ft + \frac{\mu}{2}t^2)\} \text{ for } |t| < \frac{T}{2} \quad (6.7)$$

where  $f$  is the carrier frequency,  $\mu$  is the chirp rate and  $T$  is the chirp pulse duration.  $\chi(t)$  is the envelope of the transmitted signal satisfying  $\chi(t) = 1$ , for  $|t| < \frac{T}{2}$ , and  $\chi(t) = 0$ , for  $|t| > \frac{T}{2}$ . The received signal is thus

$$r(t) = \rho \times \chi(t - \tau) \exp\{j2\pi[f(t - \tau) + \frac{\mu}{2}(t - \tau)^2]\} \quad (6.8)$$

After demodulation and match filtering, the received signal can be expressed as

$$\tilde{r}(t) = \rho \times \chi(t - \tau) \exp(-j2\pi f) \times \text{sinc}(\mu T(t - \tau)) \quad (6.9)$$

As the whole range is divided into different range cells, the scattered signal from the blade will be dispersed into different range cells at time instances where the blade is not perpendicular to the radar beam. The total signal received is the sum of the blade signal and the signal scattered from the helicopter's body.

### 6.3 Envelope Alignment and Zero-force Windowing

Conventional envelope alignment methods include the strongest scatter tracking [12], correlation maximization [69] and entropy minimization algorithms [100], etc.. Algorithms in [101] and [102] claimed that they are suitable for target with a rotating part and provided some simulation results. However, the algorithm of [101] requires a key threshold parameter to be manually selected and the computational complexity of [102] is high.

In this chapter, we assume that the moving trajectory of the target can be approximated by a polynomial function during data collection. Let  $I(m, n)$  be the

one-dimensional range profile where  $0 \leq m \leq M - 1$  and  $0 \leq n \leq N - 1$ . The proposed envelope alignment algorithm can be summarized using the following pseudo codes:

**For**  $n = 0$  **to**  $N - 1$

**Step 1:** Compute the correlation between  $I(:, n)$  and the shifted version of  $I(:, k)$ ,  $k \neq n$ ; and get the position  $p(k)$  where maximum value  $C(k)$  of correlation occurs.

**Step 2:** Select  $k$ , such that  $C(k)$  belongs to the first  $K$  largest value of the set  $C(:)$ . Denote the set of the selected  $k$  as  $P(n)$ .

**Step 3:** Polynomial fitting is then used to fit the  $K$ 's  $p(k)$ . Let the order of polynomial function be  $L$  and then solve the least square equation

$$a_n(0) + a_n(1) \times k + \dots + a_n(L) \times k^L = p(k) \quad (6.10)$$

The polynomial coefficients is denoted as  $\mathbf{a}_n$ .

**End of code**

The average of  $\mathbf{a}_n$ , denoted as  $\bar{\mathbf{a}}$ , is the estimation of the target motion parameters vector. The range adjustment value can be obtained by computing the

polynomial function

$$M(k) = \bar{a}(1) \times k + \bar{a}(2) \times k^2 + \dots + \bar{a}(L) \times k^L \quad (6.11)$$

Motion compensation can be done using conventional methods and will not be discussed here. As the signal from the rotor is a "flash-like" signal in the time domain, the performance of the ISAR image will be improved if the "flash-like" signal is removed. The key to doing so is to determine its position. As the envelope of the one-dimensional range profile of the target body is a slow time-varying signal, while the rotor's signal is a fast time-varying signal at the flashing point, a difference or high pass filter can be used to determine the position of flash point.

Let  $\tilde{I}$  be the norm of the one-dimensional range profile. The difference of the range profile at different slow-time is

$$\hat{I}(:, n) = |\tilde{I}(:, n+1) - \tilde{I}(:, n)|, \quad n = 0, \dots, N-2 \quad (6.12)$$

The sum of the  $\hat{I}$  in the range and slow-time direction is  $S1$  and  $S2$  respectively, where

$$S1(n) = \sum_{m=0}^{M-1} \hat{I}(m, n), \quad n = 0, \dots, N-2 \quad (6.13)$$

and

$$S2(m) = \sum_{n=0}^{N-2} \hat{I}(m, n), \quad m = 0, \dots, M-1 \quad (6.14)$$

The peaks of  $S1$  and  $S2$  correspond to the position of the flash signal in the slow-time and range domain, respectively. Assume that the rotor rotates with a speed of 5 Hz and the PRF of the Radar is 1000 Hz, then the rotor rotates  $1.8^\circ$  between two pulses. Because the flash signal falls by 20 dB within a  $2^\circ$  rotation[103], the signals from the rotor are periodic pseudo "dirt" function.

For the case where the range resolution of the wideband signal is about 0.5 m and the length of the blade is about 10 m, when the blade has rotated such that the distance difference of the two end of the blade relative to the radar is one range resolution cell, the rotated angle would be  $\arcsin(0.5/10) = 2.9^\circ$ . This is greater than the correlation angle, and the return signal from the rotor would be almost zero. Therefore the flash signal is mainly limited to one range cell. Based on these, we propose that the one-dimensional range profiles at the flash position be masked by a zero. A bigger masked area is better for rotor signal suppression, but will induce a poorer spectrum resolution and leads to helicopter body signal suppression.

## 6.4 Simulation Results

In this section, some simulation results are provided to verify the effectiveness of our method. The distance from the target to the radar is 10 km, the transmitted signal's wavelength is  $\lambda = 0.03$  m, signal bandwidth is 300 MHz corresponding to a range resolution of 0.5 m. The pulse repetition frequency is 80 Hz. The target's body comprises of 10 strong scatterers. There are 2 blades with length  $L = 12$  m. The figure of the target is shown in Figure 6.2. Here, some scatterers are simulated at the  $Y = -1$  position instead of at the  $Y = 0$  position. This is to allow us to clearly see the alignment of the rotor flash.

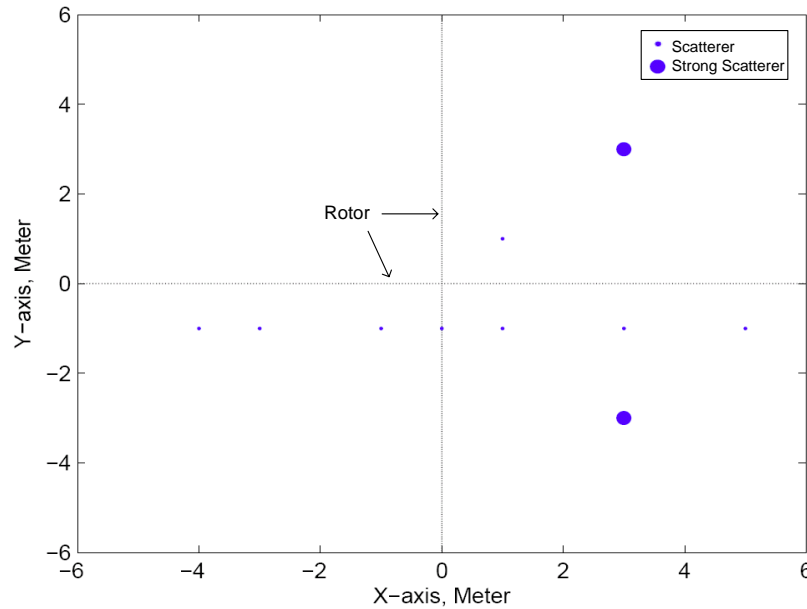


Fig. 6.2: Projected image of the target.

The volume of the point is used to express the power of the scatterer, with a higher power being represented by a larger volume. The target moves along a

straight line with speed  $V_x = 30$  m/s,  $V_y = 3$  m/s and  $V_z = 0$  m/s. The data collection time is 10 s and during this time, the cross-range moved is 300 m, which corresponds to a relative rotated angle of  $1.7189^\circ$  and resulting cross-range resolution of 0.5 m. There are 8 sampling points in one range cell. The range profile aligned using conventional correlation method[69] and our method are shown in Figure 6.3 and Figure 6.4 respectively.

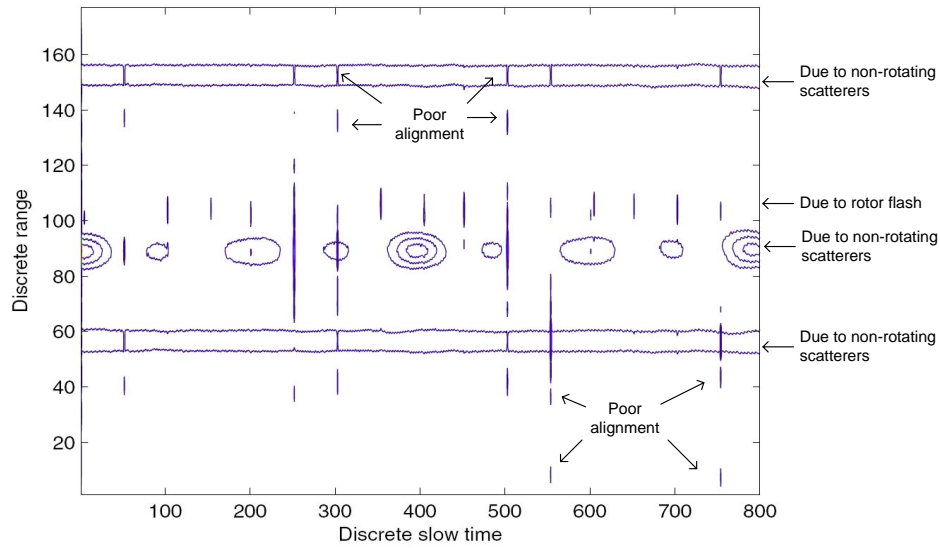


Fig. 6.3: Range profile after alignment using conventional method[69].

In Figure 6.3, the straight horizontal lines are due to the scatterers while the short vertical lines are due to the rotor "flashes". It can be seen that the alignment is not good as the flashes appears at different ranges although it should be located at around range cell 100. In comparison, the range profile using our proposed method is very well aligned with the flashes contained near range cell 90. Using



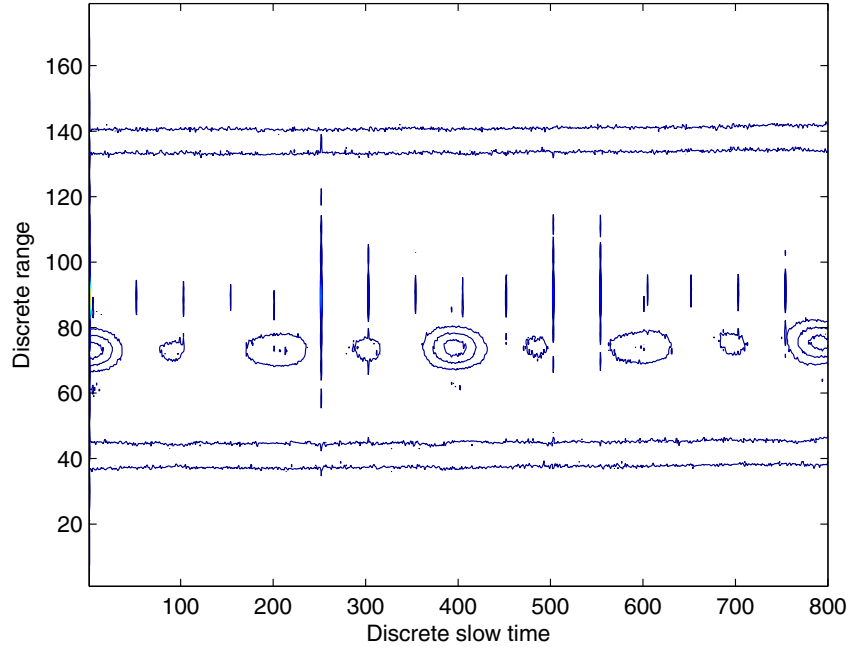


Fig. 6.4: Range profile after alignment using the proposed method.

conventional method, errors usually occur at the positions of the flash and this will influence the selection of the isolated scatterer for motion compensation. The variances of the signal of Figure 6.3 and Figure 6.4 in slow time domain are shown in Figure 6.5 and Figure 6.6 respectively.

It can be seen that the alignment of Figure 6.6 is much better compared to Figure 6.5 as the rotor flashes are contained near the center of the range profile. The plot of  $S1$  and  $S2$  are shown in Figure 6.7 and Figure 6.8 respectively.  $S1$  obtained by using the range profile method of [69] and our method are plotted in Figure 6.7. They are plotted with an offset in amplitude so that the result of the two methods can be clearly seen. The plot shows that the alignment using the

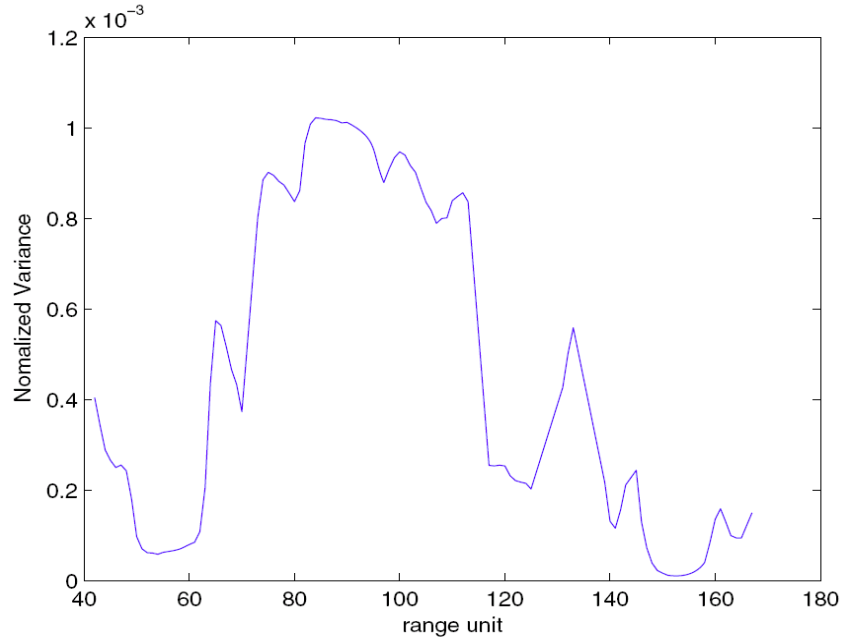


Fig. 6.5: Variance of range profile using conventional method[69].

proposed method is better as the amplitude across the cross-range is almost constant except at the flash positions. In comparison, the amplitude variation using the method of [69] is greater. The flash position can be easily obtained from these plots.

The ISAR images using the conventional method[69] and our method are shown in Figure 6.9 and Figure 6.10 respectively. Figure 6.10 shows a better ISAR image compared to Figure 6.9 as we see that the unwanted sidelobes in the cross-range direction has been suppressed. It is also similar to the original target shown in Figure 6.2. It is seen that the effects of the rotor have been effectively removed using our method.

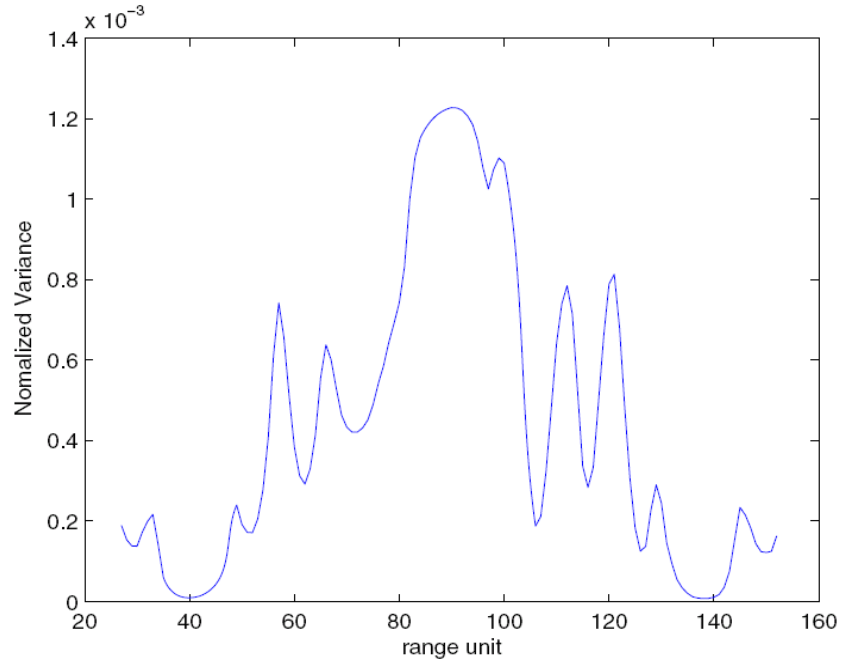


Fig. 6.6: Variance of range profile using the proposed method.

## 6.5 Conclusions

In this chapter, an ISAR imaging method for helicopter is proposed. Polynomial fitting is used to obtain the range trace of the target. Zero-force windowing is used to remove the signals from the rotor. Simulation results has shown the effectiveness of the proposed method.

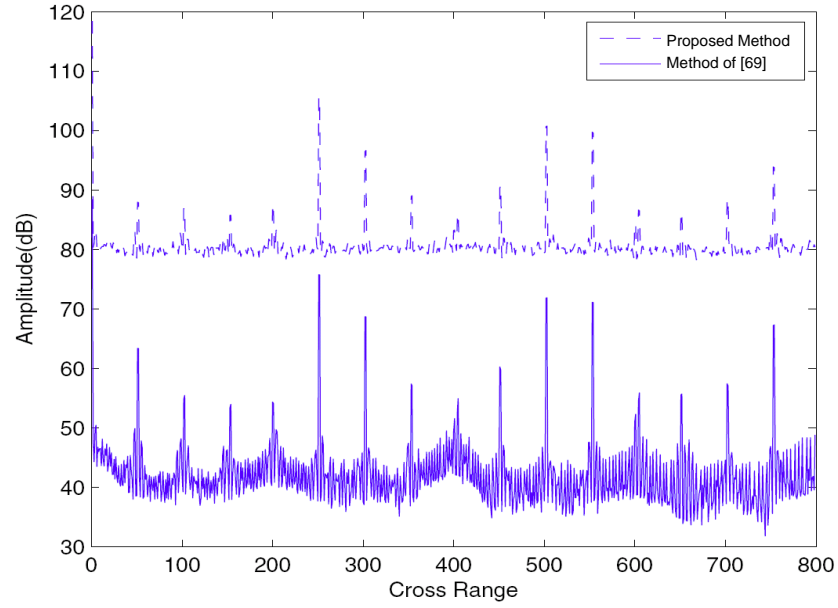


Fig. 6.7: S1, Positions of flash signals in the slow time domain.

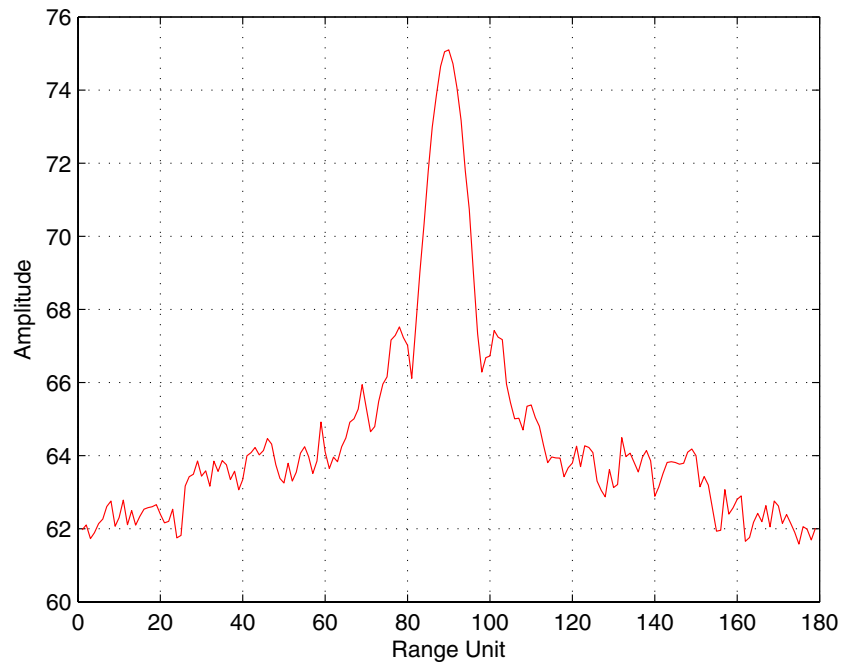


Fig. 6.8: S2, Positions of flash signals in the range domain.

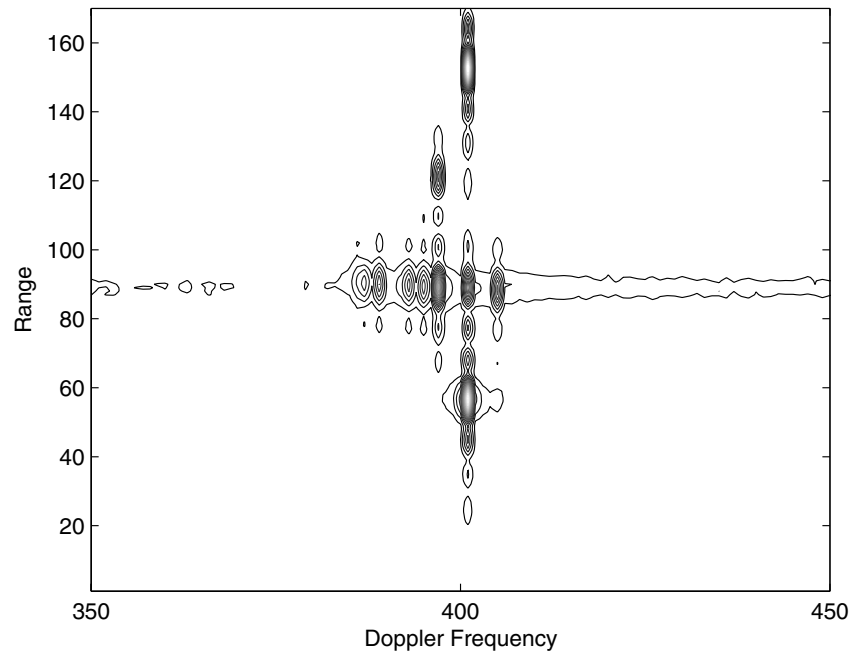


Fig. 6.9: ISAR image obtained using conventional method.

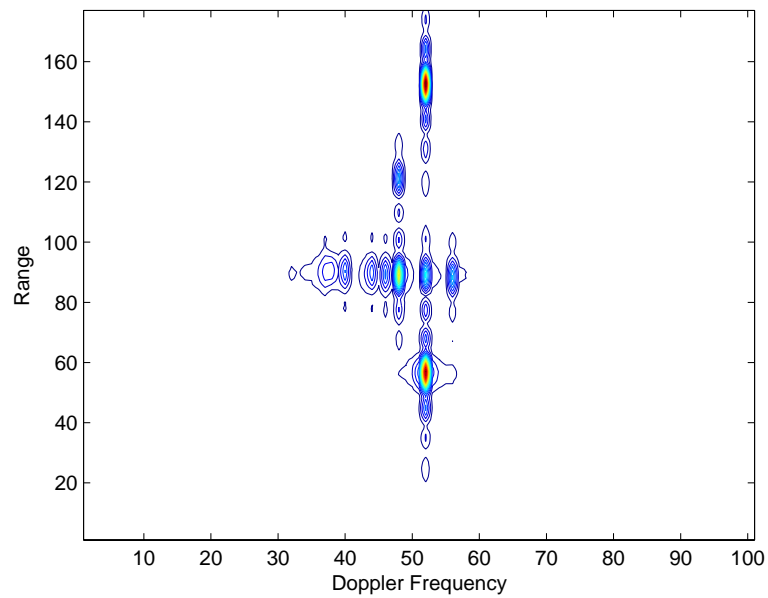


Fig. 6.10: ISAR image obtained using the proposed method.

# Chapter 7

## Conclusions

### 7.1 Summary of Work

The area of work undertaken is in the area of ISAR imaging, which has important applications in surveillance and target identification. The thesis presents improved methods to solve several previously unresolved issues, thereby improving the quality of ISAR images. My work covers the areas of array-based ISAR imaging and imaging of targets exhibiting the micro-Doppler phenomena. For array-based ISAR imaging, a perpendicular array method and a sparse array method have been proposed; while an extended Hough Transform and Range Grouping method has been proposed to extract the micro-Doppler contribution of both regular and irregular body parts of a target. This is followed by the imaging of a helicopter target.

In the antenna array imaging method, a three-dimensional imaging method using two perpendicular antenna arrays along with the method for motion compensation and scatterer registration strategy was proposed. The array-based method allows synthesis scatterers to be separated and this significantly improves the identifiability of a target.

The antenna array method was enhanced by using two-dimensional sparse-array beamforming combined with ISAR imaging. The advantage of a sparse array is that it achieves a wider aperture while the number of antenna elements can be greatly reduced compared to a full array. The method also solves the scatterer registration challenge which exists for the antenna array method.

The next part of the thesis deals with the issue of micro-motions known as the micro-Doppler phenomenon. Micro-Doppler contamination has to be extracted, otherwise it causes blurring of ISAR images. In our work, a separation method using the standard Hough Transform and extended Hough Transform is proposed to remove the micro-Doppler contamination caused by the rotating body part of a target.

Although the micro-Doppler removal using the extended Hough Transform is

effective for a target with a regular rotating body part, it is not suitable for a target with an irregular moving body part. A Range Grouping method is therefore proposed for micro-Doppler removal. This method has been shown to be effective for other complex micro-movements that one may wish to detect. An example of such a target would be the movement of the turret and gun of a tank which is not in a regular circular motion.

Finally the imaging of a helicopter target is considered. The helicopter target is a challenging target as the signal contributions from the rotors would affect the envelope alignment step. Here, an envelope alignment algorithm and zero-force windowing method are proposed.

In all the proposed works, the simulated results shows that the proposed methods are effective and lead to a great improvement in the processed ISAR image. A summary of the work done in this thesis is shown in Table 7.1.

Type of target	Method	Section
1) Rigid body, constant speed, uniformly rotating part	a) Extended Hough Transform	4.3.2
	b) Zero-Force Windowing	6.3
2) Rigid body, constant speed, non-uniformly rotating part	a) Range Grouping	5.2
3) Rigid body, maneuvering	a) Sparse Array	3.4.3
4) Rigid body, maneuvering, with rotating part	Future Work	-

Table 7.1: Summary of work.



## 7.2 Contributions

In this section, we discuss the contributions made in our course of work versus existing methods for imaging.

The proposed antenna array imaging method allows for three-dimensional imaging of targets with synthesis scatterers. The existence of synthesis scatterers is likely to occur for a real world target as targets are made up of many scatterers. It is possible for scatterers to be at different physical positions, but are projected onto the same point on the range-Doppler plane. Thus previous methods such as InISAR systems fail to create an acceptable three-dimensional ISAR image when synthesis scatterers exist. Using the proposed antenna array method, the correct calculation of the scatterers' position would result in a clearer three-dimensional image for easier classification and identification.

The antenna array method, however, may not be suitable for maneuvering targets unless methods such as time frequency techniques are used. This led to the proposed sparse-array method which allows for a simple method for imaging a maneuvering target. Due to the large aperture formed by the sparse array, a long coherent time duration is not needed to separate scatterers. Therefore, during a short time duration, the rotation of the target relative to the antenna array may

be approximated as an uniform rotation. Techniques such as time frequency analysis or super resolution spectrum analysis are not necessary and processing is very much simplified.

In real-life situations, targets are unlikely to be a completely rigid targets. There may be rotating body parts or vibrations in the engine of a vehicle, which can cause image blurring. The micro-Doppler extraction using the extended Hough Transform method allows for imaging of target with non-rigid body parts that cannot be done using conventional range-Doppler principles. With the separation and removal of the micro-Doppler contamination, an improved ISAR image can be obtained. The proposed method is simpler compared to previous methods using high resolution time-frequency techniques as it is done on the range profile image instead of at the signal level. Micro-Doppler information can also provide information on the rotating body part and help in radar target identification and classification.

There may also be other complex micro movements that one may wish to detect, like the movement of the gun on a tank target. Micro-Doppler removal by Range Grouping proposed in our work is more effective compared to previous methods using high-resolution time-frequency analysis, as there is no specific equations describing such random rotations or motions. It is also simple as it is carried out on the range profile image instead of at the signal level.

### 7.3 Future Work

The next step to proceed forward would be to combine the techniques of three-dimensional array imaging and micro-Doppler extraction for imaging of non-rigid targets. This way, a more realistic target can be imaged. An area we would like to work on is to produce a three-dimensional ISAR image of a moving tank target. The movement of the turret and gun of a tank would not be in a regular circular motion like in the case of the rotor of a helicopter. The turret may be moving in a clockwise or anti-clockwise movement, and the gun may be moving vertically up or down according to operational requirements. This makes it a challenging target which could not be correctly imaged using previous techniques.

Another area which we feel that may be worth exploring would be in the imaging of Unmanned Aerial Vehicle(UAV). Modern warfare makes extensive use of UAV for reconnaissance or even huge UAV for bombing. Thus, identifying and classification of a UAV and determining its threat will be of great importance as its use becomes more prevalent. However the imaging of UAV remains challenging as the size may vary greatly from hand-launched UAV to full size UAV. The body may also be made of composite materials which have low radar reflectivity. Imaging may have to be focussed on certain components like UAV propeller, engines,

pitot-static tubes and sensors or trays which are metal.

# Appendix A

## Derivation of Equations

### A.1 Derivation of (3.28)

In our derivation, we use the following approximation  $\frac{1}{r} \approx \frac{1}{\tilde{r}}$ , where  $r$  and  $\tilde{r}$  are two large enough numbers and  $|r - \tilde{r}|$  is a small value. The relative difference  $|(\frac{1}{r} - \frac{1}{\tilde{r}})/\frac{1}{\tilde{r}}| = |\frac{r-\tilde{r}}{\tilde{r}}| \ll 1$ , is a small value. First we simplify the phase term of (3.7).

$$\begin{aligned}
\Delta r_{PQk} &= \frac{2(\mathbf{r} + \mathbf{q})^T \mathbf{d}_k - \mathbf{d}_k^T \mathbf{d}_k}{(r_{q0} + r_{qk})} - \frac{2(\mathbf{r} + \mathbf{p})^T \mathbf{d}_k - \mathbf{d}_k^T \mathbf{d}_k}{(r_{p0} + r_{pk})} \\
&= \frac{(2(\mathbf{r} + \mathbf{q})^T \mathbf{d}_k - \mathbf{d}_k^T \mathbf{d}_k)(r_{p0} + r_{pk}) - (2(\mathbf{r} + \mathbf{p})^T \mathbf{d}_k - \mathbf{d}_k^T \mathbf{d}_k)(r_{q0} + r_{qk})}{(r_{p0} + r_{pk})(r_{q0} + r_{qk})} \\
&\approx \frac{(2\mathbf{r}^T \mathbf{d}_k(r_{p0} + r_{pk} - r_{q0} - r_{qk}) + 2\mathbf{q}^T \mathbf{d}_k(r_{p0} + r_{pk}) - 2\mathbf{p}^T \mathbf{d}_k(r_{q0} + r_{qk}))}{4\tilde{r}^2} \\
&\quad + \frac{(\mathbf{d}_k^T \mathbf{d}_k(r_{q0} + r_{qk} - r_{p0} - r_{pk}))}{4\tilde{r}^2}, \tag{A.1}
\end{aligned}$$

where  $\tilde{r} \approx r_{p0}$ . As

$$\frac{2\mathbf{r}^T \mathbf{d}_k(r_{p0} + r_{pk} - r_{q0} - r_{qk})}{4\tilde{r}^2} \approx -\mathbf{n}_0^T \mathbf{d}_k \overrightarrow{PQ}^T \mathbf{n}_0 / \tilde{r}, \quad (\text{A.2})$$

we use the approximation  $\mathbf{r}/\tilde{r} \approx \mathbf{n}_0$  (The radar line of sight unit vector),  $r_{p0} - r_{q0} \approx -\overrightarrow{PQ}^T \mathbf{n}_0$  and  $r_{pk} - r_{qk} \approx -\overrightarrow{PQ}^T \mathbf{n}_0$ ,

$$\begin{aligned} & (2\mathbf{q}^T \mathbf{d}_k(r_{p0} + r_{pk}) - 2\mathbf{p}^T \mathbf{d}_k(r_{q0} + r_{qk})) / (4\tilde{r}^2) \\ &= (2\mathbf{q}^T \mathbf{d}_k(r_{p0} + r_{pk}) - 2\mathbf{p}^T \mathbf{d}_k(r_{p0} + r_{pk}) + 2\mathbf{p}^T \mathbf{d}_k(r_{p0} + r_{pk}) - 2\mathbf{p}^T \mathbf{d}_k(r_{q0} + r_{qk})) / (4\tilde{r}^2) \\ &= \frac{2\overrightarrow{PQ}^T \mathbf{d}_k(r_{p0} + r_{pk})}{4\tilde{r}^2} - \frac{\mathbf{p}^T \mathbf{d}_k \overrightarrow{PQ}^T \mathbf{n}_0}{\tilde{r}^2} \\ &= \frac{\overrightarrow{PQ}^T \mathbf{d}_k}{\tilde{r}} - \frac{\mathbf{p}^T \mathbf{d}_k \overrightarrow{PQ}^T \mathbf{n}_0}{\tilde{r}^2}, \end{aligned} \quad (\text{A.3})$$

and

$$\frac{\mathbf{d}_k^T \mathbf{d}_k(r_{q0} + r_{qk} - r_{p0} - r_{pk})}{4\tilde{r}^2} = \frac{\mathbf{d}_k^T \mathbf{d}_k \overrightarrow{PQ}^T \mathbf{n}_0}{2\tilde{r}^2}, \quad (\text{A.4})$$

Therefore, we have

$$\begin{aligned} \Delta r_{PQk} &= -\mathbf{n}_0^T \mathbf{d}_k \overrightarrow{PQ}^T \mathbf{n}_0 / \tilde{r} + \frac{\overrightarrow{PQ}^T \mathbf{d}_k}{\tilde{r}} - \frac{\mathbf{p}^T \mathbf{d}_k \overrightarrow{PQ}^T \mathbf{n}_0}{\tilde{r}^2} + \frac{\mathbf{d}_k^T \mathbf{d}_k \overrightarrow{PQ}^T \mathbf{n}_0}{2\tilde{r}^2} \\ &\approx \frac{(\overrightarrow{PQ} - \overrightarrow{PQ}^T \mathbf{n}_0 \mathbf{n}_0)^T \mathbf{d}_k}{\tilde{r}} \end{aligned} \quad (\text{A.5})$$

Here we assume that the target is small and that the antenna array configuration satisfies  $\mathbf{d}_k^T \mathbf{d}_k / \tilde{r} \ll 1$ . Then the array signal can be simplified as

$$\hat{\mathbf{s}}_q(t) = e^{-j4\pi \frac{r_{q0}(t) - r_{p0}(t)}{\lambda}} \times [1, \dots, e^{\frac{j2\pi(\vec{P}\vec{Q} - \vec{P}\vec{Q}^T \mathbf{n}_0 \mathbf{n}_0)^T \mathbf{d}_k}{\lambda \tilde{r}}}, \dots] \quad (\text{A.6})$$

It should be noted that (A.6) holds only when (1): the target is located in far field and the size of the target is small, (2): the distance moved by the target in the range direction is small, and (3): the size of the antenna array is small compared to the distance  $\tilde{r}$ .

Next, we simplify the time domain phase  $r(t) = r_{q0}(t) - r_{p0}(t)$ . Although this has been discussed in previous literatures, most of them covered targets with only either translational or rotational motion. We consider a target with simultaneous translational and rotational motion. We assume the translational velocity vector of the target be  $\mathbf{v}$ , and that it rotates around its rotational axis  $\boldsymbol{\omega} = [\omega_x, \omega_y, \omega_z]^T (|\boldsymbol{\omega}| = 1)$  with a rotational speed  $\Omega$ . Define a skew symmetric matrix

$$\hat{\boldsymbol{\omega}} = \begin{pmatrix} 0 & -\omega_z & \omega_y \\ \omega_z & 0 & \omega_x \\ -\omega_y & \omega_x & 0 \end{pmatrix}, \quad (\text{A.7})$$

The rotation matrix can then be denoted as  $R(t) = I + \sin(\Omega t)\hat{\boldsymbol{\omega}} + (1 - \cos(\Omega t))\hat{\boldsymbol{\omega}}^2$  [77].

The instantaneous vector of  $P$  and  $Q$  are  $\mathbf{r}_p(t) = \mathbf{r} + \mathbf{v}t + R(t)\overrightarrow{OP}$  and  $\mathbf{r}_q(t) = \mathbf{r} + \mathbf{v}t + R(t)\overrightarrow{OQ}$  respectively. Denote  $\mathbf{p} = \overrightarrow{OP}$ ,  $\mathbf{q} = \overrightarrow{OQ}$ , then the difference in distance from  $O'$  to  $P$  and to  $Q$  are

$$\begin{aligned} r(t) &= r_{q0}(t) - r_{p0}(t) \\ &= \|\mathbf{r} + \mathbf{v}t + R(t)\mathbf{q}\| - \|\mathbf{r} + \mathbf{v}t + R(t)\mathbf{p}\| \\ &= \frac{2(\mathbf{r} + \mathbf{v}t)^T R(t)\overrightarrow{PQ} + q^2 - p^2}{r_{q0}(t) + r_{p0}(t)} \end{aligned} \quad (\text{A.8})$$

where  $p = |\mathbf{p}|$  and  $q = |\mathbf{q}|$  and  $R(t)^T R(t) = I$ . Usually,  $r(t)$  can be approximated as a linear function within a short time duration. We have

$$r(0) = \frac{2\mathbf{r}^T \overrightarrow{PQ} + q^2 - p^2}{r_p(0) + r_q(0)}, \quad (\text{A.9})$$

and

$$\begin{aligned} r'(t) &= \frac{2(\mathbf{v}^T R(t) + \mathbf{r}^T R'(t) + \mathbf{v}^T t R'(t))\overrightarrow{PQ}}{r_p(t) + r_q(t)} \\ &\quad - \frac{(2(\mathbf{r} + \mathbf{v}t)^T R(t)\overrightarrow{PQ} + q^2 - p^2)(r'_p(t) + r'_q(t))}{(r_p(t) + r_q(t))^2}. \end{aligned} \quad (\text{A.10})$$

$$r'_p(t) = \frac{(\mathbf{v} + R'(t)\mathbf{p})^T (\mathbf{r} + \mathbf{v}t + R(t)\mathbf{p})}{r_p(t)}, \quad (\text{A.11})$$

$$r'_q(t) = \frac{(\mathbf{v} + R'(t)\mathbf{q})^T (\mathbf{r} + \mathbf{v}t + R(t)\mathbf{q})}{r_q(t)}, \quad (\text{A.12})$$

Substituting  $r'_p(t)$  and  $r'_q(t)$  into  $r'(t)$  and solving, we obtain



$$\begin{aligned}
& r'(t)|_{t=0} \\
&= \frac{2(\mathbf{r}^T \Omega \hat{\omega} + \mathbf{v}^T) \vec{PQ}}{r_p(0) + r_q(0)} \\
&\quad - \frac{2\mathbf{r}^T \vec{PQ} + \mathbf{q}^T \mathbf{q} - \mathbf{p}^T \mathbf{p}}{(r_p(0) + r_q(0))^2} \times \left( \frac{(\mathbf{v} + \Omega \hat{\omega} \mathbf{p})^T (\mathbf{r} + \mathbf{p})}{r_p(0)} + \frac{(\mathbf{v} + \Omega \hat{\omega} \mathbf{q})^T (\mathbf{r} + \mathbf{q})}{r_q(0)} \right) \\
&\approx \mathbf{n}_0^T \Omega \hat{\omega} \vec{PQ} + \frac{\mathbf{v}^T \vec{PQ}}{\tilde{r}} - \frac{\mathbf{n}_0^T \mathbf{v} \mathbf{n}_0^T \vec{PQ}}{\tilde{r}} - \frac{\mathbf{n}_0^T \Omega \hat{\omega} \frac{\mathbf{p} + \mathbf{q}}{2} \mathbf{n}_0^T \vec{PQ}}{\tilde{r}} \\
&= ((\mathbf{v} - \mathbf{n}_0^T \mathbf{v} \mathbf{n}_0) / \tilde{r} - \Omega \hat{\omega} \mathbf{n}_0)^T \vec{PQ} \\
&= \vec{\nu}^T \vec{PQ}
\end{aligned} \tag{A.13}$$

where the fourth term  $\frac{\mathbf{n}_0^T \Omega \hat{\omega} \frac{\mathbf{p} + \mathbf{q}}{2} \mathbf{n}_0^T \vec{PQ}}{\tilde{r}}$  is omitted as it is much smaller compared to the other terms.  $\vec{\nu}$  is the synthetic vector which represents the effects induced by the target's translational and rotational motion.

Using (3.7), (A.6) and (A.13), we have obtained the simplified space time expression (3.9).

## A.2 Derivation of (4.4)

Here, we study in detail the Fourier properties of the received signal in the fast-time domain. Assume that the transmitted signal is  $p(t)$ , as shown in (4.3); then, the echoed signal can be rewritten as

$$\begin{aligned}
s(t, \tau) = & \sum_m \sigma_m \operatorname{rect} \left( \frac{t - \frac{2R_m(\tau)}{c}}{T_p} \right) \cdot \exp \left( j2\pi \left( f_c \left( t - \frac{2R_m(\tau)}{c} \right) + \frac{1}{2}\mu \left( t - \frac{2R_m(\tau)}{c} \right)^2 \right) \right) \\
& + \sum_n \sigma_n \operatorname{rect} \left( \frac{t - \frac{2R_n(\tau)}{c}}{T_p} \right) \cdot \exp \left( j2\pi \left( f_c \left( t - \frac{2R_n(\tau)}{c} \right) + \frac{1}{2}\mu \left( t - \frac{2R_n(\tau)}{c} \right)^2 \right) \right)
\end{aligned} \tag{A.14}$$

where  $c$  is the wave propagation speed,  $\sigma_m$  and  $\sigma_n$  are the complex scattering coefficients, and  $R_m(\tau)$  and  $R_n(\tau)$  are the distances of the non-rotating scatter points and the rotating scatter points from the radar at the slow-time  $\tau$ , respectively. Let the center of the target be the reference point. Then, the reference signal is

$$s_r(t, \tau) = \operatorname{rect} \left( \frac{t - \frac{2R_c(\tau)}{c}}{T_{ref}} \right) \cdot \exp \left( j2\pi \left( f_c \left( t - \frac{2R_c(\tau)}{c} \right) + \frac{1}{2}\mu \left( t - \frac{2R_c(\tau)}{c} \right)^2 \right) \right) \tag{A.15}$$

where  $R_c(\tau)$  is the distance of the reference point from the radar at the slow-time  $\tau$ .  $T_{ref}$  is the reference signal duration, which is somewhat longer than the chirp pulse duration  $T_p$ . The time-domain compressed signal after stretch processing is given as follows:

$$\begin{aligned}
s_c(t, \tau) &= s(t, \tau) \cdot s_r^*(t, \tau) \\
&= \sum_m \sigma_m \cdot \text{rect} \left( \frac{t - 2R_m(\tau)}{T_p} \right) \cdot \exp \left( j \frac{4\pi}{c} \mu \left( t - \frac{2R_c}{c} \right) \Delta R_m(\tau) \right) \\
&\quad \cdot \exp \left( j \frac{4\pi}{c} f_c \Delta R_m(\tau) \right) \cdot \exp \left( j \frac{4\pi \mu}{c^2} \Delta R_m^2(\tau) \right) \\
&\quad + \sum_n \sigma_n \cdot \text{rect} \left( \frac{t - 2R_n(\tau)}{T_p} \right) \cdot \exp \left( j \frac{4\pi}{c} \mu \left( t - \frac{2R_c}{c} \right) \Delta R_n(\tau) \right) \\
&\quad \cdot \exp \left( j \frac{4\pi}{c} f_c \Delta R_n(\tau) \right) \cdot \exp \left( j \frac{4\pi \mu}{c^2} \Delta R_n^2(\tau) \right) \\
&= \sum_m \sigma_m \cdot \text{rect} \left( \frac{t - 2R_m(\tau)}{T_p} \right) \cdot \exp(j\Phi_m(t, \tau)) \\
&\quad + \sum_n \sigma_n \cdot \text{rect} \left( \frac{t - 2R_n(\tau)}{T_p} \right) \cdot \exp(j\Phi_n(t, \tau))
\end{aligned} \tag{A.16}$$

where

$$\begin{aligned}
\Delta R_m(\tau) &= R_m(\tau) - R_c(\tau) \\
&\approx R_m(0) - R_c + x_m \cdot \frac{vT}{R_m(0)} \\
&= \Delta R_m(0) + x_m \cdot \frac{vT}{R_m(0)}
\end{aligned} \tag{A.17}$$

$$\Delta R_n(\tau) = R_n(\tau) - R_c(\tau) \approx R_n \sin(\omega_n \tau + \theta_{n0}) \tag{A.18}$$

$$\Phi_m(t, \tau) = -\frac{4\pi}{c}\mu(t - \frac{2R_c}{c}) \cdot \Delta R_m(\tau) + \frac{4\pi}{c}f_c \cdot \Delta R_m(\tau) + \frac{4\pi\mu}{c^2} \cdot \Delta R_m^2(\tau) \quad (\text{A.19})$$

$$\Phi_n(t, \tau) = -\frac{4\pi}{c}\mu(t - \frac{2R_c}{c}) \cdot \Delta R_n(\tau) + \frac{4\pi}{c}f_c \cdot \Delta R_n(\tau) + \frac{4\pi\mu}{c^2} \cdot \Delta R_n^2(\tau) \quad (\text{A.20})$$

The second term of (A.19) and (A.20) cause a variation in the phase to produce a Doppler shift, whereas the third term is the residual video phase (RVP) error, which can be removed by simple processing. Next, we assume that the standard motion compensation has been completed to remove the translation motion. Assuming that the RVP error has been eliminated, taking the Fourier transforms of (A.16) with respect to the fast-time  $\tau$ , we obtain

$$\begin{aligned} S_c(f, \tau) = & \sum_m \sigma_m T_p \operatorname{sinc} \left( T_p \left( f + \frac{2\mu}{c}(\Delta R_m(\tau)) \right) \right) \cdot \exp \left( j \frac{4\pi}{\lambda} \Delta R_m(\tau) \right) \\ & + \sum_n \sigma_n T_p \operatorname{sinc} \left( T_p \left( f + \frac{2\mu}{c}(\Delta R_n(\tau)) \right) \right) \cdot \exp \left( j \frac{4\pi}{\lambda} \Delta R_n(\tau) \right) \end{aligned} \quad (\text{A.21})$$

We have obtained the expression of (4.4).

# Bibliography

- [1] M. I. Skolnik, *Introduction to Radar Systems*. McGraw Hill, 1980.
- [2] Wikipedia. Aircraft collision avoidance systems. [Online]. Available:  
[http://en.wikipedia.org/wiki/Aircraft\\_collision\\_avoidance\\_systems](http://en.wikipedia.org/wiki/Aircraft_collision_avoidance_systems)
- [3] J. C. Curlander and R. N. McDonough, *Synthetic Aperture Radar Systems and Signal Processing*. John Wiley and Sons, 1991.
- [4] B. R. Mahafza, *Radar Systems Analysis and Design Using MATLAB*. CRC Press, 2005.
- [5] M. Soumekh, *Synthetic aperture radar signal processing with MATLAB algorithms*. John Wiley and Sons, 1999.
- [6] B. R. Mahafza and A. Z. Elsherbeni, *MATLAB Simulations for Radar Systems Design*. CRC Press, 2004.
- [7] G. R. Curry, *Radar System Performance Modeling*. Artech House, 2005.
- [8] G. V. Morris, *Airborne Pulsed Doppler Radar*. Artech House, 1988.

- [9] D. L. Mensa, *High Resolution Radar Cross-Section Imaging*. Artech House, 1991.
- [10] D. R. Wehner, *High Resolution Radar*. Artech House, 1994.
- [11] D. A. Ausherman, A. Kozma, J. L. Walker, H. M. Jones, and E. C. Poggio, "Developments in radar imaging," *IEEE Trans. Aerosp. Electron. Syst.*, vol. 20, no. 4, pp. 363–400, July 1984.
- [12] C. C. Chen and H. C. Andrews, "Target-motion-induced radar imaging," *IEEE Trans. Aerosp. Electron. Syst.*, vol. 16, no. 1, pp. 2–14, Jan. 1980.
- [13] ———, "Multifrequency imaging of radar turntable data," *IEEE Trans. Aerosp. Electron. Syst.*, vol. 16, no. 1, pp. 15–22, Jan. 1980.
- [14] J. L. Walker, "Range-doppler imaging of rotating objects," *IEEE Trans. Aerosp. Electron. Syst.*, vol. 16, no. 1, pp. 23–52, Jan. 1980.
- [15] L. C. Graham, "Synthetic interferometer radar for topographic mapping," *IEEE Proc.*, vol. 62, pp. 763–768, June 1974.
- [16] R. Bamler and P. Hartl, "Synthetic aperture radar interferometry," *Inv. Prob.*, vol. 14, pp. R1–R54, Aug. 1998.
- [17] A. K. Gabriel, R. M. Goldstein, and H. A. Zebker, "Mapping small elevation changes over large areas: Differential interferometry," *J. Geophys. Res.*, vol. 94, pp. 9183–9191, 1989.

- [18] R. M. Narayanan, R. D. Mueller, and R. D. Palmer, "Random noise radar interferometry," *Proc. SPIE*, vol. 2845, pp. 75–82, 1996.
- [19] M. Soumekh, "Automatic aircraft landing using interferometric inverse synthetic aperture radar imaging," *IEEE Trans. Image Processing*, vol. 5, no. 9, pp. 1335–1345, Sept. 1996.
- [20] G. Y. Wang, X. G. Xia, and V. C. Chen, "Three-dimensional isar imaging of maneuvering targets using three receivers," *IEEE Trans. Image Processing*, vol. 10, no. 3, pp. 436–447, Mar. 2001.
- [21] X. J. Xu and R. M. Narayanan, "Three-dimensional interferometric isar imaging for target scattering diagnosis and modeling," *IEEE Trans. Image Processing*, vol. 10, no. 7, pp. 1094–1102, July 2001.
- [22] Q. Zhang, T. S. Yeo, G. Du, and S. Zhang, "Estimation of three-dimensional motion parameters in interferometric isar imaging," *IEEE Trans. Geosci. Remote Sensing*, vol. 42, no. 2, pp. 292–300, Feb. 2004.
- [23] Q. Zhang and T. S. Yeo, "Three-dimensional sar imaging of a ground moving target using the inisar technique," *IEEE Trans. Geosci. Remote Sensing*, vol. 42, no. 9, pp. 1818–1828, Sept. 2004.
- [24] Z. Bao, G. Y. Wang, and L. Luo, "Inverse synthetic aperture radar imaging of maneuvering targets," *Opt. Eng.*, vol. 37, p. 1582, 1998.

- [25] V. C. Chen and S. Qian, "Joint time-frequency transform for radar range doppler imaging," *IEEE Trans. Aerosp. Electron. Syst.*, vol. 34, no. 2, pp. 486–499, Apr. 1998.
- [26] V. C. Chen and H. Ling, *Time-frequency transforms for radar imaging and signal analysis*. Artech House, 2002.
- [27] G. Y. Wang and Z. Bao, "Isar imaging of maneuvering targets based on chirplet decomposition," *Opt. Eng.*, vol. 38, pp. 1534–1541, 1999.
- [28] Y. Wang, H. Lin, and V. C. Chen, "Isar motion compensation via adaptive joint time-frequency techniques," *IEEE Trans. Aerosp. Electron. Syst.*, vol. 34, no. 2, pp. 670–677, Apr. 1998.
- [29] J. Li, D. M. Zheng, and P. Stoica, "Angle and waveform estimation via relax," *IEEE Trans. Aerosp. Electron. Syst.*, vol. 33, no. 3, pp. 1077–1087, July 1997.
- [30] V. C. Chen, "Analysis of radar micro-doppler signature with time-frequency transform," *Proc. Statistical Signal and Array processing*, pp. 463–466, Aug. 2000.
- [31] V. C. Chen and F. Li, "Analysis of radar micro-doppler signatures," *IEE Proc. Radar Sonar Navig*, vol. 150, pp. 271–276, 2003.



- [32] T. Sparr and P. Kane, "Micro-doppler analysis of vibrating targets in sar," *IEE Proc. Radar Sonar Navig*, vol. 150, no. 4, pp. 277–283, Aug. 2003.
- [33] J. E. Gray and S. R. Addison, "Effect of nonuniform target motion on radar backscattered waveforms," *IEE Proc. Radar Sonar Navig*, vol. 150, no. 4, pp. 262–270, Aug. 2003.
- [34] J. Lei and C. Lu, "Target classification based on micro-doppler signatures," *IEEE International Radar Conference*, pp. 179–183, May 2005.
- [35] V. C. Chen, "Spatial and temporal independent component analysis of micro-doppler features," *IEEE International Radar Conference*, pp. 348–353, May 2005.
- [36] T. Thayaparan, S. Abrol, and E. Riseborough, "Micro-doppler feature extraction of experimental helicopter data using wavelet and timecfrequency analysis," *Proc. Radar*, pp. 19–22, Oct. 2004.
- [37] A. Bultan, "A four-parameter atomic decomposition of chirplets," *IEEE Trans. Signal Processing*, vol. 47, no. 3, pp. 731–745, Mar. 1999.
- [38] J. Li and H. Ling, "Application of adaptive chirplet representation for isar feature extraction from targets with rotating parts," *IEE Proc. Radar Sonar Navig.*, vol. 150, no. 4, pp. 284–291, Aug. 2003.

- [39] B. D. Steinberg, "Microwave imaging of aircraft," *IEEE Proc.*, vol. 76, no. 12, pp. 1578–1592, Dec. 1988.
- [40] H. L. V. Trees, Ed., *Optimum Array Processing Part IV of Detection, Estimation and Modulation Theory*. New York: John Wiley and Sons, 2002.
- [41] F. Athley, C. Engdahl, and P. Sunnergren, "Model-based detection and direction of arrival estimation in radar using sparse arrays," *Proc. Signals, Systems and Computers*, vol. 2, pp. 1953–1957, Nov. 2004.
- [42] S. Holm, B. Elgetun, and G. Dahl, "Properties of the beampattern of weight and layout-optimization sparse arrays," *IEEE Trans. Ultrason., Ferroelect., Freq. Contr.*, vol. 44, no. 5, pp. 983–991, Sept. 1997.
- [43] A. Austeng and S. Holm, "Sparse arrays for real-time 3d imaging, simulated and experimental results," *IEEE Ultrasonics Symposium*, vol. 2, pp. 1187–1190, Oct. 2000.
- [44] A. Austeng, S. Holm, P. K. Weber, N. Aakvaag, and K. Iranpour, "1d and 2d algorithmically optimized sparse arrays," *IEEE Ultrasonics Symposium*, vol. 2, pp. 1683–1686, Oct. 1997.
- [45] D. J. Rabideau and P. Parker, "Ubiquitous mimo multifunction digital array radar," *Proc. 37th IEEE Asil. Conf on Signals, Systems, and Computers*, vol. 1, pp. 1057–1064, Nov. 2003.

- [46] D. W. Bliss and K. W. Forsythe, "Multiple-input multiple-output (mimo) radar and imaging: degrees of freedom and resolution," *Proc. 37th IEEE Asil. Conf on Signals, Systems, and Computers*, vol. 1, pp. 54–59, Nov. 2003.
- [47] E. Fishler, A. Haimovich, R. S. Blum, L. J. Cimini, D. Chizhik, and R. A. Valenzuela, "Spatial diversity in radars-models and detection performance," *IEEE Trans. Signal Processing*, vol. 54, no. 3, pp. 823–837, Mar. 2006.
- [48] F. C. Robey, S. Coutts, D. Weikle, J. C. McHarg, and K. Cuomo, "Mimo radar theory and experimental results," *Proc. 38th IEEE Asil. Conf on Signals, Systems, and Computers*, vol. 1, pp. 300–304, Nov. 2004.
- [49] D. R. Fuhrmann and G. S. Antonio, "Transmit beamforming for mimo radar systems using partial signal correlation," *IEEE Trans. Aerosp. Electron. Syst.*, vol. 44, no. 1, pp. 171–186, Jan. 2008.
- [50] G. S. Antonio and D. R. Fuhrmann, "Beampattern synthesis for wideband mimo radar systems," *Proc. 1st. IEEE Workshop CAMSAP*, pp. 105–108, Dec. 2005.
- [51] K. W. Forsythe and D. W. Bliss, "Waveform correlation and optimization issues for mimo radar," *Proc. 39th IEEE Asil. Conf on Signals, Systems, and Computers*, pp. 1306–1310, Nov. 2005.

- [52] C. Y. Chen and P. P. Vaidyanathan, "Beamforming issues in modern mimo radars with doppler," *Proc. 40th IEEE Asil. Conf on Signals, Systems, and Computers*, pp. 41–45, Nov. 2006.
- [53] L. S. Cohen, "Radar spectrum management issues and problems," *Proc. Tri-Service Radar Symp.*, June 2004.
- [54] J. Isnard, "Spectrum management: A high stakes game," *IEEE Aerosp. Electron. Syst. Mag.*, vol. 13, no. 4, pp. 3–8, Apr. 1998.
- [55] K. Gerlach, A. K. Shackelford, and S. D. Blunt, "Combined multistatic adaptive pulse compression and adaptive beamforming for shared-spectrum radar," *IEEE Journal of Selected Topics in Signal Processing.*, vol. 1, no. 1, pp. 137–146, June 2007.
- [56] S. D. Blunt and K. Gerlach, "Aspects of multistatic adaptive pulse compression," *Proc. IEEE Intl. Conf. Radar*, pp. 104–108, May 2005.
- [57] —, "Multistatic adaptive pulse compression," *IEEE Trans. Aerosp. Electron. Syst.*, vol. 42, no. 3, pp. 891–903, July 2006.
- [58] —, "A novel pulse compression scheme based on minimum mean-square error reiteration," *Proc. IEEE Int. Conf. Radar*, pp. 349–353, Sept. 2003.
- [59] —, "Adaptive pulse compression via mmse estimation," *IEEE Trans. Aerosp. Electron. Syst.*, vol. 42, no. 2, pp. 572–584, Apr. 2006.

- [60] J. M. Headrick and M. I. Skolnik, "Over-the-horizon radar in the hf band," *Proc. IEEE*, vol. 62, no. 6, pp. 664–673, June 1974.
- [61] M. I. Skolnik, *Radar Handbook*. McGraw Hill, 2008.
- [62] T. M. Georges and J. A. Harlan, "New horizons for over-the-horizon radar," *IEEE Antennas Propagat. Mag.*, vol. 36, no. 4, pp. 14–24, Aug. 1994.
- [63] G. Wang, X. G. Xia, B. T. Root, V. C. Chen, Y. Zhang, and M. G. Amin, "Maneuvering target detection in over-the-horizon radar using adaptive clutter rejection and adaptive chirplet transform," *Proc. Inst. Elect. Eng., Radar, Sonar, Navig.*, vol. 150, pp. 292–298, Aug. 2003.
- [64] Y. Zhang, M. G. Amin, and G. J. Frazer, "High-resolution time-frequency distributions for manoeuvring target detection in over-the-horizon radars," *Proc. Inst. Elect. Eng., Radar, Sonar, Navig.*, vol. 150, pp. 299–304, Aug. 2003.
- [65] X. Guo, H. Sun, and T. S. Yeo, "Transient interference excision in over the-horizon radar using adaptive time-frequency analysis," *IEEE Trans. Geosci. Remote Sensing*, vol. 43, no. 4, pp. 722–725, Apr. 2005.
- [66] Y. Zhang, G. J. Frazer, and M. G. Amin, "Simultaneous operation of two over-the-horizon radars," *Proc. SPIE Advanced Signal Processing Algorithms, Architectures, and Implementations*, pp. 313–324, Aug. 2004.

- [67] ———, “Concurrent operation of two over-the-horizon radars,” *IEEE Journal of Selected Topics in Signal Processing.*, vol. 1, no. 1, pp. 114–123, June 2007.
- [68] I. G. Cumming and F. H. Wong, *Digital Processing of Synthetic Aperture Radar Data: Algorithms and Implementation.* Artech House, 2005.
- [69] G. Y. Delisle and H. Q. Wu, “Moving target imaging and trajectory computation using isar,” *IEEE Trans. Aerosp. Electron. Syst.*, vol. 30, no. 3, pp. 887–899, July 1994.
- [70] H. Q. Wu, D. Grenier, G. Y. Delisle, and D. G. Fang, “Translational motion compensation in isar image processing,” *IEEE Trans. Image Processing*, vol. 4, no. 11, pp. 1561–1571, Nov. 1995.
- [71] W. Ye, T. S. Yeo, and Z. Bao, “Weighted least-squares estimation of phase errors for sar/isar autofocus,” *IEEE Trans. Geosci. Remote Sensing*, vol. 37, no. 5, pp. 2487–2494, Sept. 1999.
- [72] J. A. Given and W. R. Schmidt, “Generalized isar-part ii: interferometric techniques for three-dimensional location of scatterers,” *IEEE Trans. Image Processing*, vol. 14, no. 11, pp. 1792–1797, Nov. 2005.
- [73] C. Z. Ma, “Research on radar three dimensional imaging techniques,” Ph.D. dissertation, Xidian University, China, 1999.

- [74] P. Stoica and A. Nehorai, "Music, maximum likelihood and the cramer-rao bound," *IEEE Trans. Acoust., Speech, Signal Processing*, vol. 37, no. 5, pp. 720–741, May 1989.
- [75] C. Z. Ma, T. S. Yeo, Q. Zhang, H. S. Tan, and J. Wang, "Three-dimensional isar imaging based on antenna array," *IEEE Trans. Geosci. Remote Sensing*, vol. 46, no. 2, pp. 504–515, Feb. 2008.
- [76] S. Holm, B. Elgetun, and G. Dahl, "Properties of the beampattern of weight and layout-optimization sparse arrays," *IEEE Trans. Ultrason., Ferroelect., Freq. Contr.*, vol. 44, no. 5, pp. 983–991, Sept. 1997.
- [77] V. C. Chen, F. Y. Li, S. S. Ho, and H. Wechsler, "Micro-doppler effect in radar: Phenomenon, model, and simulation study," *IEEE Trans. Aerosp. Electron. Syst.*, vol. 42, no. 1, pp. 2–21, Jan. 2006.
- [78] C. J. Cai, W. X. Liu, J. S. Fu, and L. L. Lu, "Empirical mode decomposition of micro-doppler signature," *IEEE Proc. Int. Radar Conf.*, pp. 895–899, May 2005.
- [79] K. Glossop, P. J. G. Lisboa, P. C. Russell, A. Siddans, and G. R. Jones, "An implementation of the hough transformation for the identification and labelling of fixed period sinusoidal curves," *Comput. Vis. Image Underst.*, vol. 74, pp. 96–100, Apr. 1999.

- [80] B. B. Thappa, P. Hughett, and K. Karasaki, "Semi-automatic analysis of rock-fracture orientations from borehole wall images," *Geophysics*, vol. 62, pp. 129–137, Jan. 1997.
- [81] V. C. Chen and W. J. Miceli, "Time-varying spectral analysis for imaging of manoeuvring targets," *Proc. Inst. Electr. Eng. Radar Sonar Navig*, vol. 145, pp. 262–268, 1998.
- [82] Z. Bao, C. Y. Sun, and M. D. Xing, "Time-frequency approaches to isar imaging of maneuvering targets and their limitations," *IEEE Trans. Aerosp. Electron. Syst.*, vol. 37, no. 3, pp. 1091–1099, July 2001.
- [83] P. Steeghs and S. Gelsema, "Application of radon transforms and time-frequency representations to isar imagery," *Proc. SPIE*, vol. 5102, pp. 189–199, 2003.
- [84] P. V. C. Hough, "Methods and means for recognizing complex patterns," U.S. Patent 306 9654, 1962.
- [85] P. S. Wu and M. Li, "A novel transform for curve detection," *IEEE Proc. Int. Conf. Syst., Man, Cybern*, vol. 4, pp. 2722–2727, 1996.
- [86] T. M. Breuel, "Recognition by adaptive subdivision of transformation space: Practical experiences and comparison with the hough transform," *IEE Proc. Colloq. Hough Transforms*, pp. 7/1–7/4, May 1993.



- [87] J. Turan, P. Filo, P. Farkas, and D. Siskovicova, "Parameter estimation based on hough transform," *Proc. 4th EURASIP Conf. Focused Video/Image Process. Multimedia Commun.*, vol. 1, pp. 221–226, July 2003.
- [88] J. Qi, Z. C. Shi, X. Y. Zhao, and Y. S. Wang, "A novel fingerprint matching method based on the hough transform without quantization of the hough space," *Proc. 3rd Int. Conf. Image Graph.*, pp. 262–265, Dec. 2004.
- [89] A. L. Kesidis and N. Papamarkos, "On the inverse hough transform," *IEEE Trans. Pattern Anal. Machine Intell.*, vol. 21, no. 12, pp. 1329–1343, Dec. 1999.
- [90] M. Atiquzzaman, "Multi-resolution hough transforman efficient method of detecting patterns in images," *IEEE Trans. Pattern Anal. Machine Intell.*, vol. 14, no. 11, pp. 1090–1095, Nov. 1992.
- [91] D. S. Mckenzie and S. R. Protheroe, "Curve description using the inverse hough transform," *Pattern Recognition*, vol. 23, pp. 283–290, Mar. 1990.
- [92] D. H. Ballard, "Generalization the hough transform to detect arbitrary shapes," *Pattern Recognition*, vol. 13, pp. 111–122, 1981.
- [93] H. Keishi, M. Tsugito, and U. Takashi, "A real-time processor for the hough transform," vol. 10, no. 1, pp. 121–125, Jan. 1988.

- [94] A. S. Aguado, M. E. Montiel, and M. S. Nixon, "Improving parameter space decomposition for the generalised hough transform," *Proc. IEEE Int. Conf. Image Process*, vol. 3, pp. 627–630, Sept. 1996.
- [95] A. Goneid, S. Gindi, and A. Sewisy, "A method for the hough transform detection of circles and ellipse using a 1-dimensional array," *Proc. IEEE Int. Conf. Syst., Man Cybern.*, vol. 4, pp. 3154–3157, Oct. 1997.
- [96] Y. Lei and K. C.Wong, "Ellipse detection based on symmetry," *Pattern Recognit. Lett.*, vol. 20, pp. 41–47, Jan. 1999.
- [97] B. D. Carlson, E. D. Evans, and S. L.Wilson, "Search radar detection and track with the hough transform-part i: System concept," *IEEE Trans. Aerosp. Electron. Syst.*, vol. 30, no. 1, pp. 102–108, Jan. 1994.
- [98] K. Mikolajczyk, T. Tuytelaars, C. Schmid, A. Zisserman, J. Matas, F. Schafalitzky, T. Kadir, and L. V. Gool, "A comparison of affine region detectors," *International Journal of Computer Vision*, pp. 43–72, Jan. 2006.
- [99] Q. Zhang, T. S. Yeo, and H. S. Tan, "Imaging of moving target with rotating parts based on hough transform," *IEEE Geoscience and Remote Sensing Symposium Proc.*, pp. 4183–4186, Aug. 2006.
- [100] G. Y. Wang and Z. Bao, "A new algorithm of range alignment in isar motion compensation," *ACTA Electronica Sinica*, vol. 26, pp. 5–8, 1998.

- [101] G. Y. Lu and Z. Bao, "Range alignment for targets with moving parts in isar imaging," *Systems Engineering and Electronics*, vol. 22, pp. 12–15, 2000.
- [102] M. D. Xing, Z. Bao, and Y. M. Zheng, "Range alignment using global optimization criterion in isar imaging," *ACTA Electronica Sinica*, vol. 29, pp. 1807–1811, Dec. 2001.
- [103] J. Misiurewicz, K. Kulpa, and Z. Czekala, "Analysis of recorded helicopter echo," *IEE Conference of Radar 97*, pp. 449–513, Oct. 1997.
- [104] Z. Y. Tang, Y. L. Wang, and X. Z. Jiang, "Radar detection of hovering helicopter," *Modern Radar*, vol. 12, pp. 15–19, 2000.
- [105] W. F. Sun, C. Zhang, and Y. L. Wang, "Radar detection of hovering helicopter," *ACTA Electronica Sinica*, vol. 30, pp. 896–899, June 2002.